5-4-2015 12:00 AM

Response of Endothelial Cells to Quantified Hemodynamic Shear Stress

Hamed Avari
The University of Western Ontario

Supervisor
Dr. Eric Savory
The University of Western Ontario

Graduate Program in Mechanical and Materials Engineering
A thesis submitted in partial fulfillment of the requirements for the degree in Doctor of Philosophy

Recommended Citation

Avari, Hamed, "Response of Endothelial Cells to Quantified Hemodynamic Shear Stress" (2015). *Electronic Thesis and Dissertation Repository*. 2830.
https://ir.lib.uwo.ca/etd/2830

RESPONSE OF ENDOTHELIAL CELLS TO QUANTIFIED HEMODYNAMIC SHEAR STRESS

(Thesis format: Integrated Article)

by

Hamed Avari

Graduate Program in Mechanical and Materials Engineering

A thesis submitted in partial fulfillment
of the requirements for the degree of
Doctor of Philosophy

The School of Graduate and Postdoctoral Studies
The University of Western Ontario
London, Ontario, Canada

Abstract

Cardiovascular diseases (CVDs) are the number one cause of death globally. Arterial endothelial cell (EC) dysfunction plays a key role in many of these CVDs, such as atherosclerosis. Blood flow-induced wall shear stress (WSS), among many other pathophysiological factors, is shown to significantly contribute to EC dysfunction. Atherosclerotic lesions are mainly located at the bends and bifurcations of the arterial network where the flow is disturbed (i.e., low and reciprocating WSS). Although many *in vitro* studies have been dedicated to the WSS effects on ECs, accurate quantification of the flow within the experimental facility remains elusive. Additionally, analysis of EC response, in some aspects, relies solely on descriptive methods.

The present dissertation is an *in vitro* investigation of quantified WSS on ECs to quantitatively analyze the EC morphometric parameters, as well as cytoskeletal remodeling.

A hemodynamic facility based on the parallel plate flow chamber (PPFC) concept, with test section dimensions of 22 × 17.5 × 1.8 mm (L × W × H =length, width and height, respectively), capable of producing a wide range of physiologically relevant conditions was developed. The Laser Doppler Velocimetry (LDV) method with a custom set-up was implemented to suit the needs of the small-scale channel flow measurements.

The effects of four different flow cases including the low steady laminar (LSL), medium steady laminar (MSL), non-zero-mean sinusoidal laminar (NZMSL), laminar carotid (LCRD) on EC area, perimeter, shape index (S.I.), angle of orientation, F-actin bundle remodeling and PECAM-1 re-distribution were studied. The S.I. and angle of orientation were found to be the most flow-sensitive morphometric parameters. A 2D FFT based image processing technique was applied to analyze the F-actin directionality and an alignment index (A.I.) was defined accordingly. For the first time, a (linear) mathematical relationship was proposed, based on the current findings, between the cell orientation vs. F-actin alignment. Also, for the first time, a significant peripheral loss of PECAM-1 in ECs subjected to athero-prone cases (LSL and NZMSL) with high internalization of this protein is reported, which might shed light on the mechanosensory role of PECAM-1 in mechanotransduction.

Keywords

Atherosclerosis, Endothelial Cell, Endothelial Dysfunction, Wall Shear Stress, Laser Doppler Velocimetry (LDV), Small-scale Conventional Channel Flow, Pulsatile, low-Reynolds number, Turbulence, Morphology, Shape Index, Angle of Orientation, F-actin, PECAM-1, CD31.

Co-Authorship Statement

This doctoral thesis is prepared in accordance with the regulations for an Integrated-Article thesis stipulated by the School of Graduate and Postdoctoral Studies (SGPS) at the University of Western Ontario. This document includes co-authored articles where the contribution of each author will be explicitly stated below.

Chapter 2: An *in vitro* Hemodynamic Facility to Study the Effects of Quantified Shear Stresses on Endothelial Cells

The experiments were designed by Hamed Avari with guidance from Drs. Eric Savory and Kem A Rogers. Conducting all of the literature review, experiments and their data analysis and authoring the document was completed by Hamed Avari. The work was supervised by Dr. Eric Savory and mentored by Kem A Rogers. The chapter drafts were read by Drs. Eric Savory and Kem A Rogers and their revisions were provided to Hamed Avari. A version of this chapter, authored by Hamed Avari, Eric Savory and Kem A Rogers, has been submitted for review to the Journal of Cardiovascular Engineering and Technology.

Chapter 3: Wall Shear Stress for Laminar, Pulsatile and Low-Reynolds Number Turbulent Flows in a Parallel Plate Flow Chamber (PPFC) using Laser Doppler Velocimetry (LDV)

The experiments were designed by Hamed Avari with guidance from Drs. Eric Savory and Kem A Rogers. Major direction was provided by Dr. Eric Savory. Conducting all of the literature review, experiments and their data analysis and authoring the document was completed by Hamed Avari. The work was supervised by Dr. Eric Savory. The chapter drafts were read by Drs. Eric Savory and Kem A Rogers and their revisions were provided to Hamed Avari. A version of this chapter, authored by Hamed Avari, Eric Savory and Kem A Rogers, has been submitted for review to the ASME Journal of Fluids Engineering.

Chapter 4: Quantification of Morphological Modulation, F-Actin Remodeling and PECAM-1 (CD-31) Re-distribution in Endothelial Cells in Response to Fluid-Induced Shear Stress under Various Flow Conditions

The experiments were designed by Hamed Avari with guidance from Drs. Kem A Rogers and Eric Savory. The cell biology-related analysis including the imaging was conducted at the Department of Anatomy and Cell Biology. Conducting all of the literature review, experiments and their data analysis and authoring the document was completed by Hamed Avari. Dr. Kem A Rogers had a major contribution in the cell imaging and immunofluorescence process. The work was supervised by Drs. Eric Savory and mentored by Dr. Kem A Rogers. The chapter drafts were read by Drs. Eric Savory and Kem A Rogers and their revisions were provided to Hamed Avari. A version of this chapter, authored by Hamed Avari, Kem A Rogers and Eric Savory has been submitted for review to the Journal of Biomechanics.

Dedication

To my wonderful parents for their endless love, support and encouragement

Acknowledgments

This dissertation is a product of the guidance, great support and friendship I have had the honour to receive during my PhD work. I would like to at least write a few lines to express my gratitude to anyone who has helped me along this journey.

First, I would like to show my special gratitude to my supervisor Dr. Eric Savory and my mentor Dr. Kem A Rogers for their continued guidance, instruction, encouragement and patience and for providing me with the opportunity to conduct research in an area where, as an engineer, I could make a contribution in the area of human health, although very little.

I want to acknowledge my advisory committee members Drs. Anthony Straatman and Kamran Siddiqui for providing insight toward the success of the project, as well as Prof. Martin Sandig for his guidance on how to approach an interdisciplinary research study such as the current one. I should also thank Mrs. Joanna Bloom (graduate coordinator) at the Mechanical and Materials Engineering (MME) Department at the University of Western Ontario (UWO).

I would like to show gratitude to Mrs. Jessica Davie, Dr. Zachary Armstrong and Dr. Silvia Penuela for training me in the cell biology field and helping me to gain the skills I needed for this study.

I would also like to thank Mr. Dan Sweiger at the University Machine Services (UMS) for his great effort and patience in the development process of the experimental facility as well as Mr. Marin Vratonjic for his input in the PPFC design. My thanks also go to Mr. Cody Ruthman (UMS) for the improvement works done on the facility as well as Mrs. Paul Sheller (purchasing coordinator) at UWO Engineering Finance and Stores. I am also thankful to Mrs. Soheil Afara and Brian Dennis for providing the experimental facility and guidance to characterize the biological fluid.

I am also thankful to all of my previous and current colleagues in the Advanced Fluid Mechanics Research Group (AFM) at UWO, especially to Dr. William Lin for his guidance during my PhD and for reviewing some of the documents and Dr. Taravat Khadivi for her support and Dr. Charles Guo for his guidance.

And my special thanks go to my wonderful family, for their support and endless love, without whom I would have not been where I am now; And to all of my friends who encouraged me along the way.

Table of Contents

List of Tables

List of Figures

List of Appendices

List of Abbreviations

2D FFT	two-dimensional fast Fourier transform
BAEC	bovine aortic endothelial cell
BSA	bovine serum albumin
CCA	common carotid artery
CD 31	cluster of differentiation 31
CFD	computational fluid dynamics
CVD	cardio vascular disease
Cx	connexin
DMEM	Dulbecco's Modified Eagle's medium
DNS	direct numerical simulation
EC	endothelial cell
eNOS	endothelial nitric oxide synthase
FBS	fetal bovine serum
FSO	full sale output
HWA	hot-wire anemometry
ICAM-1	intercellular adhesion molecule 1
LCRD	laminar carotid
LDL	low-density lipoprotein
LDV	laser Doppler velocimetry
LSL	low steady laminar
MSL	medium steady laminar
NMMII	non-muscle myosin II

NO	nitric oxide
NZMSL	non-zero-mean sinusoidal laminar
oxLDL	oxidized Low-density lipoprotein
PAEC	porcine aortic endothelial cell
PBS	phosphate buffered saline
PDM	photodetector multiplier
PECAM-1	platelet endothelial cell adhesion molecule 1
PPFC	parallel plate flow chamber
rms	root mean square
ROI	region of interest
RT	room temperature
UDV	ultrasound Doppler velocimetry
VCAM-1	vascular cell adhesion molecule 1
WSS	wall shear stress
μPIV	micro particle image velocimetry
NFκB	nuclear factor kappa-light-chain-enhancer of activated B cells
SMC	smooth muscle cells
SEM	standard deviation error of the mean
ANOVA	analysis of variance
CAD	coronary artery disease
μl	microliter
mg	milligram
mm	millimeter

Nomenclature

A.I.	sum of the relative pixel intensities in the 10° and 180° bands
A_c	endothelial cell area (μm^2)
A_t	test section area (mm^2)
d	channel glass working section length (mm)
d_p	particle diameter
d_s	penetration depth of measuring volume
f	frequency
F_g, F_a	given and actual lens focal lengths
H	channel test section height (mm)
H(k,l)	2D Hartley transform function
I(n,m)	pixel intensity function at a 2D domain
k	distance from the pump to the test section (mm)
L	channel test section length (mm)
$\dot{N}$	data rate
N_p	number of point employed in regression method
n_p	degree of polynomial
NRSS	normalized Reynolds shear stress ($-\overline{u'v'}/u_\tau^2$)
OSI	$= 0.5\left(1.0 - \frac{\left\lvert\int_0^T \tau_W dt\right\rvert}{\int_0^T \lvert\tau_W\rvert\, dt}\right)$

p	p-value
P.R.D.	PECAM-1 relative density= total peripheral PECAM-1 area in a ROI/ (Number of ECs in that ROI × Average EC area in the ROI) × 100 %
P_c	endothelial cell perimeter (μm)
p_t	wetted perimeter of test section
P	time-averaged hydrostatic pressure (mmHg)
$\tilde{p}$	periodic bin-averaged hydrostatic pressure (mmHg)
P_t	instantaneous hydrostatic pressure (Pa, mmHg)
p'	instantaneous pressure fluctuations (mmHg)
<P>	phase-averaged hydrostatic pressure (Pa, mmHg)
Q	flow rate (ml/s)
r	vessel radius
Re	Reynolds number based on channel height and bulk velocity ($U_b H/\nu$)
Re_0	Reynolds number based on channel half-height and center-line velocity ($U_o \delta/\nu$)
RSS	Reynolds shear stress ($-\rho\overline{u'v'}$)
S.I.	shape index=$4\pi A_c/P_c^2$
St	Stoke’s number
T	pulsatile cycle period (s)

t	real time (s)
t^*	$=t/T$
$\tilde{u}$	periodic bin-average velocity
u, v	instantaneous x- and y- direction velocity
U,V	time-average x- and y-direction velocity
u',v'	x- and y-direction instantaneous velocity fluctuations
$<u>$	phase-averaged x-direction velocity (cm/s)
$<u>^*$	normalized phased-averaged streamwise velocity
U_b	bulk velocity
$U_{b\text{-}max}$	maximum bulk velocity of a pulse
U_o	center-line velocity
u_{rms}^+ , v_{rms}^+	u_{rms} and v_{rms} normalized by u_τ
u_τ	friction velocity
V	fluid average velocity
W	channel test section width (mm)
w_s	beam waist
α	Womersley number
δ	channel half height (mm)
δ_b	boundary layer thickness

ε, B, P, S	experimental uncertainty, bias errors, random errors and the standard deviation of the random errors
θ	beam half angle
θ_o	cell angle of orientation
$<\theta_o>$	average cell angle of orientation
μ	dynamic viscosity (Pa.s)
ν	kinematic viscosity (m^2/s)
ρ	density (kg/m^3)
ρ_f	fluid density
ρ_p	particle density
$\dot{\gamma} = \frac{\partial U}{\partial y}$	shear rate
τ	shear stress ($dyne/cm^2$)
τ_p	particle response time
τ_Λ	integral time scale
τ_w	wall shear stress ($dyne/cm^2$)
φ	Probe tilting angle
ω	angular frequency

Chapter 1

1 Introduction

As the major cause of death in the world, cardiovascular diseases (CVDs), such as atherosclerosis, have raised crucial concerns among scientists and researchers since they affect a large proportion of the world's population. An estimated 17.5 million people died in 2012 due to CVDs (i.e., 31% of all global deaths) including about 7.4 and 6.7 million deaths due to coronary heart disease and stroke, respectively [1]. Coronary artery disease (CAD) and cerebrovascular disease are the most common types of CVDs in which atherosclerosis is the underlying cause [2]. This chapter will introduce a brief summary about the cell biology and the cellular events involved in the pathobiology of diseases such as atherosclerosis. The specific area of the current research program is the effect of hemodynamic (blood flow) shear stresses on arterial endothelial cells (ECs) that contributes to the development of atherosclerosis and is the subject of the present thesis.

1.1 Artery Wall Structure and Endothelial Cell (EC)

Arteries are composed of three distinct layers; the outer layer known as the tunica externa, the mid-layer known as tunica media, which is made up of smooth muscle cells, and the inner-most layer known as tunica intima which is covered with a monolayer of endothelial cells (ECs) with an underlying internal elastic membrane (see Figure 1-1).

ECs cover the inner layer of the arterial as well as the venous system. Most animal cells, including ECs, have three types of cytoskeletal filaments that are responsible for the cells' spatial organization and mechanical properties. These three types are: microfilaments (actin), intermediate filaments and microtubules. Microfilaments determine the shape of the cell's surface and are necessary for whole-cell locomotion. Intermediate filaments provide mechanical strength, whilst microtubules determine the positions of the membrane-enclosed organelles and are responsible for direct intercellular transport [3]. Cytoskeletal systems are dynamic and adaptable, organized more like ant trails than interstate highways. A single trail of ants may persist for many hours, extending from the ant nest to, say , a picnic site, but the individual ants within the trail are anything buy static. If the ants find a new resource, the dynamic structure rearranges itself rapidly to deal with the situation. In a similar way, the cytoskeletal structure can change or persist, according to need, lasting for lengths of time ranging from less than a minute up to the cell's lifetime (i.e., from few hours to many years). Actin is a multifunctional protein that forms microfilaments which can be present as a free monomer called G-actin (globular) or as a linear polymer format called F-actin (filamentous). Actin filaments are two-stranded helical polymers of the protein actin and are organized into two types of arrays: bundles and web-like [3, 4]. Stress fibers are contractile actin bundles found in non-muscle cells (e.g., ECs) which are composed of F-actin and non-muscle myosin II (NMII), and also contain other linking proteins, such as α-actinin, to crosslink F-actin and NMII, consequently forming a highly regulated actomyosin structure. Stress fibers have been shown to play an important role in cellular contractility, cell adhesion, migration and morphogenesis [5]. A schematic of F-actin filament and stress fiber organization is shown in Figure 1-2

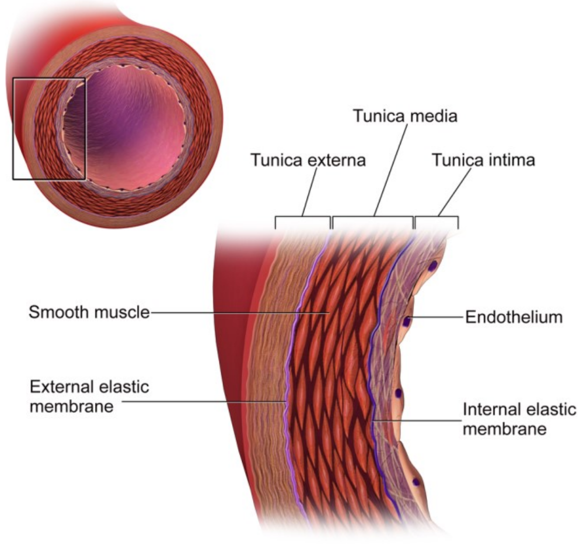

Figure 1-1 The structure of an artery wall (redrawn from [1])

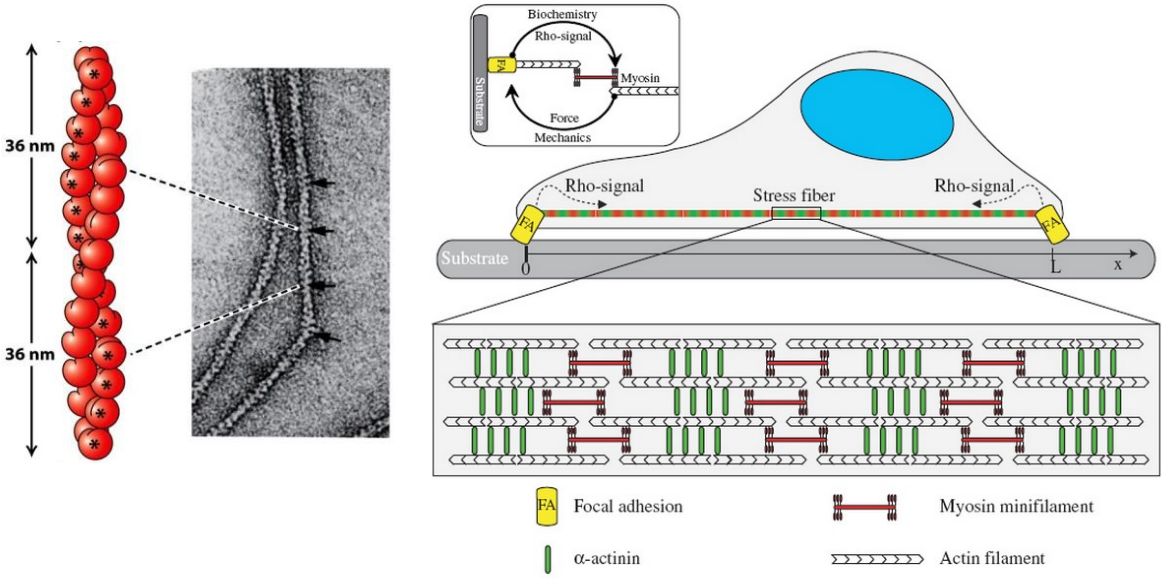

(A) **(B)**

Figure 1-2 Actin filaments are two-stranded helical polymers of the actin protein (G-actin, red spheres). They appear as flexible structure with a diameter of 5-9 nm (A); Schematic of stress fibres which are mainly composed of actin filaments (linear bundles), NMII, α-actinin. These stress fibres are fastened to the substrate through focal adhesion molecules which are also acting as a support (redrawn from [3])

1.2 Cell-Cell Junctions and Adhesions

The most fundamental interactions between cells are those that hold the cells together. Cells may be connected to each other through direct cell-cell junctions or they may be bound together by extracellular material. These attachments can be categorized into four functional classes (see for visualization see Figure 1-3) [3].

1) **Anchoring junctions**, including both cell-cell and cell-matrix adhesions which transmit stresses and are tethered to cytoskeletal filaments within the cell.

2) **Occluding junctions**, which seal the gap between the cells to make an impermeable barrier.

3) **Channel-forming junctions**, which create passageways to link the cytoplasm of the neighboring cells

4) **Signal-relaying junctions**, which allow signals to be relayed cell-to-cell across their plasma membrane.

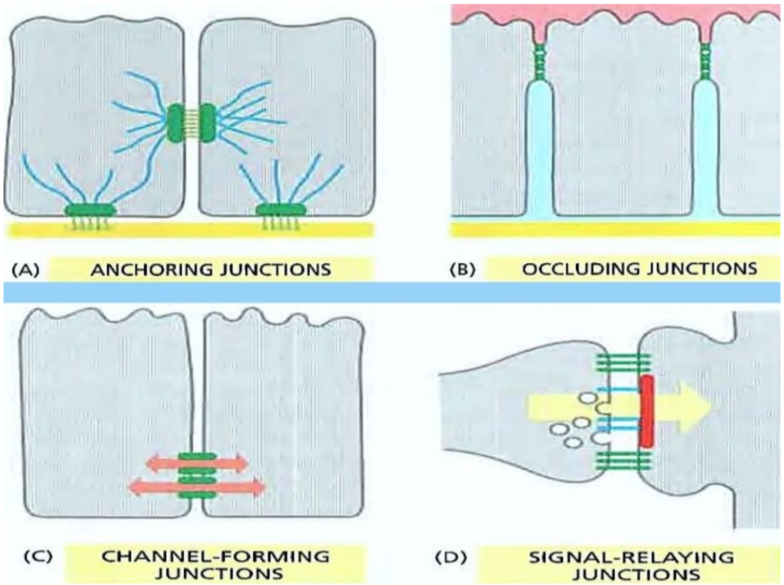

Figure 1-3 Four functional classes of cell junctions (redrawn from [3])

Cell adhesion, which is the binding of a cell to another cell or to a substrate, occurs through adhesion molecules such as selectin, integrins and cadherins [6]. Platelet endothelial cell adhesion molecule-1 (PECAM-1/ CD31) is expressed on the surface of platelets and leukocytes, and is also concentrated at the lateral junctions of ECs and has been implicated in various biological functions such as leukocyte transmigration, cell migration, angiogenesis, cell signaling and cell adhesion [7]. PECAM-1 mediates cell-cell adhesion and may be involved in some of the interactive events taking place in angiogenesis [8].

1.3 Mechanotransduction

Mechanotransduction is the many mechanisms by which cells convert mechanical stimulus into chemical activity [9-10]. ECs respond to the sensed mechanical forces and can modify intracellular signaling, gene expression and protein expression which, consequently, results in cell function regulation [9]. Blood vessels are subjected to shear stress, hydrostatic pressure and cyclic stretch (see Figure 1-4). Shear stress (force per unit area, commonly given in dyne/cm^2) induced by the blood flow on the vascular system acts parallel to the endothelial monolayer and is caused by the blood viscosity and the gradient of the velocity at the blood-tissue interface [4, 11]. Once the shear-induced signal activates the sensors, a complicated network of intercellular pathways (mechanotransduction) is initiated. In order to discuss how mechanical forces regulate cells, it is critical that rather than considering the cell only, the cell in direct physical contact with extra-cellular matrix (ECM) be considered since adhesion of cells to matrix results in the structural organization of the cell itself. Integrin binding to ECM ligands results in change in cell shape and cytoskeletal remodeling, anchoring actin filaments to adhesion sites. Since the cytoskeleton is connected to nuclear envelope, mechanical forces experienced by the cell-ECM complex, are transmitted throughout this complex. Applying external force to the cell-ECM unit causes structural rearrangement of ECM, deformation of intercellular structure and force transmission in focal adhesion sites [14].

To better understand the mechanotransduction, one might envision the EC as a circus tent and the wind blowing across the tent roof as the blood flow-induced shear stress. As the wind blows, the ropes tethering the roof (analogous to cytoskeletal stress fibres) transmit the wind force to the stakes (analogous to focal adhesion complexes) anchored in the ground around the tent base. The resulting movement of the stakes in the earth might be considered analogous to the biochemical events in the focal adhesion complexes, which then are acting as biomechanical-biochemical transducers at a distance from the point of application of the force [12] (see Figure 1-5 for visualization).

Shear-induced mechanotransduction of ECs is important in the arteries since these signals have significant effects on the ECs which may result in proliferation, apoptosis, migration, changes in permeability and structural remodeling of the wall [13]. EC responses to shear stress, determined through *in vivo* and *in vitro* studies, have shown that the following are the most affected [14]: cell shape and orientation, cytoskeletal localization, cell mechanical stiffness, cell proliferation, synthesis and secretion, endocytosis and intracellular signaling [15-17]

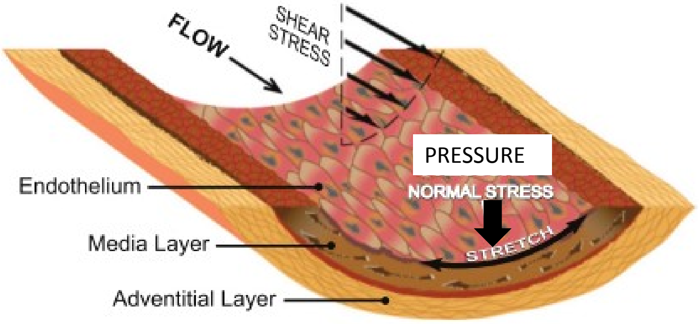

Figure 1-4 Three types of hemodynamic-induced stress on vessels are induced by wall shear stress, circumferential cyclic stretching and normal stress from hydrostatic pressure (redrawn from [18])

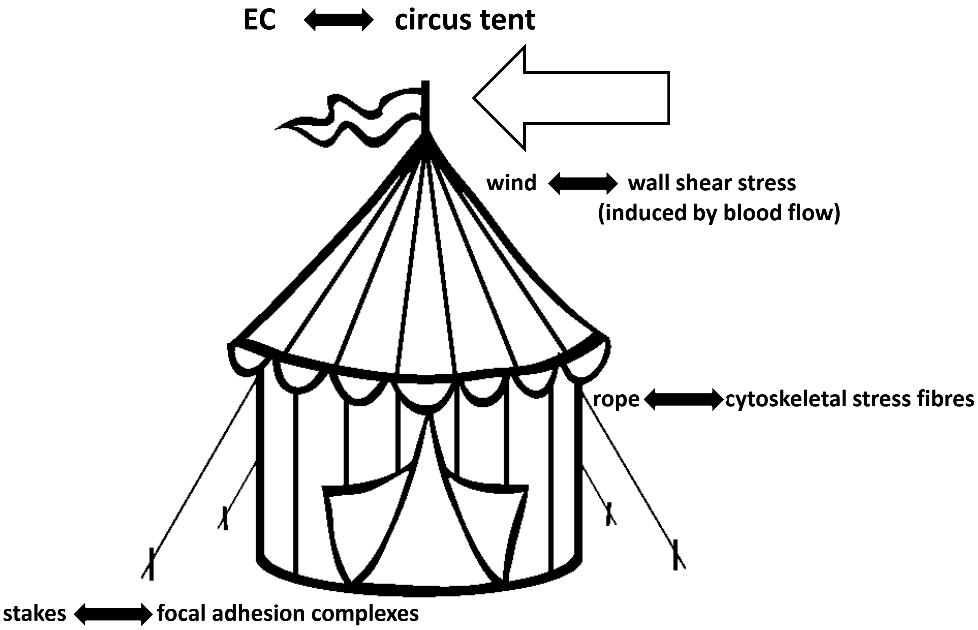

Figure 1-5 Schematic of the analogy to link the wind force effects on a circus tent to mechanotransduction in an EC

1.4 Atherosclerosis

Atherosclerosis is a slowly progressing chronic inflammatory disease of medium to large-sized arteries [2] in which an artery wall thickens (hardens in more progressive stages) as a result of plaque formation which may result in artery blockage. The exact pathophysiology of the disease is still not fully understood since many factors are associated with its initiation, development and progression.

A number of risk factors, including hypertension, obesity, diabetes, smoking, and especially hyperlipidemia, which is an elevated level of low-density lipoprotein (LDL) cholesterol, have been found to be associated with the disease [20]. It is widely accepted that dysfunction of the vascular endothelium plays a key role in the initiation of atherosclerosis [18]. The “response to injury” hypothesis proposed by Ross *et al.* [21], for the first time suggested that the injury somehow results in an alteration in endothelial cell-cell attachment or endothelial cell-connective tissue attachment due to factors such as mechanical forces, oxidized low density lipoproteins (oxLDL) or viruses [19, 21]. However, a more recent review based on experimental studies and clinical investigations, has shown that a high level of circulating LDL in blood promotes atherosclerosis by accumulation in the intima which results in LDL oxidization (oxLDL) [2]. Activation of ECs, due to immune system response at the site of injury, by components of oxLDL and disturbed flow, causes up-regulation (i.e., an increase of a cellular component) of adhesion molecules such as vascular cell adhesion molecule 1 (VCAM-1) and E-selectin; which facilitates the adhesion of monocytes and T-cells to the EC and their migration into the intima [2]. These monocytes then are stimulated by activated ECs to differentiate into macrophages which are a necessary event in initiation of atherosclerosis. These macrophages activate a type of receptor which can take up the oxLDL that has penetrated in the intima. The macrophages keep taking up the oxLDL in an unregulated fashion resulting in the formation of foam cells which are known as the hallmark of atherosclerotic lesions. A similar mechanism occurs for T-cells as well as other minor players in the process. These cellular events are more complex and are not yet fully understood. The foam cells start the development of the fatty streak which can develop into a fibrous plaque and eventually an atheromatous lesion. A schematic of major cellular events caused by the immune system in the endothelium (early stage of atherosclerosis) is illustrated in Figure 1-6.

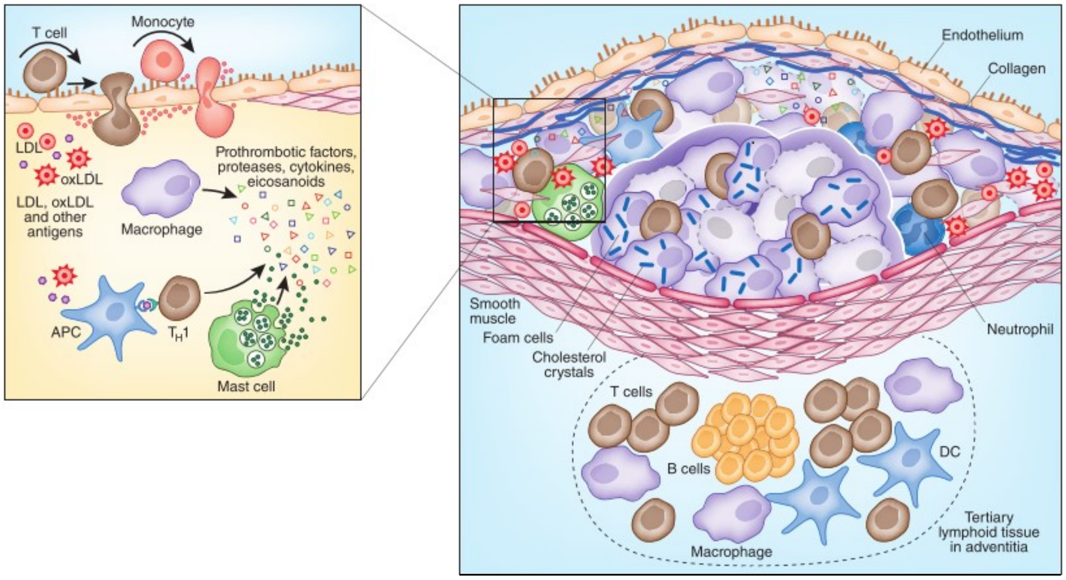

Figure 1-6 Major events in the early stages of atherosclerosis. Several types of proteins including, but not limited to, LDL, oxLDL, macrophages, T-cells and foam cells are present in the subendothelial atherosclerotic lesions (redrawn from [2]).

1.4.1 Hemodynamics and Endothelial Dysfunction

The possible role of hemodynamics (blood flow) on endothelial dysfunction was first proposed by the observation that atherosclerotic lesions do not occur at random locations but, rather, these lesions appear at the bifurcations and curved sections of the vascular network [18] (see Figure 1-7). Various *in vivo* and *in vitro* studies have shown that the flow is disturbed in the athero-prone sites of the arterial tree [9, 22-24]. The hemodynamics of these sites is characterized by disturbed regions (flow separation, recirculation zone and reattachment, see Figure 1-8 for a schematic of a step channel flow producing a disturbed flow region), low and reciprocal shear stress and high spatial and temporal gradients of the shear stress [17]. Some of the effects on the ECs that are mediated by hemodynamics are summarized in the following sections.

1.4.1.1 Effects of Flow on EC Morphology, Cytoskeletal Structure, Proliferation and Migration

Previous studies have shown that ECs subjected to laminar flow with a relatively high wall shear stress (WSS) of 10-20 dyne/cm^2 [14, 25] are aligned in the direction of the flow, with formation of long, well-organized actin filaments (in the flow direction), whereas ECs exposed to oscillatory (disturbed flow) have a morphology and random orientation of actin filaments similar to that under static control conditions [17]. Figure 1-9 shows a comparison between the morphology of actin filaments and microtubules in ECs exposed to a steady laminar WSS of 20 dyne/cm^2 (A, B and C) and a reciprocating flow with a mean WSS of 0 dyne/cm^2 (E, D and F). Additionally, ECs exposed to disturbed flow turn over (i.e., the replacement of old cells with newly generated ones) more rapidly than those subjected to a static condition or to laminar flow with relatively high WSS [26]. Laminar WSS increases EC migration in wound healing [27], whereas disturbed flow does not promote wound healing (see Figure 1-10) due to migration of ECs away from the sites with high WSS gradient (i.e., reattachment points) [28].

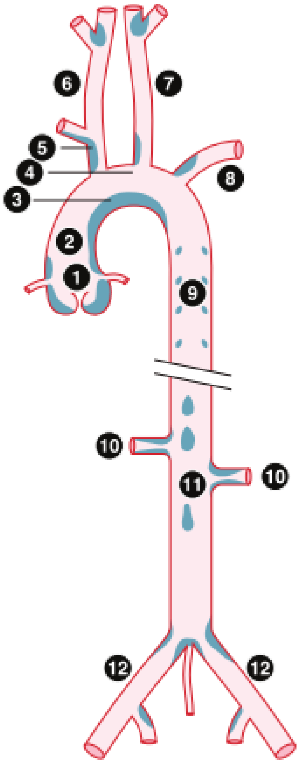

Figure 1-7 Schematic of the atherosclerotic lesions (gray) developed at the bends and bifurcations in a study of the vasculature of mice fed with high-fat atherogenetic diet (redrawn from [29])

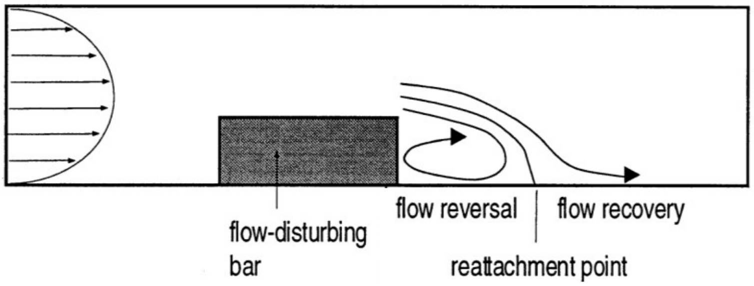

Figure 1-8 Schematic of a disturbed flow region in a channel flow. The flow becomes separated due to the flow-disturbing bar followed by a recirculation (reversal) region and the flow becomes attached again past the reattachment point. The disturbed region (the reattachment region, in particular) is characterized by having an oscillatory WSS with no distinct direction (modified from [28]).

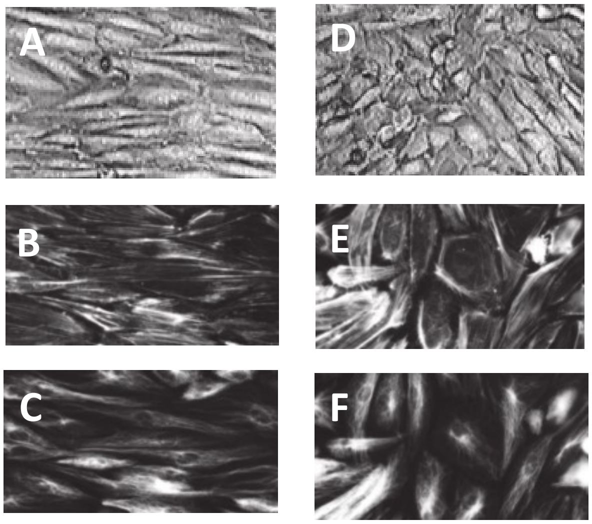

Figure 1-9 Comparison of morphology, actin filament and microtubules organization of EC monolayer (modified from [18]) exposed to a steady laminar WSS of 20 dyne/cm^2 (A, B and C) and a reciprocating flow with a mean WSS of 0 dyne/cm^2 (D, E and F)

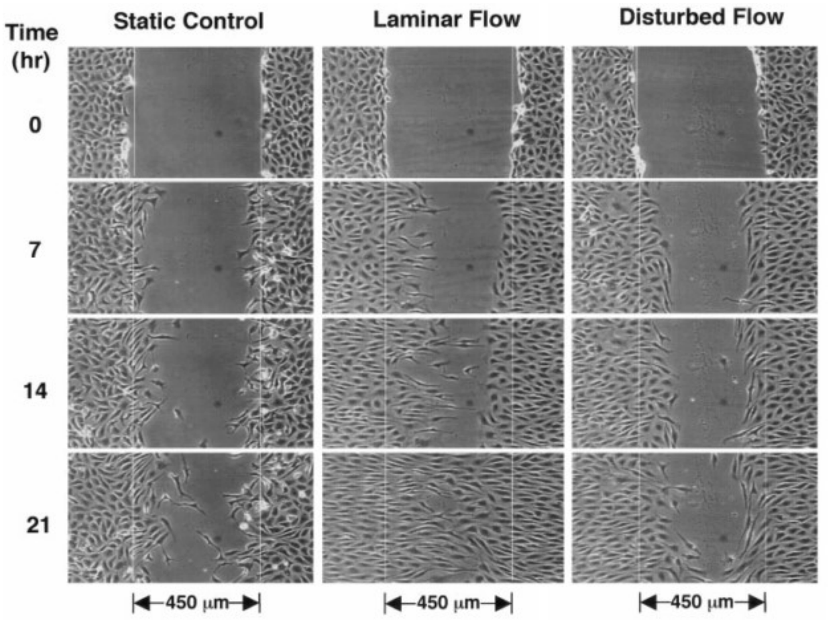

Figure 1-10 Laminar flow promotes migration of ECs in the wounded region compared to the static or disturbed flow region. These results were obtained by exposing a wounded EC monolayer to the step channel flow at the reattachment point, as well as the laminar attached region, and compared with the EC migration under static control conditions (modified from [30])

1.4.1.2 Effects of flow on EC Permeability, Junctional Proteins and Adhesion Molecules

Disturbed and low-magnitude reciprocating flows influence the EC integrity and, thus, the arterial wall permeability. In the regions prone to atherosclerosis, the particle (LDL) transit time may also increase which, consequently, increases the uptake of these particles by the arterial wall [31]. The flow also affects the junctional proteins in ECs. Connexin (Cx) 43, a type of gap junction, was upregulated in the ECs subjected to disturbed flow, but with disrupted peripheral edges, whereas ECs in uniform laminar flow had a normal distribution of Cx43 with fully-established cell communication [32]. Both *in vivo* and *in vitro* studies have shown that ECs exposed to flow with a net forward direction (e.g., a steady laminar flow) have upregulated VE-cadherin (a type of anchoring junctions) with dense peripheral junctions [33], whereas disturbed (e.g., sinusoidal) flow caused disruption of this protein at the cell borders [18]. Low and reciprocating shear stress influences the adhesion of leukocytes to ECs through up-regulation of adhesion molecules such as Intercellular Adhesion Molecule 1 (ICAM-1), Vascular Cell Adhesion Molecule 1 (VCAM-1) and E-Selectin (an adhesion molecule found on ECs only) [31] and increases the levels of transcription factors such as Nuclear factor (NF-κB, a protein involved in the response of cells to stimuli such as stress) [9]. In contrast, up-regulation of the above-mentioned proteins is absent (down-regulated) or transient in ECs exposed to laminar steady or pulsating laminar flow with net forward direction, as well as in cells under static control conditions [18, 31, 34].

1.5 Wall Shear Stress Determination

In the previous sections, the effects of flow-induced wall shear stress were briefly discussed. To experimentally determine the shear stress *in vitro*, as a product of the fluid viscosity and the velocity gradient at the wall, flow quantification techniques may be applied. In the following section, the Laser Doppler Velocimetry (LDV) method will be briefly introduced.

1.5.1 Flow Measurements Using Laser Doppler Velocimetry

The laser Doppler velocimetry (LDV), also known as laser Doppler Anemometry (LDA), is a well-developed minimally-intrusive method for measuring fluid flow velocity. When a sound or electromagnetic signal of a given frequency is emitted from a moving body, the apparent frequency to a stationary observer is different from the emitted frequency. This frequency change is known as Doppler shift. When two laser beams are brought to an intersection (i.e., focal point of the transmitting probe lens), they interfere with each other, producing a fringe pattern, which consists of alternating light and dark bands. A small particle that passes through this interference region will pass through the light and dark bands although it scatters light only in the light region. The scattered light can be collected by a receiver and detected by a photodetector. The interference pattern is due to the superposition principle of oscillation representing two electromagnetic fields [35]. The fringe spacing (the distance between the two light or dark fringes) of an LDV measuring volume is given by

$$\Delta x=\lambda/2\sin\theta \qquad (1\text{-}1)$$

where Δx, λ and θ are the fringe spacing, laser beam wavelength and the half-angle of the beam, respectively, and hence, if a particle with a speed V passes through the fringe pattern, scattered light pulses with frequency f_{ph} will be produced (due to the bright bands). The frequency of these pulses will be [35]

$$f_{ph} = V/\Delta x = 2V\sin\theta/\lambda \qquad (1\text{-}2)$$

Due to viscous effects, very small particles (e.g., 1 μm diameter) will move at essentially the same velocity as the fluid and, hence, measuring the particle velocity is equivalent to measuring fluid velocity (for visualization see Figure 1-11) [36]. If the two interfering beams have exactly the same frequency, the fringes produced at the measuring volume will be stationary which makes the detection of the velocity direction impossible. To overcome this issue, one of the beams is shifted by a Bragg cell by 40 MHz which results in fringes that are moving at a rate of 40 MHz at the measuring volume. The scattered light frequency is either above or below 40 MHz. If the particle is moving against the fringe motion, the scattered light frequency will be 40 MHz plus the actual Doppler frequency due to its velocity, otherwise it will be 40 MHz minus the particle frequency [36].

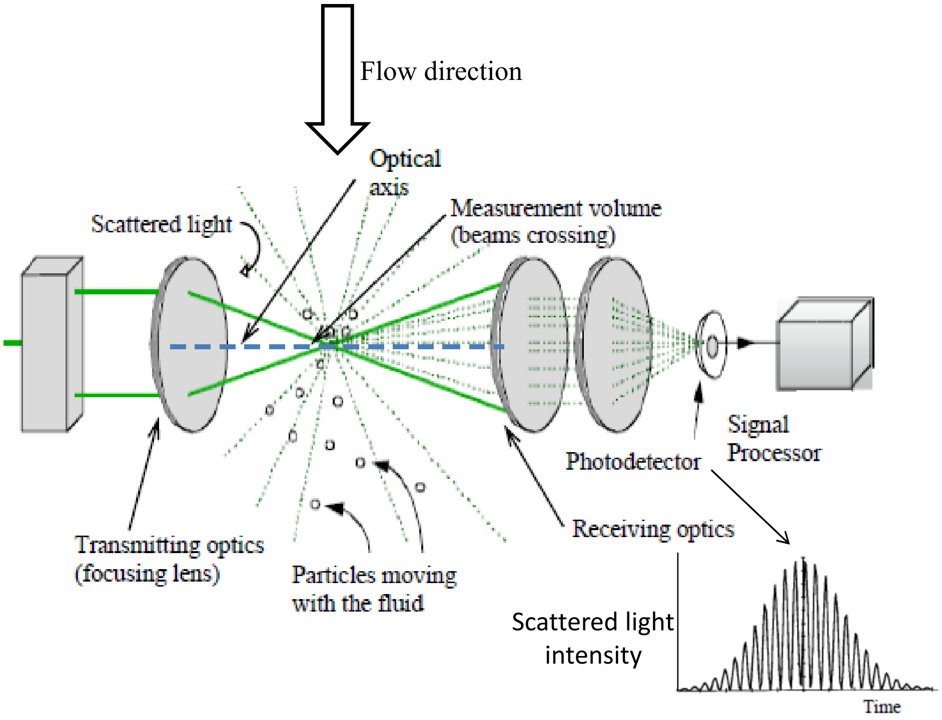

Figure 1-11 Basic components of dual-beam LDV (modified from [36])

1.6 Objectives of This Thesis

In vitro investigation of the flow effects (hemodynamics) on ECs has been widely reported in the literature. However, the quantification of the flow within the experimental facility has been mostly under-reported and WSS determinations have been based on theoretical relationships (which may not be applicable in every flow conditions), even though the flow-dependent response of EC, requires accurate flow quantification (e.g., the uniformity of the flow over the endothelium monolayer). Additionally, in order to approach physiologically relevant hemodynamic conditions for *in vitro* experiments, parameters such as Reynolds number (i.e., the ratio between the inertial and viscous forces in the flow), which determine the flow regimes need to be evaluated.

Also, no study was found in the literature in which the effects of various types of flow (in terms of the flow pattern such as steady/pulsatile and the magnitude of shear stress) on EC response has been examined with an in depth quantification of cell morphology and cytoskeletal actin filament organization. The effects of different flow regimes on PECAM-1 morphology also remain elusive since only a few studies have been conducted to investigate the PECAM-1 morphological changes under WSS [37-39].

The current research aims are to design and develop an *in vitro* facility based on the parallel plate flow chamber (PPFC) concept, to accurately quantify the flow in the span- and streamwise direction and to, consequently, determine the WSS exerted on the endothelium model. This flow measurement also aims at improving our understanding of the flow dynamics in a small-scale channel flow using the LDV technique in laminar, pulsatile laminar and low-Re turbulent flow regimes.

The well-quantified facility will then be applied to the investigation of flow effects on ECs to answer the following research questions:

- How does each flow regime affect the morphometric parameters of an EC and how significant are these changes?

- How do the cytoskeletal actin filaments remodel in response to the flow and how can these changes be quantitatively compared between different cases?

- How is PECAM-1 location influenced by shear stress? Are the junctional sites of this protein sustained under athero-prone/athero-protective flows?

1.7 Thesis Organization

The following three chapters include the articles that discuss the research completed in detail. Chapter 2 describes the design of a PPFC, development of the hemodynamic facility, biological fluid selection and characterization, and the cell culture process, along with results demonstrating the LDV velocity measurements of the flows studied and the feasibility of conducting biological experiments under the described experimental condition by presenting preliminary results of EC response to flow.

Chapter 3 describes the LDV set-up for the velocity measurement in a small-scale channel flow with an in depth discussion on a wall location determination technique, seeding particle selections, uncertainty analysis, the applied phase-averaging technique and the regression method used for determining the velocity gradient at the wall. In this chapter, also the results of the velocity measurements across the span as well as over the height of the channel for a laminar and two pulsating laminar (carotid and non-zero-mean sinusoidal) pulses are presented. A low-Re turbulent flow is also measured to demonstrate the feasibility of capturing turbulence within the PPFC. The resultant WSS from the measured cases are applied in the following chapter.

Chapter 4 represents the investigation of WSS effects (quantified in Chapters 2 and 3) on EC area, perimeter, angle of orientation, shape index, actin filament rearrangement and the PECAM-1 distribution. The experimental procedure, including the cell culture protocol, immunofluorescence, microscopy, statistical analysis, fast Fourier transform-based (FFT) quantification of actin filaments arrangement and PECAM-1 morphological changes are discussed.

Chapter 5 is dedicated to an integrated discussion of the key findings from the research conducted to examine how these findings provide an insight for better understanding of EC remodeling under mechanical stimuli and how these results may be correlated with the EC dysfunction.

1.8 Summary

Cardiovascular diseases, in which EC dysfunction is known to be a major cause, are the number one cause of death in the world. It is known that blood flow (hemodynamics) is one of the key factors which governs the EC dysfunction. Although much work has investigated the effects of flow on ECs *in vitro*, accurate quantification of the flow over the ECs and quantitative analysis of cell response in some key aspects remains elusive. The current research aims to apply quantitative methods to examine the cell response under various flow conditions through determining the morphometric parameters as well as cytoskeletal remodeling to link the descriptive and quantitative cell response due to flow with EC dysfunction. The following chapter will discuss in detail the *in vitro* hemodynamic facility, the associated experimental set-up and protocols that were developed as the initial phase of the research project.

1.9 References

[1] World Health Organization (WHO), " Cardiovascular Disease," retrieved from: http://www.who.int/mediacentre/factsheets/fs317/en/. [Accessed 3 February 2015].

[2] G. Hansson and A. Hermansonn, "The Immune System in Atherosclerosis," *Nat. Immunol.,* vol. 13, no. 2, pp. 204-212, 2011.

[3] B. Alberts, A. Johnson, J. Lewis, M. Raff, K. Roberts and P. Walter, Molecular Biology of the Cell, New York: Garland Sience, 2008.

[4] G. A. Truskey, F. Yuan and D. F. Katz, Transport Phenomena in Biological Systems, New York: Pearson, 2009.

[5] S. Tojkander, G. Gateva and P. Lappalainen, "Actin Stress Fibers: Assembly, Dynamics and Biological Roles," *J. Cell Sci.,* vol. 125, pp. 1855-1864, 2012.

[6] B. M. Gumbiner, "Cell Adhesion: The Molecular Basis of Tissue Architecture and Morphogenesis," *Cell,* vol. 84, pp. 345-357, 1996.

[7] D. E. Jackson, "The Unfolding Tale of PECAM-1," *FEBS Lett.,* vol. 540, pp. 7-14, 2003.

[8] S. M. Albelda, W. A. Muller, C. A. Buck and P. J. Newman, "Molecular and Cellular Properties of PECAM-1(endoCAM/CD31): A Novel Vascular Cell-Cell Adhesion Molecule," *J. Cell Biol.,* vol. 114, no. 5, pp. 1059-1068, 1991.

[9] S. Chien, "Mechanotransduction and Endothelial Cell Homeostasis; the Wisdom of the Cell," *Am J Physiol Heart Circ Physiol,* vol. 292, pp. 1209-1224, 2007.

[10] J. A. Berliner, M. Navab, A. M. Fogelman, J. S. Frank, L. L. Demer, P. Edwards, A. D. Watson and A. J. Lusis, "Atherosclerosis: Basic Mechanisms, Oxidation, Inflammation, and Genetics," *Circ.,* vol. 91, pp. 2488-2496, 1995.

[11] F. M. White, Fluid mechanics, New York: McGraw Hill, 2009.

[12] M. A. Gimbrone, "Vascular Endothelium, Hemodynamic Forces and Atherogenesis," *Am. J. Pathol.,* vol. 155, no. 1, pp. 537-539, 1999.

[13] D. E. Ingber, "Mechanobiology and Diseases of Mechanotransduction," *Ann. Med.,* vol. 35, pp. 564-577, 2003.

[14] R. M. Nerem, "Hemodynamics and Vascular Endothelium," *J. Biomech. Eng. ,* vol. 115, pp. 510-514, 1993.

[15] H. S. Baldwin, H. M. Shen, H. C. Yan, H. M. DeLiss, A. Chunh, C. Mickanin, T. Trask, N. E. Kirschbuaum, P. J. Newman and S. M. Albelda, "Platelet Endothelial Cell Adhesion Molecule-1 (PECAM-1/CD31): Alternatively Spliced, Functionally distinct Isoforms Expressed During Mammalian Cardiovascular Development," *Development,* vol. 120, pp. 2539-2553, 1994.

[16] L. Cao, A. Wu and G. A. Truskey, "Biomechanical Effects of Flow and Conculture on Human Aortic and Cord Blood Derived Endothelial Cells," *J Biomech.,* vol. 44, pp. 2150-2157, 2011.

[17] S. Chien, "Effects of Disturbed Flow on Endothelial Cell," *Anns. Biomed. Eng.,* vol. 36, no. 4, pp. 554-562, 2007.

[18] J.-J. Chiu and S. Chien, "Effects of Disturbed Flow on Vascular Endothelium; Pathophysiological Basis and Clinical Perspectives," *Physiol Rev,* vol. 91, pp. 327-387, 2011.

[19] R. Ross, "The Pathogenesis of Atherosclerosis: A Prospective for 1990s," *Nature,* vol. 363, pp. 801-809, 1993.

[20] Q. Guo, "The effect of Biomechanical and Biochemical Factors on endothelial Cells: Relevance to Atherosclerosis," *PhD theis,* University of Western Ontarion, London, Canada, p. 137, 2011.

[21] R. Ross, J. Glomset and L. Harker, "Response to Injury and Atherogenesis," *Am. J.*

Pathol., vol. 86, no. 3, p. 675–684, 1977.

[22] S. R. Bussolari, F. Dewey and M. A. Gimbrone, "Apparatus for Subjecting Living Cells to Fluid Shear Stress," *Rev. Sci. Instrum.,* vol. 53, no. 12, pp. 1851-1854, 1982.

[23] T. Asakura and T. Karino, "Flow Patterns and Spatial Distribution of Atherosclerotic Lesions in Human Coronary Arteries," *Circ. Res.,* vol. 66, pp. 1045-1066, 1990.

[24] C. M. Gibson, L. Diaz, K. Kandarpa, F. M. Sacks, R. C. Pasternak, T. Sandor, C. Feldman and P. H. Stone, "Relation of Vessel Wall Shear Stress to Atherosclerosis Progression in Human Coronary Arteries," *J. Atheroscler. Thromb.,* vol. 13, pp. 310-315, 1993.

[25] R. M. Nerem, M. J. Levesque and J. F. Cornhill, "Vascular Endothelial Morphology as an Indicator of the Pattern of Blood Flow," *J. Biomech. Eng.,* vol. 103, pp. 172-176, 1981.

[26] S. Chien, "Molecular and Mechanical Bases of Focal Lipid Accumulation in Arterial Wall," *Prog. Biophys. Mol. Biol.,* vol. 83, pp. 131-151, 2003.

[27] M. L. Albuquerque, C. M. Waters, U. Savla, H. W. Schnaper and A. S. Flozak, "Shear Stress Enhances Human Endothelial Cell Wound Closure in Vitro," *Am. J. Physiol.,* vol. 279, pp. H293-H302, 2000.

[28] Y. Tardy, T. Resnick, T. Nagel, M. A. Gimbrone and C. Dewey, "Shear Stress Gradients Remodel Endothelial Monolayers in Vitro via a Cell Proliferation-Migration-Loss Cycle," *Arterioscl. Thromb. Vasc. Biol.,* vol. 17, pp. 3102-3106, 1997.

[29] P. A. VanderLaan, C. A. Reardon and G. S. Getz, "Site Specificity of Atherosclerosis: Site-Selective Responses to Atherosclerotic Modulators," *Arterioscler. Thromb. Vasc. Biol.,* vol. 24, pp. 12-22, 2004.

[30] P. P. Hsu, S. Li, Y. S. Li, S. Usami, A. Ratcliffe , X. Wang and S. Chien, "Effects of

Flow Patterns on Endothelial Cell Migration into a Zone of Mechanical Denudation," *Biochem. Biophys. Res. Commun.,* vol. 285, no. 3, pp. 751-9, 2001.

[31] K. Cunningham and A. I. Gotlieb, "The Role of Shear Stress in the Pathogenesis of Atherosclerosis," *Lab. Invest.,* vol. 85, pp. 9-23, 2005.

[32] N. Depaola, P. F. Davies, W. F. Pritchard, L. Florez, N. Harbeck and D. C. Polacek, "Spatial and Temporal Regulation of Gap Junction Connexin43 in Vascular Endothelial Cells Exposed to Controlled Disturbed Flows in Vitro," *Proc. Natl. Acad. Sci. USA,* vol. 56, pp. 3154-3159, 1999.

[33] N. Sabrena, D. B. Cowan, A. I. Gotlieb and B. L. Langille, "Transient and Steady-State Effects of Shear Stress on Endothelial Cell Adherens Junctions," *Circ. Res.,* vol. 85, no. 6, pp. 504-14, 1999.

[34] T. Nagel, N. Resnick, W. J. Atkinson, C. F. Dewey and M. A. Gimbrone, "Shear Stress Selectively Upregulates Intercellular Adhesion Molecule-1 Expression in Cultured Human Vascular Endothelial Cells," *J. Clin. Invest.,* vol. 94, no. 2, p. 885–891, 1994.

[35] A. J. Wheeler and A. R. Ganji, Introduction to Engineering Experimentation, Upper Saddle River: Prentice Hall, 2010.

[36] TSI Incorporated, Operation Manual: Phase Doppler Particle Analyzer (PDPA)/ Laser Doppler Velocimeter (LDV)*,* Shoreview: MN, 2006.

[37] I. Flemin, B. Fisslthaler, M. Dixit and R. Busse, "Role of PECAM-1 in the Shear-Stress-Induced Activation of Akt and the Endothelail Nitric Oxide Synthase (eNOS) in Endothelail Cells," *J. Cell Sci.,* vol. 118, pp. 4103-4111, 2005.

[38] D. E. Conway and M. A. Schwartz, "Mechanotransduction of Shear Stress Occurs through Changes in VE-Cadherin and PECAM-1 Tension: Implications for Cell Migration," *Cell Adh. Migr.,* p. DOI:10.4161/19336918.2014.968498, 2014.

[39] D. E. Conway, M. T. Breckennridge, E. Hinde, E. Gratton and C. S. Chen, "Fluid Shear Stress on Endothelial Cells Modulates Mechanical Tension across VE-

Cadherin and PECAM-1," *Curr. Biol.,* vol. 23, no. 11, pp. 1024-1030, 2013.

[40] J. Eyckmans, T. Boudou, X. Yu, C. S. Chen, “A Hitchhiker’s Guide to Mechanobiology,” *Dev. Cell*, vol. 21, pp. 35-47.

Chapter 2

2 An *in Vitro* Hemodynamic Facility to Study the Effects of Quantified Shear Stresses on Endothelial Cells

The following chapter describes the development and validation of an *in vitro* hemodynamic facility for studying the effect of shear stress on endothelial cells. First, a detailed literature review will be presented, followed by the experimental details and results and finally, a discussion of the results obtained.

2.1 Introduction

Cardiovascular diseases (CVDs) are the number one cause of death, globally [1]. Atherosclerosis is one of the most common types of CVD that has a high rate of mortality [1]. It is an inflammatory disease of the arteries that is initiated by recruitment of monocytes and low-density lipoproteins (LDL) on the inner layer of arteries (intima including the endothelium) [2]. Numerous studies have been conducted to show that the hemodynamic interaction between blood flow and the endothelium is a significant factor in the onset of this type of cardiovascular disorder [3]. These studies have depicted that pathophysiological factors such as intracellular signaling, gene activation and immune system response due to mechanotransduction (mechanisms by which cells convert mechanical stimulus into chemical activity) activated by mechanical loading, such as shear stresses, play key roles in the pathogenesis of this disease [3-4]. Many *in vivo* and *in vitro* studies have demonstrated the effects of flow on the morphology and cytoskeletal structure of endothelial cells (ECs) [3-7]. It has been reported that shear-induced mechanotransduction of ECs may result in proliferation, apoptosis, migration, increased permeability and structural remodeling of these cells on the arterial wall [3]. Due to the restrictions associated with conducting *in vivo* experiments, *in vitro* facilities have been gaining popularity. These *in vitro* systems include macro- to micro-scale facilities [8-9]. A very wide spectrum of cellular physiological phenomenon including mechanoreception (e.g., focal adhesion, ion channels) and cellular response to such stimulation (e.g., by cytoskeleton remodeling, nitric oxide production) as a result of exposure of cells to shear stress can be investigated [4]. Despite the promising application of microfluidic systems, a lack of user friendliness and facility complexity are the major drawbacks. [5]. Macro-scale flow systems have been widely used in similar research areas and are mainly classified as; parallel-plate flow chamber (PPFC), cone-and-plate viscometer, parallel disk viscometer, orbital shaker and tubular/ rectangular capillary tube [3] (Figure 2-1).

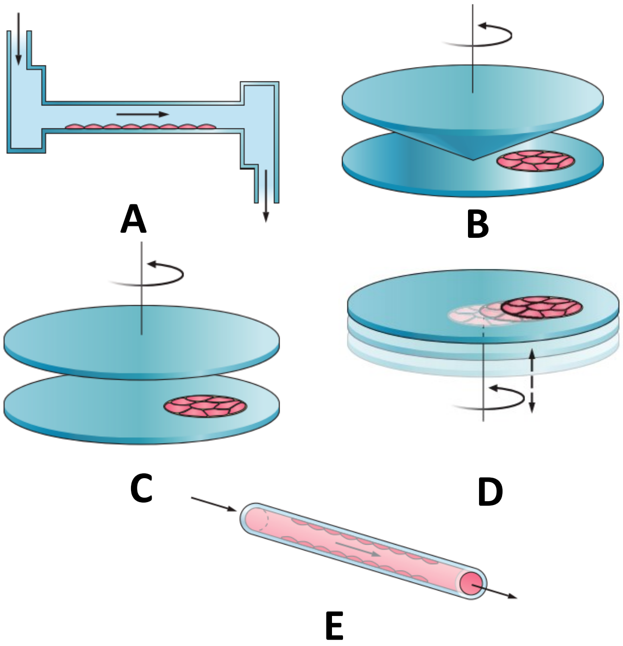

Figure 2-1 Commonly reported macro-scale hemodynamic facilities for studying the effects of hemodynamics on mechanical loading on ECs; PPFC (A), cone-and-plate viscometer (B), parallel disk viscometer (C), orbital shaker (D), tubular/ rectangular capillary tube (E) (redrawn from [3])

A uniform shear stress across the entire monolayer is not achievable by systems that use a parallel disk viscometer [6] or orbital shaker [7]; which can be considered as the main drawback of these devices. Although there have been some recent studies using capillary tubes [8]; such devices do not yield sufficient amounts of cells for some types of bioassay analysis [3]. Hence, cone-and-plate and PPFC have been the most widely reported devices for research studies.

Early detailed research on the effects of mechanical stimulation on ECs started with the application of cone-and-plate viscometers [5]. In these facilities, the flow is produced by rotation imposed around a cone axis oriented perpendicular to the surface of a flat plate. This configuration produces spatially homogenous shear stress over the ECs [3]. Davies *et al.* used this type of facility to study the effect of laminar flow (shear stress range of 8-15 dyne/cm^2) and turbulent flow on ECs [9]. Blackman *et al.* used a cone and plate viscometer device to investigate the dynamic response of cells in a hemodynamic environment with pulsatile flow [10]. Shear stress magnitudes as high as 100 dyne/cm^2 have been achieved with this apparatus [3]. Flow field measurements are more challenging in this type of tissue engineering device due to its configuration and, hence, shear stresses are mostly calculated through theoretical and mathematical relations [3, 11]. The possibility of using multiple EC coverslips and the optical path difficulties due to the geometry are the main advantage and drawback, respectively, associated with this type of apparatus [10].

Due to the restrictions briefly discussed above, PPFCs have been widely used in the study of mechanotransduction in ECs [3-4, 6, 12]. A PPFC is created as a rectangular cross section channel with an insert for cells to be placed flush with the wall flow which is driven into the chamber by a constant pressure head or by an appropriate pump. PPFCs have the following advantages over other similar *in vitro* systems: homogeneity of shear stress over the ECs, user friendliness of equipment installation [3], ease of media change [5], ease of optical access to the culture as well as for the flow measurements [4].

Studies of atherosclerotic lesions have revealed that they are not localized randomly in the arterial network [13]. Complex geometries in the arterial network, such as bends and bifurcations, are more prone to these plaques [3, 14]. These locations are characterized by having disturbed flow resulting from flow separation due to the natural geometry of the vessel (e.g., common carotid artery) or the onset of the plaque formation which acts as an obstacle to the flow [15]. The main feature of the disturbed flow is a recirculation zone due to the separation of the main flow, which results in non-uniform reciprocating shear stress. The detached flow becomes re-attached some distance downstream from the obstacle [14]. Due to the unsteady nature of blood flow, the location of the reattachment point is oscillatory [15]. ECs located in such sites are subjected to disturbed flow. Several research studies have shown that cell response to disturbed flow is significantly different from that of a laminar flow with distinct direction [4, 16]. Hence, some experimental facilities have been developed recently to mimic conditions that tend toward a realistic physiological environment (e.g., an obstacle for producing disturbed flow [3]). Depending on the requirements and goals of each experiment, corresponding devices have been designed and developed, yet, in most studies, the precise quantification of the flow (e.g., uniformity of shear stress over ECs) remains elusive. The wall shear stress for steady flows in PPFCs, cone-and-plate viscometer and tubular capillary tubes has mainly been determined using laminar flow theory [10, 12]. The shear stress magnitude has been shown to have a direct effect on mechanotransduction in ECs and, hence, it is crucial to investigate the uniformity and exact magnitude of the shear stresses associated with each device. In PPFCs, parameters such as entrance length, channel aspect ratio and Reynolds number (Re) play a key role in the flow pattern and the resulting shear stress distribution. Apart from the theoretical and numerical assessment of shear stress in such devices, other studies have taken advantage of various flow measurement techniques such as Doppler ultrasound [17], micro-Particle Imaging Velocimetry (μPIV) [18] and MEMS-based sensors [19]. The main advantage of methods such as Doppler ultrasound and μPIV is the quantification of the flow field; although, the resolution of the flow measurements in the wall region is not high [20]. MEMS-based sensors are an invasive technique that introduces a complication in the experimental set-up. The laser Doppler Velocimetry (LDV) technique is applied in the present work due to its higher accuracy in the wall region because it can resolve the velocity gradients and, hence, allow determination of the wall shear stress.

The main focus of the present chapter is to design, develop and test a PPFC channel system which has the capability of providing a wider range of accurately characterized hemodynamic conditions (compared to other reported works) including various types of physiological waveforms (e.g., carotid), flow regimes (e.g., laminar, turbulent, pulsatile, disturbed) with accurate monitoring of the ECs condition (temperature, hydrostatic pressure) and online microscopy for visualization of the ECs during the experiment. The main objective of this chapter is to demonstrate a hemodynamic facility that quantifies the uniformity of the flow as well as the shear stress, using LDV, with a real time monitoring system of the ECs. Section 2-2 will discuss the experimental details as well as the theoretical relations applied in this study. Section 2-3 will present results regarding the flow quantification as well as cell response to the flow, and, in section 2-4, a discussion of the results presented will be provided.

2.2 Materials and Methods

In this section, the experimental set-up details, cell culturing and fluid characterization will be discussed.

2.2.1 Hemodynamic Flow Facility

A PPFC was designed and developed for this study to mimic a wide variety of flow regimes and shear stresses. The closed-loop experimental set-up is a system consisting of the PPFC, a programmable physiological pump, a controlled heating unit, two pressure transducers, a media reservoir, a filtering unit, a phase contrast microscope and a LDV velocity measurement system. All of the hosing, fittings and connections were chosen from bio-compatible materials. A schematic of this set-up is presented in Figure 2-2. In the following sections each of these units will be described in detail.

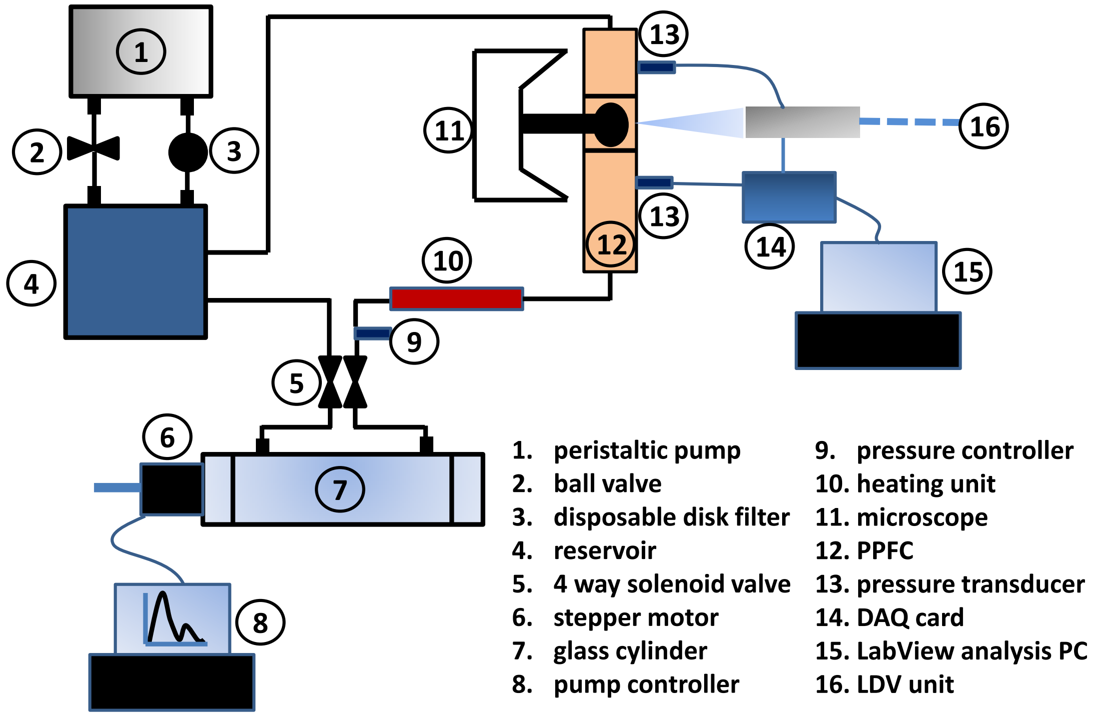

Figure 2-2 Schematic of the experimental set-up

2.2.1.1 PPFC Device

The chamber design was inspired by similar PPFCs reported in the literature (mentioned earlier in this paper) as well as pilot versions developed in the present work. The main material used for the fabrication of this chamber was ULTEM 1000 resin which is a family of polyetherimide-unfilled PEI. Table 2-1 compares some of the material properties associated with ULTEM and 316 stainless steel (data are extracted from CES EduPack, version 2013) [21].

ULTEM is a bio-compatible material, highly resistant to chemical solutions and is capable of withstanding multiple autoclaving cycles (it retains its mechanical properties in continuous exposure to heat up to 170 ºC) and, hence, it has been used in many biomedical related applications [22]. In addition, its light weight and economical processing time make this material the best candidate for the current application.

Table 2-1 Comparison of material properties between ULTEM and 316 stainless steel

Material	*ULTEM*	*316 stainless steel*
Tensile strength (MPa)	91.9-101	485-515
Density (kg/m^3)	1280	8050
Durability to water (fresh), water (salt), acids, alcohols, alkaline, organic solvents	Excellent	Excellent

The channel consists of top and bottom cavities with the coverslip test section positioned on the bottom cavity and an upstream and downstream flow development transition length of 251 mm (chosen based on theoretical calculations [23] to assure fully developed flow at the test section) and 94 mm, respectively. The channel test section has a rectangular cross section with height H=1.8 mm and width W=17.5 mm (width of the channel was chosen based on the size of the coverslip) giving a hydraulic diameter (defined as $D_h=4A_t/p_t$ where A_t and p_t are the area and wetted perimeter of the test section) of 3.26 mm. This hydraulic diameter is in the range of physiological artery sizes (e.g., proximal left anterior descending coronary artery has diameter of 3.7±0.4 mm [24]). The inlet and outlet are 3.18 mm and 6.35 mm diameter female threaded NPT connections. There is a smooth transition from a circular to a rectangular cross section and *vice versa*, upstream and downstream of the channel, respectively, from/to the hose installation. The test working section is made from precision glass (6 mm thick, Angstrom Precision Optics Inc., USA) for optical access on the top cavity and there is a shallow square insert 22 x 22 mm in the bottom cavity for installation of 0.22 mm thick coverslips to be flush mounted with the lower wall of the channel. Vacuum silicon grease (Dow Corning, USA) was applied to prevent any leakage. Under the test section on the bottom cavity, another cylindrical cavity (53 mm diameter, 15.9 mm depth) was fabricated for microscopy access. These dimensions have been chosen based on typical microscope objective sizes for visualization of the coverslip in the test section. In order to mimic occlusion conditions (disturbed flow), an insert for an obstacle block (316 stainless steel, 17.5 x 17.5 mm in plane) is fabricated upstream of the test section. Using various block heights, an occlusion up to 70% is achievable. The schematic of the obstacle location with respect to the coverslips is shown in Figure 2-3.

The top and bottom cavities are connected together by evenly-distributed stainless steel fine-threaded screws. Additional compression is provided by plastic screws from the two ULTEM parts of the top cavity along edges of the glass canopy. A viton o-ring cord seals the gap between the top and bottom cavities. A schematic of the PPFC is depicted in Figure 2-4.

2.2.1.2 Physiological Wave Form Pump

A positive displacement pump (CompuFlow 1000 MR, Shelley Medical Imaging Technology, Canada) was used to produce the flow. The pump was capable of producing steady flows (volume flow rate Q=0.1-50 ml/s), realistic physiological flows (e.g., carotid), and user defined waveforms (e.g., non-zero mean sinusoidal waveforms). The pump was controlled by SimuFlow II Waveform Editing Software (Shelley Medical Imaging Technology, Canada). A snap action switch (Omron Basic, USA) initiates the pump motion. A bio-compatible 4 way double solenoid valve was designed and manufactured in-house from ULTEM for switching the flow direction at the end of each stroke, assuring unidirectional flow.

2.2.1.3 Heating Unit

To keep the ECs at the physiological temperature (37 ºC), a heating unit, consisting of a 316 stainless steel in-line tubular heater (120 V/600 W, Zesta Engineering, USA), 1.6 mm diameter T type thermocouple (316 stainless steel, Zesta Engineering, USA) and a proportional–integral–derivative (PID) single channel heater controller (Zesta Engineering, USA) with an accuracy of ± 0.1 ℃ was used. The heater was installed in the flow circuit, between the pump and the channel. For further heater power adjustment to accommodate various flow rates, a variable transformer (0-140 V, Superior Electric, Canada) was used.

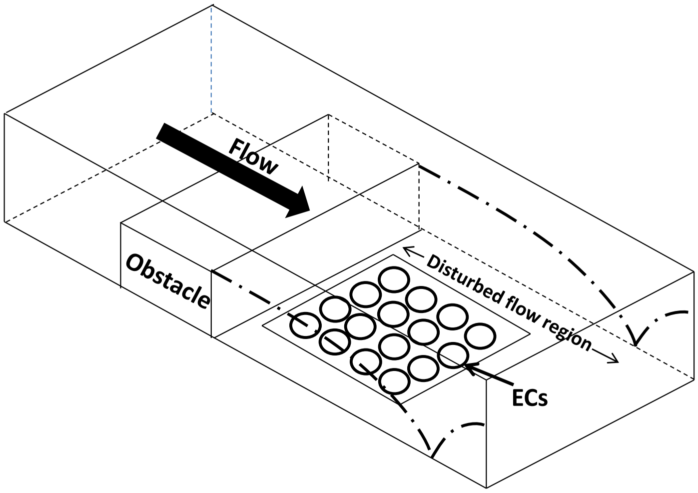

Figure 2-3 Schematic of the occlusion mimicking obstacle location upstream of the ECs (Note: not drawn to scale)

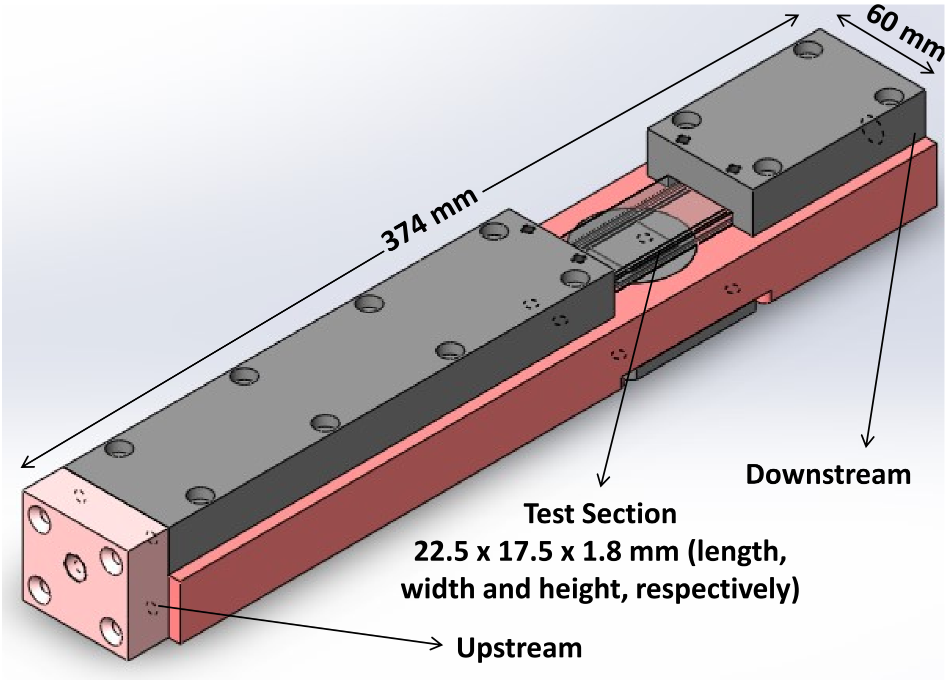

Figure 2-4 Schematic of the parallel plate flow chamber

2.2.1.4 Pressure Transducers

To monitor the hydrostatic pressure acting on the ECs, as well as the flow waveform, two pressure transducers (PX 309-005G5V, Omegadyne, USA) with an accuracy of ±2% full scale output (FSO) and a response time < 1 ms were implemented. These transducers were capable of measuring pressures in the range 0-34.37 KPa (0-5 psi) and were installed upstream and downstream of the test section. Such a response time was crucial for monitoring the pulsatile flow measurements. A DAQ card (6042E, National Instrument, USA), a shielded I/O connector block and a 68-Pin connector (SCB-68, National Instrument, USA) were used to connect the transducers to a PC. A LabVIEW (version 7.2, National Instrument, USA) program was written for processing of the signals. For pulsatile flows, a MATLAB (Total Academic Headcount license, 2013a) code was also written for phase-averaging such signals.

2.2.1.5 Filtering Unit

In order to filter the media during the experiment to eliminate possible biological contamination a secondary loop parallel to the main flow loop was created by a peristaltic pump (Piper Pump, Canada). The media was circulated from/to the reservoir through a sterile Mellipak filtering unit (0.45 μm pore size, Sigma Aldrich, USA).

2.2.1.6 Microscopy

In order to visually observe the ECs (e.g., morphological change monitoring) during the experiment, a Micromaster infinity optics microscope (Fisher Scientific Inc., USA) was used. The microscope stage was modified in-house for installation of the test rig under the microscope. An aluminum stage was designed with a circular opening (to accommodate for the PPFC geometries) for this set-up to support the PPFC.

2.2.1.7 Fittings and Hosing

All the fittings (Cole-Parmer, Canada) and hosing (C_FLEX, Cole-Parmer) were chosen from a range of bio-compatible materials with inner diameter of 6.35 mm.

2.2.1.8 Biological Compatibility and Sterilization

To assure the compatibility of the facility for mechanobiological experiments and considering the corrosive behavior of the media used in the experiments, the individual channel components were maintained in the media in sterile conditions and the resultant media was tested for biocompatibility using ECs in petri dishes. A comparison between the cells kept in the fresh media and those in the media in contact with the experimental facility demonstrated no difference between cell morphology and growth, revealing the inert properties of the experimental materials in contact with the cell media.

All the parts and tools that could not be autoclaved were steam sterilized. Prior to each experiment, a cold sterilization method was used to clean the system. 70% Ethanol was circulated in the flow loop for 30 min and then, the system was rinsed before being washed three times with sterile water.

2.2.1.9 Fluid Selection and Characterization

Dulbecco's Modified Eagle Medium (DMEM) solution was used for the flow experiments. This media was prepared in-house for each experiment. 12.78 g/L DMEM powder (without phenol red, Wisent, USA), 10 mM/L HEPES (Wisent, USA), and 10 ml/l Antibiotic-Antimycotic (the original solution containing 10,000 units/mL of penicillin, 10,000 μg/mL of streptomycin, and 25 μg/mL of Fungizone, Life Technologies Inc., Canada) were dissolved in nano-pure water. After the media was prepared, the pH level was adjusted to 7.4 by adding NaOH pellets to comply with physiological conditions. Characterization of the media, including density and viscosity measurements, as well as its adaptability with cells was carried out. The EC viability in this media was examined and no difference was observed between the cells grown in the described fluid and those commercially-available DMEM media (Life Technology, Canada). The viscosity was measured using an Ubbelohde viscometer in a 37 ºC water-bath and it was found to be 0.737±0.0012 mPa.s which is in the range of similar solutions in other studies [17, 25]. Although this value of viscosity is lower than blood viscosity (3-4 mPa.s) [26], it has been widely accepted [18, 27-28] since the WSS is the product of the dynamic viscosity and the velocity gradient at the wall and, hence, the increase in the velocity gradient at the wall can compensate for the lower viscosity magnitude. Although Dextran has been widely used to increase the media viscosity to match the rheological properties of blood, it has been shown that under both static and flow conditions, Dextran has adverse effects such as decreasing the cell's ability to attach to culture plates and increasing the protein and mRNA expression of intercellular adhesion molecule 1 (ICAM-1) [29]. Hence, in this study Dextran was not used. Also, although blood is a non-Newtonian fluid, in arteries larger than 250 μm it can be considered as a Newtonian fluid [26] and has been treated as such in many *in vitro* numerical or experimental studies [3, 10, 16, 20, 30]. The density of the media was measured to be 997.96±0.12 kg/m^3.

2.2.2 Cell Culture

Porcine Aortic Endothelial cells (PAECs) were chosen for this study as their response to shear stress has been well characterized [31]. ECs were cultured on 100 mm culture dishes using DMEM and 20% fetal bovine serum (FBS) and were kept at 37 ºC in a 5% CO_2 incubator until confluent. The cell media was changed every 48 hours. Once confluent, the cells were detached by 0.25% Trypsin-EDTA (Life Technologies Inc., Canada) and plated on 22 × 22 mm (number 2) autoclaved coverslips (VWR, USA) using DMEM and 10% FBS and kept in the incubator until confluent. Having a monolayer of ECs was an essential requirement for this experiment since ECs *in vivo* are the innermost monolayer of arteries which are exposed to direct WSS due to the blood flow [2]. Coverslips were then mounted in the hemodynamic channel for flow exposure experiments. At the end of each experiment, the cells were fixed with 4% Formaldehyde in 1 x phosphate buffered saline (PBS).

2.2.3 Velocity Measurement and Shear Stress Determination

2.2.3.1 Flow Field Measurements

In order to non-invasively measure velocity and, hence, wall shear stress, the LDV method was used. This method is based on a Doppler frequency shift. When two laser beams intersect, a fringe pattern forms due to the coherence of the laser beams and when a very small seeding particle passes through these fringes, it generates a Doppler shift in the scattered light frequency proportional to its velocity [32-33] The LDV system in this study was consisted of a 5 Watt water-cooled Argon-ion laser (COHERENT, USA), a 2-component (4 beams) probe (TRx20, TSI, USA) with measurement volume diameters of 64 μm and 68 μm (for the green and blue beams, respectively) and measurement volume length of 1.1 mm, a photo detector multiplier (PDM 1000, TSI, USA), a FSA 3500 signal processor (TSI, USA) and FlowSizer software (version 2.0.4) [34]. Two pairs of shifted and unshifted beams (green at 514.5 nm and blue at 488.0 nm) were used. A Bragg cell was used to shift the frequency of each color by 40 MHz to eliminate directional ambiguity. Titanium dioxide particles (Showa America, USA) with size distribution ranging from 0.24-0.47 μm were used for seeding. Near wall velocity measurements were carried out in the PPFC within the EC test section. The probe was mounted on a multi-axis traverse (THORLABS, USA) with positional accuracy of ±5 μm to assure accurate translation in all three directions. A schematic of the LDV layout is depicted in Figure 2-5.

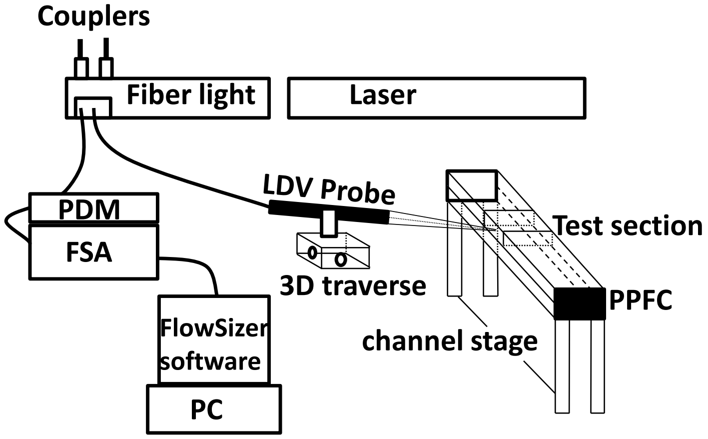

Figure 2-5 Layout of the LDV system component and probe positioning with respect to the PPFC test section

Determination of the distance from the wall to the measurement volume was of significant importance in this study due to the confined geometry of the channel. In the literature, it has been reported that there is a distinct frequency shift associated with the wall once the LDV beam is traversed into the wall [35- 37]. An oscilloscope was used to monitor the signal intensity from the PDM and, hence, the location of the beam measurement volume with respect to the wall (coverslip) was determined to within ±27 µm.

To avoid the laser beams encountering the lower wall (e.g., coverslip) of the test section, the probe was tilted downward by 4.5° (slightly greater than the beam half angle, 3.9°) (Figure 2-6). Although tilting the angle of the probe did not vary the u component measurements, the v component measurements were in error by approximately 0.3%. Typical data rates were 50-100 Hz near the wall and 500-2000 Hz further from the wall. All the acquired data were analyzed with MATLAB (Total Academic Headcount license, 2013a).

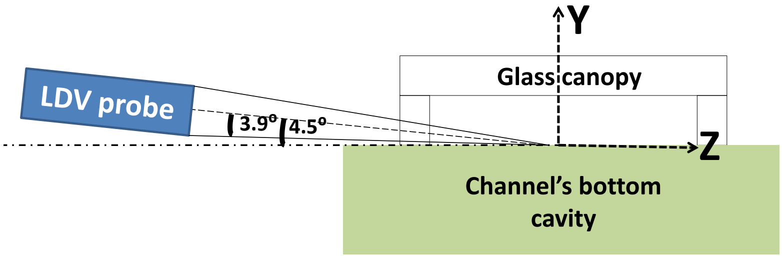

Figure 2-6 Probe configuration for two component velocity measurements

2.2.3.2 Analytical solution of two-dimensional laminar flow in a rectangular channel

To compare the experimental data for steady laminar flow with numerical results, an analytical solution of two-dimensional fully developed laminar flow in a rectangular channel was applied as below [26].

$$U(y,z) = \frac{\Delta P H^2}{8\mu L}\left(1 - \frac{4y^2}{H^2}\right) - \frac{4\Delta P H^2}{\mu L}\sum_{n=0}^{\infty}\frac{(-1)^n cosh\left(\frac{(2n+1)\pi z}{H}\right) cos(\frac{(2n+1)\pi y}{H})}{(2n+1)^3\pi^3 cosh(\frac{(2n+1)\pi W}{2H})} \tag{2-1}$$

where U(y,z), ΔP, μ and L are the streamwise velocity at any specified y and z coordinate, the pressure loss along (x) the channel, dynamic viscosity and channel length, respectively. The subtracted modifying terms are due to the application of the boundary conditions in the solution for a homogenous second order partial differential equation

(PDE) of two-dimensional laminar channel flow. Using Equation 2-1 the wall shear stress acting upon the top and bottom walls of the channel can be calculated by Equation 2-2.

$$\tau_{wall} = \mu\frac{\partial U}{\partial y}|_{y=\pm H/2} = \frac{\Delta PH}{2L}\left[1 - 16(\frac{H}{W})\sum_{n=0}^{\infty}\frac{(-1)^n tanh\big((2n+1)\pi W/2H\big)}{(2n+1)^3\pi^3}\right] \tag{2-2}$$

For larger aspect ratio channel flows (W/H>50), Equation 2-2 simplifies to

$$\tau_{wall} = {}^{6Q\mu}/_{WH^2} \tag{2-3}$$

2.3 Results

2.3.1 Fluid Dynamics of the Flow in the PPFC

In this section, the fluid dynamics measurement results for the flow in the PPFC, including steady laminar and pulsatile (Carotid waveform) flows over the ECs, and shear stress determination will be presented. Experimental uncertainties are discussed in detail in section 3.3.

2.3.1.1 Steady laminar flow

2.3.1.1.1 Uniformity of the flow

To assess whether fully developed uniform flow conditions existed in the test section, vertical and lateral profiles of the streamwise velocity (U) component were measured at three different streamwise locations above the coverslip. Streamwise velocity measurements were taken at x/L=0, 0.5 and 1, z=0 and 0<y<900 µm (0<2y/H<1). Similarly, spanwise measurements were taken at x/L=0, 0.5 and 1, -1<2z/W<1 and y=300 µm (2y/H=1/3). Since the cells are placed on the coverslip at 2y/H=0 it was appropriate to take the spanwise measurements as close as possible to the coverslip. 2y/H=1/3 was chosen to ensure the accuracy of the measured velocity data as there is a wall effect associated with the experimental measurement technique [37]. A schematic of the measurement locations in the test section is shown in Figure 2-7.

The experimental results and the analytical solution for the time-averaged mean streamwise velocity U at locations D, E and F for the volume flow rates Q=1.28 ml/s and 12.8 ml/s are shown in Figure 2-8. The Re for a channel flow is defined as $Re = U_b (2\delta)/\nu$ or $Re_0 = U_0\delta/\nu$, where U_b, U_0, δ and ν are the channel bulk velocity (defined as volume flow rate divided by the channel test section cross-sectional area), center-line velocity, channel half height ($\delta = H/2$) and kinematic viscosity of the fluid, respectively [38]. The flow is reported laminar for Re<1350 in channel flow [38]. The Re associated with the measured laminar flow rates are 100 and 990 ensuring that the flow is fully laminar.

The time-averaged mean velocity (U) in the span of the channel (at locations A, B and C), for both Re values are presented in Figure 2-9. These measured values are also compared (see Figure 2-9) with the analytical solution from Equation 2-1 and the differences are within experimental error.

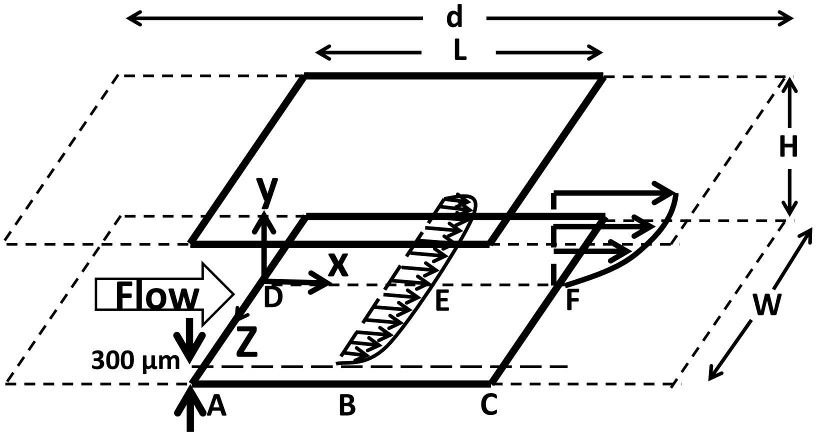

Figure 2-7 Reference coordinate system, working section dimensions (glass working section length d=65 mm, test section length, width and height, L, W and H=22.5, 17.5 and 1.8 mm, respectively), measurement location for spanwise u-velocity at x/L=0, 0.5 and 1, 2y/H=0.33 (A, B and C) and measurement location for streamwise u-velocity x/L=0, 0.5 and 1, z/W=0 (D, E and F).

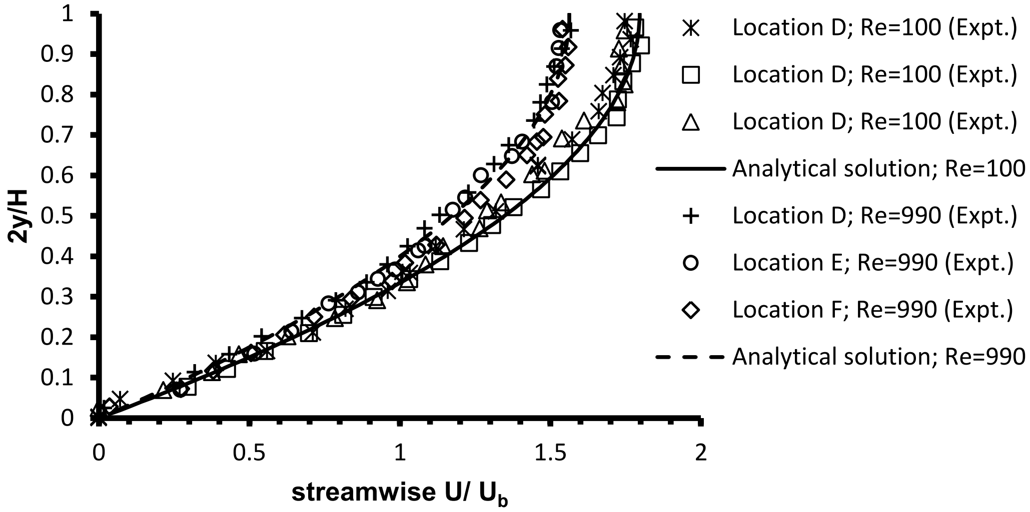

Figure 2-8 Comparison of streamwise time-averaged mean velocity U normalized by U_b (bulk velocity) with the analytical solution from Equation 2-1 for $0<2y/H<1$ at locations D, E and F for Re=100 and Re=990. The average deviation of the experimental data points from the analytical solution for Re=100 at locations D, E and F are 4.5, 1.8 and 2.6%, respectively. Similarly these values for Re=990 are 1.8, 3.2 and 6.2%, respectively.

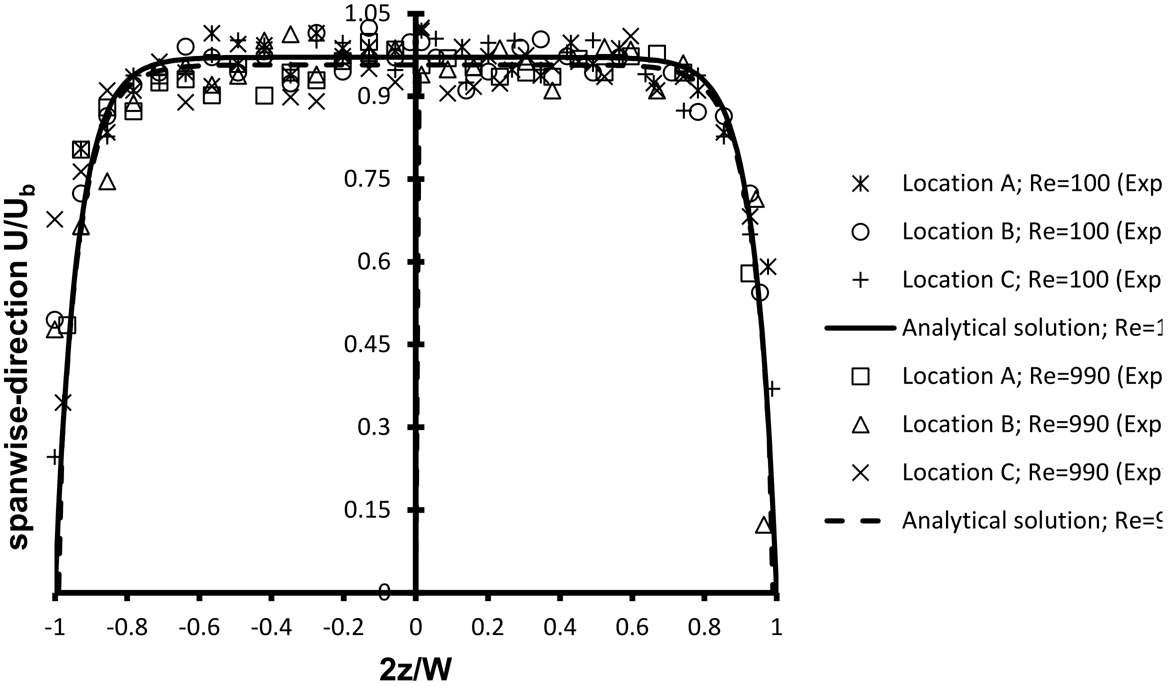

Figure 2-9 Comparison of spanwise direction time-averaged mean velocity U normalized by U_b with the analytical solution from Equation 2-1 for -1<2z/W<1 at locations A, B and C for Re=100 and Re=990. The average deviation of the experimental data points from the analytical solution for Re=100 at locations A, B and C are 3.6, 3.4 and 1.7%, respectively. Similarly these values for Re=990 are 2.4, 2.9 and 4.4%, respectively

2.3.1.1.2 Wall Shear Stress (WSS)

WSS is defined as

$$\tau_w = \mu \, {}^{\partial U}/_{\partial y} \, |_{y=0} \tag{2-4}$$

and, in the present work, it was quantified by polynomial curve fitting to the vertical profiles of the streamwise velocity. In the case of laminar channel flow, the profile is known to be parabolic and, hence, a quadratic curve was fitted (over the wall region to channel center-line) to calculate the gradient of the velocity at the wall. The analytical solution for WSS using Equations 2-2 and 2-3 was also calculated for both flow rates for comparison purposes. These values are presented in Table 2-2.

Table 2-2 Summary of experimental results and analytical solutions of WSS for Re=100 and Re=990 (the three values for each Re correspond to locations D, E and F)

Re	Experimental WSS (dyne/cm^2) (2-4)	Average Experimental WSS (dyne/cm^2)	Analytical solution (dyne/cm^2) (2-2)	Analytical solution (dyne/cm^2) (2-3)	⎮Error⎮ % between experiment and analytical solution (2-2)	⎮Error⎮ % between experiment and analytical solution (2-3)
100	1.13±0.17	1.13±0.17	1.17	0.99	3.54	12.39
	1.09±0.16				7.34	9.17
	1.18±0.18				0.85	16.1
990	11.68±1.75	11.48±1.72	10.45	9.98	9.53	14.55
	11.36±1.70				8.01	12.14
	11.41±1.71				8.41	12.53

2.3.1.2 Pulsatile flow

Due to the pulsatile nature of blood flow *in vivo*, it is critical to expose ECs to physiological waveforms. To demonstrate the capability of the current system for producing flows that replicate the hemodynamic forces of realistic physiological cases, the instantaneous streamwise velocities (u) associated with a carotid waveform (Re_{-min}=230 and Re_{-max} =1260) were measured and quantified at location E (the coverslip center). A phase-averaging method was applied for processing of this flow using MATLAB. By applying phase-averaged Reynolds decomposition [39] to the measured velocity time history values

$$u = U + \tilde{u} + u'; \qquad < u >= U + \tilde{u} \tag{2-5}$$

where u, U, $\tilde{u}$, u' and <u> are the u-component instantaneous velocity, the global time-averaged mean velocity, the periodic bin-average velocity, the turbulent fluctuations of the velocity and phase-averaged velocity, respectively. Since the flow was laminar, the u' term was zero [40].

For each measurement location, 200 waveform cycles [20, 41] of period (T) of 0.92 s were averaged within 23 bins per cycle. The LDV signal was triggered with a signal from the pump to synchronize the start of each cycle. After all of the data were phase-averaged, the velocities belonging to the corresponding bins across the channel half-height were graphed to demonstrate the temporal change in the velocity profile, as illustrated in Figure 2-10. U_b is compared with a phase-averaged experimental data measured at 2y/H=1 (channel center-line) in Figure 2-11 and both profiles show two peaks corresponding to the systolic [26] (absolute maximum) and early diastolic [26] values (local maximum) at t=0.16 and 0.44 s. No phase shift is observed when comparing the two profiles, although some attenuation of U_b is observed in the measured velocity which manifests the effects of the walls and the distance from the pump to the test section (k/L≈45, where k is the distance from the pump to the test section).

Phase-averaged u-velocity profiles (<u>) at 2y/H=0.33, 0.66 and 1 for this flow are shown in Figure 2-12. Based on the systolic peak location, no phase shift is observed in any of these graphs. At closer distances to the wall, the mean cycle velocity decreases due to the effect of shear flow near the wall causing a greater cycle-mean velocity at the wall. This effect is opposite closer to the channel center-line; comparing the profiles for 2y/H=0.66 with 1 it is clear that in the former, the velocity nearly reaches its maximum value (which occurs at 2y/H=1) and there is no significant development in the profile after t/T>0.35 (diastolic phase) for these two profiles. The systolic flow continues to grow until it reaches the maximum at the centerline. Despite the fact that no significant change is visible in the diastolic flow at 2y/H=0.66 and 1, the dissipated diastolic peak starts appearing again at 2y/H=1 similar to the profile of pump bulk velocity (Figure 2-11).

The <u> profiles at t/T=0.28, 0.44 and 0.87 across the channel height (0<y/H<1) are shown in Figure 2-13. These three graphs are presented in this figure to compare the phase-averaged (<u>) streamwise profiles at systolic deceleration (t/T=0.28), with early and late diastole (t/T=0.44 and 0.87, respectively). By graphing the velocity profiles for all of the bins, it was found that the profiles at 0.3<t/T<0.39 and 0.7<t/T<0.91 slightly deviate from the parabolic profile observed with steady flow and become “bell-shaped”. From Figure 2-13, it is evident that at t/T= 0.28 and 0.44 the velocity appears parabola-like and similar to the laminar steady channel flow, whereas at t/T= 0.87 the profile slightly deviates from a parabolic shape. These deviations correspond to the deceleration phase of the flow where the velocity gradient becomes negative and the pressure gradient tends to slightly increase in the viscous boundary layer and, hence, the viscous boundary layer does not have enough time to fully grow unlike the inertial core which has a distinct parabola-like shape [26, 42]. The shear stresses were calculated by a best-fit second-order polynomial interpolation method to determine the velocity gradients at the wall. For the profiles that deviated from a parabolic shape, in order to increase the accuracy only data close to the wall (2y/H<0.33) were taken for the shear stress calculations.

The phase-averaged shear stress $<\tau_w>$ is shown in Figure 2-14. The general profile shape is similar to the <u> profiles at locations close to the channel centerline and both systolic and diastolic peaks are visible in the graph. The WSS is positive indicating a unidirectional WSS over the ECs with an average value of 10.66 dyne/cm^2. The reported value for the mean WSS in the common carotid artery (CCA) is 4-15 dyne/cm^2 (depending on age, sex and health condition) [43-44].

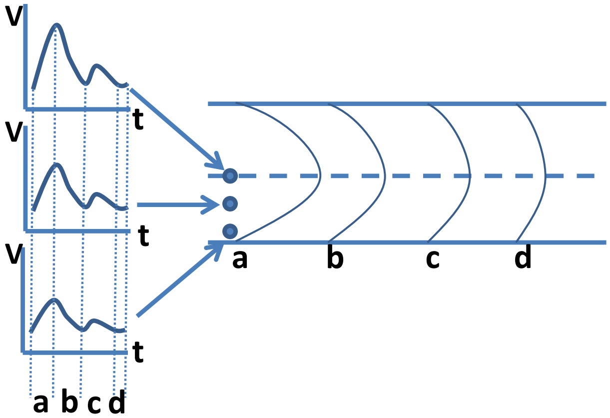

Figure 2-10 Schematic of phase-averaged velocity profile extracted from spatial LDV measurements. Profiles a, b, c and d correspond to phases a, b, c and d of the pulse across the channel height

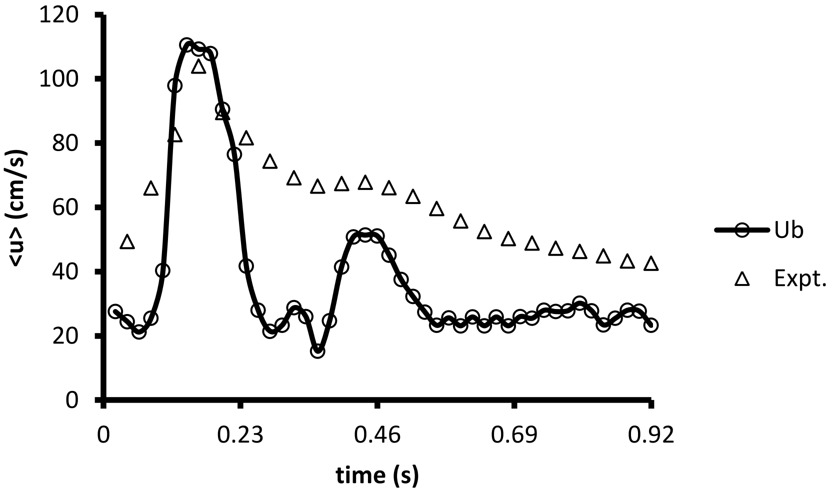

Figure 2-11 LDV measured phase-averaged streamwise velocity <u> at 2y/H=1 vs. U_b (bulk velocity)

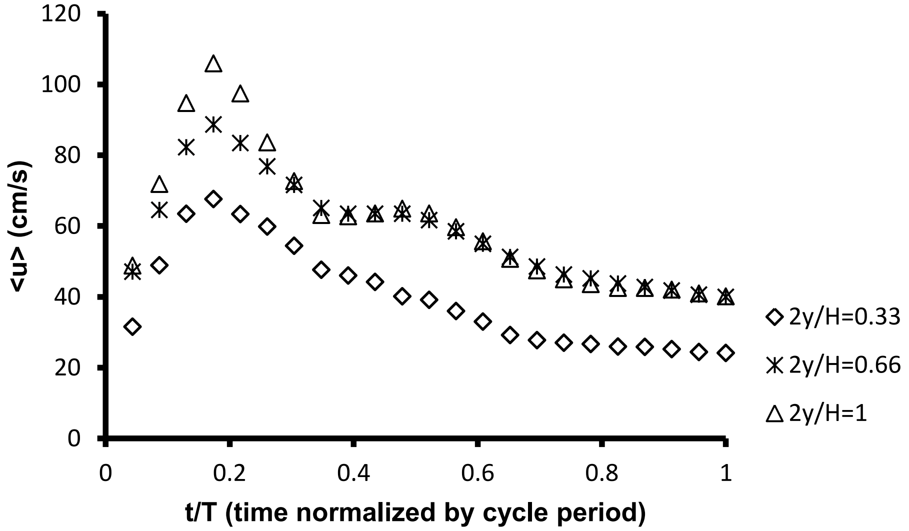

Figure 2-12 LDV measured phase-averaged streamwise velocity <u> at 2y/H=0.33, 0.66 and 1

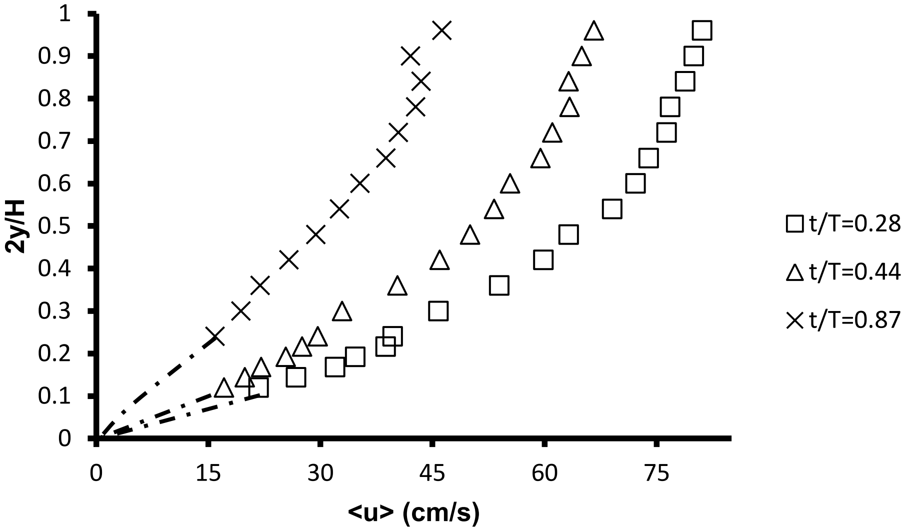

Figure 2-13 <u> profiles across the channel height (0<y/H<1) at t/T=0.28, 0.44 and 0.87 for carotid waveform

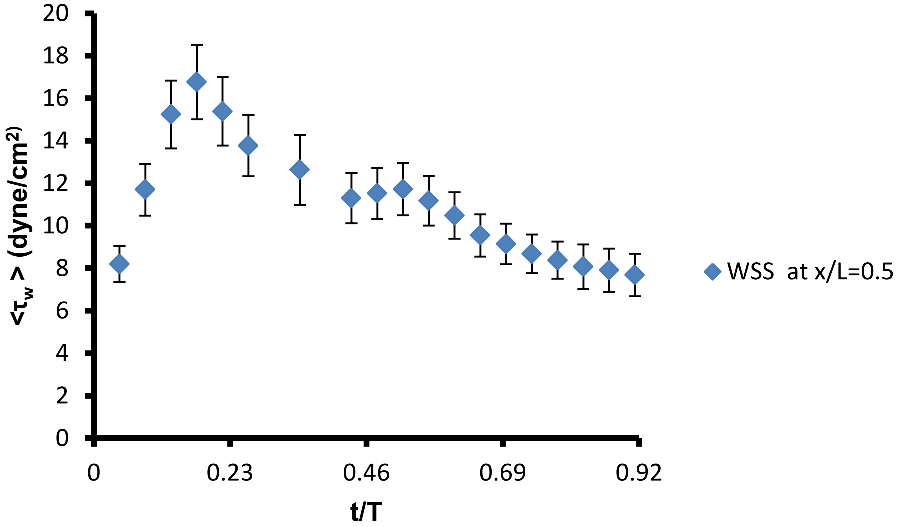

Figure 2-14 Phase-averaged wall shear stress < τ_w > for carotid wave form at x/L=0.5 (error bars indicating the measurement uncertainty)

2.3.2 Hydrostatic Pressure Measurements

ECs *in vivo* are exposed to a hydrostatic pressure of 2 to 140 mm Hg under normal conditions [48] and so it was important to monitor the pressure values at the test section to ensure physiological pressure range conditions were maintained. The two pressure transducers, one 80 mm upstream and the other 50 mm downstream of the test section (coverslip) recorded hydrostatic pressure values of 20-80 mmHg (depending on the height where the channel was located) for the two steady flow cases (Re=100 and Re=990) which complies with physiological conditions. Similar to pulsatile velocity measurements, by applying phase-averaged Reynolds decomposition to the measured pressure time history values

$$P_t = P + \tilde{p} + p'; \qquad < P >= P + \tilde{p} \tag{2-6}$$

Where P_t, P, $\tilde{p}, p'$ and <P> are the instantaneous pressure, the global time-averaged mean pressure, the periodic bin-average pressure, the random fluctuations of the pressure and phase-averaged pressure, respectively. Since the flow was laminar, the p' term was zero (pressure time history). Figure 2-15 shows the phase-averaged hydrostatic pressure <P> at the upstream and downstream ends of the PPFC test section.

These graphs demonstrate that the pressure profile follows that of U_b and also that the values are in the physiological range. In systolic acceleration (0<t/T<0.10) the two pressure profiles have a larger deviation from each other (($<P_{upstream}>$-$<P_{downstream}>$)/$<P_{upstream}>$ × 100≈14%) becoming less significant (≈3%) from 0.1<t/T<0.53 and from then until the end of the cycle, the deviation again becomes larger (≈9%). A phase shift of Δt/T=0.02 is visible between the two profiles in the first peak (t/T=0.1) and no phase shift is observed in the second peak (t/T=0.43). These graphs also confirm the attenuation of the original waveform produced by the pump (see Figure 2-11).

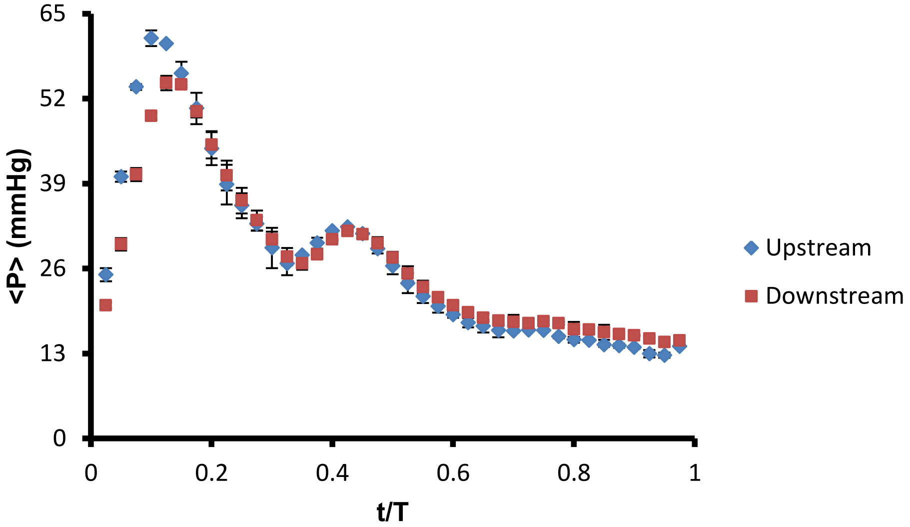

Figure 2-15 Phase-averaged hydrostatic pressure <P> upstream and downstream of the test section (error bars are indications of standard deviations of the data range within a bin)

2.3.3 EC Survivability and Responses in the Hemodynamic System

Cell remodeling has a complicated pattern due to mechanotransduction. Once the mechanical stimulus due to shear stress is transmitted to the cell, F-actin microfilaments start to change their orientation and remodel in response to the hemodynamic forces [25]. Hence, it is important to monitor the EC morphological changes during the experiment.

2.3.3.1 EC Viability in the PPFC

A confluent monolayer of PAECs on the coverslip was installed in the PPFC under static conditions to monitor cell viability in the test rig environment. No morphological or cell-density related changes were observed between the cells kept in the test rig and those kept in petri dish.

2.3.3.2 Time-dependent Morphological Response of ECs to Flow

As mentioned earlier in this paper, one of the main features of the current hemodynamic facility is the online microscopy access. Figure 2-16 represents the configuration of the

PPFC with regards to the microscope. The current design allowed monitoring the cell survival as well as the time-dependent morphological responses in the ECs. The PAECs were subjected to laminar steady flow (Re=990) with an average WSS of 11.48±0.98 dyne/cm^2 (the details of the flow field measurements were presented earlier) for up to 6 hours for preliminary testing of cell response to flow. In Figure 2-17, the morphological change (e.g., angle of orientation) of the cells at t=3, 6 hours are compared to the static condition. The PAECs in the static condition have a random orientation, as well as a cobblestone shape, whereas after 3 hours of exposure to the flow, the cells start to become elongated in the flow direction. A similar pattern is visible for the cells at t=6 hours, illustrating a temporal correlation between WSS and cell morphology. These findings are in good agreement with many other reported results [3, 10, 12, 16, 25, 30, 41].

Hence, the facility will allow future studies of the effects of various flow regimes (e.g., steady vs. pulsatile) on morphology and cytoskeleton structure (e.g., F-actin filaments re-localization). Cell exposure to flow for up to 10-12 hours is achievable in this facility. It has been reported that cytoskeletal remodeling pattern such as F-actin alignment with the flow occurs in a time-dependent manner [3, 30] .

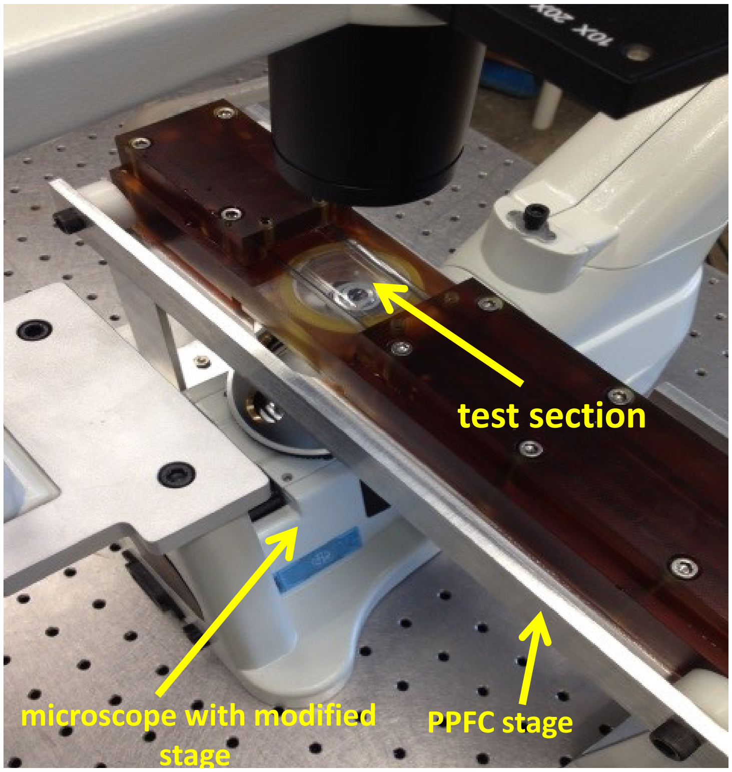

Figure 2-16 Configuration of PPFC for online microscopy set-up. The original microscope stage was modified to accommodate the PPFC structure.

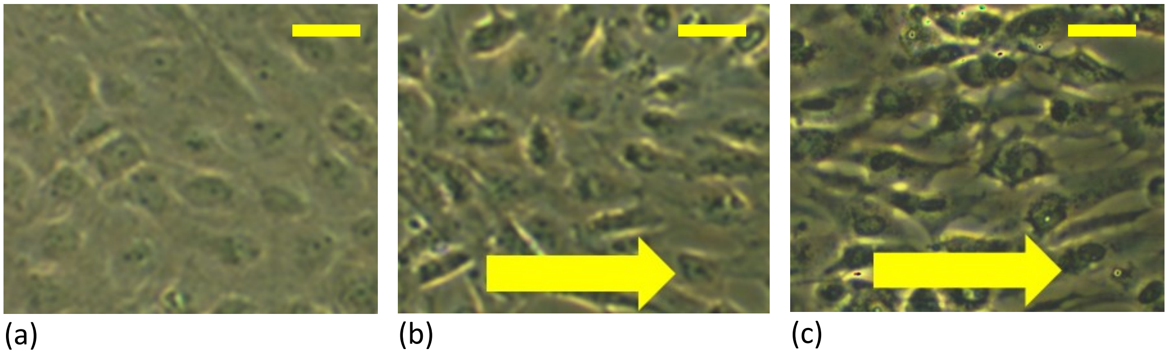

Figure 2-17 Light microscopy image of the PAECs (a) in static condition; (b) exposed to laminar WSS=11.48±0.98 dyne/cm^2 for t=3 hours; (c) exposed to laminar WSS=11.48±0.98 dyne/cm^2 t=6 hours (yellow arrows in (b) and (c) are representing the flow direction). Scale bar = 50 µm (see appendix 3 for low magnification images)

2.4 Discussion and Conclusions

The current hemodynamic facility was developed and designed with the following combined features. Firstly, it is a PPFC design concept made from ULTEM 1000 which is autoclavable, economic in terms of manufacturing, resistant to chemical corrosion and of reasonable strength (compared to other materials used in similar apparatus such as 316 SS), as well as a lighter weight. The channel is easy and quick to assemble/disassemble which is an essential feature of a biological apparatus. An adjustable height obstacle that can be in any desired shape (to mimic a more realistic occlusion structure) provides the opportunity to investigate both fluid dynamics and cell biology in this channel since it is well known that diseases such as atherosclerosis do not occur in random locations of arterial tree and, indeed, bends and bifurcations are the most commonly locations reported for plaque localization [3, 26].

All these features, along with real-time microscopy access (which can be connected to a camera for continuous visualization, imaging and post processing) and a glass window for optical access make this channel a valuable and novel research tool.

The LDV system allows a more precise quantification of flow uniformity and of whether the flow is fully developed at the test section, in contrast to most published works which have either quoted flow uniformity, by referring to theoretical equations [6, 12] or have not discussed fluid dynamic details at all [10, 41]. It has been shown here that the flow across the channel width (z direction) at the test section was uniform across about 65-75% of the coverslip area (for the two steady cases studied). For example, considering an average area of about 600 μm^2 for a rabbit aorta EC [12], this means that $2.5 \times 10^5 - 3.5 \times 10^5$ cells are exposed to a uniform shear stress (the cell count can be re-calculated for any other type of ECs) which statistically provides a sufficient cell count exposed to identical flow conditions and, consequently, the cells in the remaining 25-35 % of the coverslip (the sides of the coverslip) experience different magnitudes of WSS and so are not analyzed within the same statistical population as the cells at the center (this type of analysis has not been reported elsewhere).

For the flow to be fully developed (where the boundary layers on the top and bottom wall merge and no longer grow), no significant change in the velocity profiles along the channel (x direction) should be present. For a channel flow, the entrance length is defined as $L_e/H \approx 0.05\ Re_d$ for laminar flow [12], where L_e, is the entrance length, $Re_d = D_h U/\nu$ (with the hydraulic diameter $D_h = 2(W.H)/(W+H)$), and $L_e/H \approx 4.4\ Re_d^{1/6}$ for turbulent flow [23]. These theoretical relations are valid if the channel cross section is constant whereas, in most PPFC apparatus (including the current work), there is an entrance effect due to the transition from a circular to a rectangular cross section (to accommodate hose fittings). Hence, the entrance length associated with the flow may deviate from those empirical relations. In this work, to ensure the flow was fully developed, the streamwise velocities at locations D, E and F were experimentally measured for and it was shown that the corresponding profiles were similar, with no difference greater than 5%. These tests showed that the ECs are exposed to uniform WSS along the length and across the span of the channel.

Another contribution of this study was to examine the accuracy of the experimental flow field measurement results by comparison with theoretical relations. The WSS obtained from the experiments had higher values in almost all of the cases when compared to theoretical solutions (Equations 2-2 and 2-3) with the difference being greatest when the experimental WSS was compared to Equation 2-3 (error > 10 %). This suggests that Equation 2-2 should be used (if experimental investigation or numerical simulations are not feasible) to improve the accuracy, unless the PPFC aspect ratio is greater than 50 for which the difference between two theoretical values becomes less than 1% [26].

As a research apparatus, it is important the facility can produce various quantifiable types of flow profile. In this experiment, the uncertainties of the WSS measurements for the steady laminar and pulsatile flow regimes were quantified to be within ±13%. Based on the bias (systematic error) [47] of the current LDV system which was found to be about 2.5 mm/s, WSS as small as 0.3 dyne/cm^2 can be resolved which will be equivalent to a volume flow rate of 0.28 ml/s for the current pump system. The flow field measurement results in this work will be applied in future experiments to assess the effects of these well-quantified flows on PAEC morphology and cytoskeleton structure.

Morphological change (quantified by angle of orientation with flow, cell plan area (A_c), perimeter (P_c) and shape index S.I.=$(4\pi A_c)/(P_c^2)$) [12, 41]) and cytoskeleton remodeling have been widely accepted as an indicator of cell function [16, 18, 25]. Cells under static conditions have a cobblestone shape with a random angle of orientation [46], whereas cells exposed to uni-directional, moderate WSS, remodel in a pattern which is visible as elongation, alignment with flow direction and a reduction in S.I. This remodeling pattern also re-locates F-actin stress fibers so they are distributed more evenly and align in the direction of the flow compared to the central/peripheral distribution under static condition [11]. In the current paper which is concerned with the functionality of the facility for quantifying the cell response to mechanical stimuli, the time-dependent morphological change in PAECs (from a cobblestone shape under static conditions to an elongated shape, with gradual alignment with flow direction) is shown. Since the initial morphological cell response to flow is reported to occur at t=1-2 hours [30], experiments of 6 hrs duration provided a reasonable to test of the system functionality.

2.5 Summary

Due to the difficulties associated with conducting *in vivo* studies to investigate the effects of WSS on ECs, *in vitro* studies have been widely reported in this field. This chapter is about an *in vitro* hemodynamic facility based on the concept of PPFC with significant improvement compared to similar facilities. The development of this facility in order to mimic accurately-quantified physiological conditions and to facilitate monitoring the cell condition, during the experiments, is described in detail.

2.6 References

[1] D. P. Faxon, M. A. Creager, S. C. Smith, R. C. Pasternak, J. W. Olin, M. A. Bettmann, M. H. Criqui, R. V. Milani, P. J. Loscalzo, 2004, "Executive Summary: Atherosclerotic Vascular Disease Conference Proceeding for Healthcare Professionals from a Special Writing Group of the American Heart Association," Proc. *AHA Conference Proceedings*, New Orleans, 109, pp. 2595-2604, 2004.

[2] R. Ross, "The Pathogenesis of Atherosclerosis: A Perspective for the 1990s," *Nature* , 362, pp. 801 – 809, 1993.

[3] J.-J. Chiu and S. Chien, 2011, "Effects of Disturbed Flow on Vascular Endothelium; Pathophysiological Basis and Clinical Perspectives," *Physiol. Rev.,* vol. 91, pp. 327-387, 2011.

[4] T. D. Brown, 2000, "Techniques for Mechanical Stimulation of the Cells in vitro: A Review," *J. of Biomech Eng.,* 33(1), pp. 3-14, 2000.

[5] E. W. K. Young and C. A. Simmons, "Macro- and Mircoscale Fluid Systems for Endothelial Cell Biology," *Lab on a Chip,* 10, pp. 143-160, 2010.

[6] M. C. Laplaca and L. E. Thibault, "An in vitro Traumatic Injury Model to Examine the Response of Neurons to a Hydodynamically-Induced Deformation Loading," *Ann. Biomed. Eng.,* 25, pp. 655-677, 1997.

[7] A. Dardik, L. Chen, J. Frattini and F. Aziz, "Differential Effects of Orbital and Laminar Shear Stress on Endothelial Cells," *J. Vasc. Surg.,* 41(5) , pp. 869-880, 2005.

[8] M. A. Faracas, L. Rouleau, R. Fraser and R. L. Leask, "Development of 3-D, in vitro, Endothelial Culture Models for the Study of Coronary Artery Disease," *Biomed. Eng. Online,* 8, pp. 1-11, 2009.

[9] P. F. Davies, A. Remuzzitt, E. J. Gordon, C. F. Dewey and M. A. Gimbrone, "Turbulent Flow Shear Stress Induces Vascular Enothelial Cell Turn Over in Vitro," *Proc. the National Academy of Sciences of the United States of America,* 83, pp. 2114-2117, 1986.

[10] B. R. Blackman, K. A Barbee and L. E. Thibault, "In vitro Cell Shearing Device to Investigate the Dynamic Response of Cells in a Controlled Hydrodynamic Environment," *Ann. Biomed. Eng.,* 28(4), pp. 363-372, 2000.

[11] P. F. Davies, "Flow-Mediated Endothelial Mechanotransduction," *Physiol. Rev.,*

75(3), pp. 519-560, 1995.

[12] R. M. Nerem, M. J. Levesque and J. F. Cornhill, "Vascular Endothelial Morphology as an Indicator of the Pattern of Blood Flow," *J. Biomech. Eng.,* 103, pp. 172-176, 1981.

[13] P. A. Vander Laan, C. A. Reardon, G. S. Getz, "Site Specificity of Atherosclerosis," *Arterioscler Thromb Vasc Biol. ,* 24, pp. 12-22, 2004.

[14] F. Ghalichi , X. Deng , A. De Champlain , Y. Douville , M. King and R. Guidoin, "Low Reynolds Number Turbulence Modeling of Blood Flow in Arterial Stenoses," *Biorheology,* 34(4), pp. 281-94, 1998.

[15] G. A. Truskey, A. Pinero and K. Barber, "Effects of Recirculating Flow on U-938 Cell Adhesion to Human Vein Endothelial Cells," *Am. J. Physiol. Heart. Circ. Physiol.,* 275, pp. 591-599, 1998.

[16] P. F. Davies, C. Shi, N. Depaola, B. P. Helmek and D. C. Polacek, "Hemodynamics and the Focal Origin of the Atherosclerosis: A Spatial Approach to Endothelial Structure, Gener Expression, and Function," *Ann. N. Y. Acad. Sci.,* 947, pp. 7-16, 2001.

[17] W. Lidai, J. Xia, J. Yao, K. I. Maslov and L. V. Wang, "Ultrasonically Encoded Photoacoustic Flowgraphy in Biological Tissue," *Phys. Rev. Lett.* 111, pp. 204301-1-5, 2013.

[18] C.-Y. Chen, P. G. Menon, W. Kowalski and K. Pekkan, "Time resolved OCT-µPIV: A New Microscopic PIV Technique for Non-Invasive Depth Resolved Pulsatile Flow Profile Aquision," *Exp. Fluids.,* 54, pp. 1426-1435, 2013.

[19] R. Antony, G. Nandagopal, N. Sreekomar and N. Selvaraju, "Detection Principles and Development of Microfluidic Sensors in the Last Decade," *Microsyst. Technol.,* 20, pp. 1051-1061, 2014.

[20] S. Kefayati, J. S. Milner, D. W. Holdsworth DW3 and T. L. Poepping, "In vitro Shear Stress Measurements Using Particle Image Velocimetry in a Family of Carotid

Artery Models: Effect of Stenosis Severity, Plaque Eccentricity, and Ulceration," *PLoS ONE,* 9(7), pp. 0098209-1-12, 2014.

[21] G. M. Intelligence, "CES Edupack [computer program]," Cambridge University, Cambridge, UK. Available at http://www.grantadesign.com/products/ces (accessed 20 July 2014).

[22] T. R. Kucklick, Medical device R&D handbook, CRC press , Boca Raton, FL, ch. 2. ISBN: 978-0849327179, 2013.

[23] F. M. White, Fluid mechanics, McGraw Hill, New York, NY, ch. 6. ISBN: 978-1428849754, 2009.

[24] J. T. Dodge, B. G. Brown, E. L. Bolson and H. T. Dodge, 1992, "Lumen Diameter of Normal Human Coronary Arteries," *Circulation,* 86(1), pp. 232-246, 1992.

[25] S. Chien, "Mechanotransduction and Endothelial Cell Homeostasis; the Wisdom of the Cell," *Am. J. Physiol. Heart. Circ. Physiol.,* 292, pp. 1209-1224, 2007.

[26] G. A. Truskey, F. Yuan and D. F. Katz, Transport Phenomena in Biological Systems, Pearson press, New York, NY, ch. 3. ISBN: 9780131569881, 2009.

[27] H.J. Schnittler, R. P. Franke, U. Akbay, C. Mrowietz and D. Drenckhahn, "Improved in Vitro Rheological System for Studying the Effect of Fluid Shear Stress on Cultured Cells," *Am. J. Physiol.,* 265, pp. 289-98, 1993.

[28] W. H. Lee, "Biomedical Research Application of a Novel Double-Layer Parallel Plate Flow Chamber," M. Sc thesis, Virginia Polytecnique Institute and State University, Blacksburg, VA, 2007.

[29] L. Rouleau, J. Rossi and R. L. Leask, "Concentration and Time Effects of Dextran Exposure on Endothelial Cell Viability, Attachment, and Inflamatory Marker Expression in Vitro," *Ann. Biomed. Eng.,* 38(4), pp. 1451-1462, 2010.

[30] C. F. Dewey and S. R. Bussolari, "The Dynamic Response of Vascular Endothelial Cells to Fluid Shear Stress," *J. Biomech. Eng.,* 103, pp. 177-185, 1981.

[31] S. F. Kemeny, S. F. Dannielle and M. C. Alisa, "Hypo- and Hyperglycemia Impair Endothelial Cell Actin Alignment and Nitric Oxide Synthase Activation in Response to Shear Stress," *PLoS ONE,* 8(6), p. e66176, 2013.

[32] A. D. White and J. D. Rigden, "Localized Fluid Flow Measurements With an He-Ne Laser Spectrometer," *Phys. Rev. Lett.*, 4(10), pp. 176-189, 1964.

[33] J. W. Foreman, E. W. George and R. D. Lewis, "Measurement of Localized Flow Velocities in Gases with a Laser Doppler Flowmeter," *Phys. Rev. Lett.,* 7(4), pp. 77-87, 1965.

[34] TSI, "FlowSizer (2.0.4) [computer program]," Shoreview, MN, available at http://www.tsi.com/flowsizer-data-acquisition-analysis-software (accessed on 1 May 2011).

[35] F. Durst, R. Miller and J. Jovanovie, "Determination of the Measuring Position in Laser-Doppler Anemometry," *Exp. Fluids.,* 6, pp. 105- 110, 1998.

[36] F. Durst, J. Jovanovic and J. Sender, "LDA Measurements in the Near-Wall Region of a Turbulent Pipe Flow," *J. Fluid Mech.,* 295, pp. 305-335, 1995.

[37] F. Durst, J. Lekakis, J. Jovanovic and Q. Ye, "Wall Shear Stress Determination from Near-Wall Mean Velocity Data in Turbulent Pipe and Channel Flows," *Exp. Fluids.,* 20, pp. 417-428, 1996.

[38] S. B. Pope, Turbulent Flows, Cambridge, UK, Cambridge, ch. 7. ISBN: 9780521598866, 2000.

[39] W. C. Reynolds and A. K. F. M. Hussain, "The Mechanics of an Organized Wave in Turbulent Shear Flow; Part 3, Theoretical Models and Comparisons with Experiments," *J. Fluid Mech*., 54, pp. 263-268, 1972.

[40] S.-C. Wu, "Phase-Averaged Method Applied to Periodic Flow Between Shrouded Co-rotating disks," *Int. J. Rot. Machin.,* 8(6), pp. 413-421, 2002.

[41] C. F. Dewey, "Effects of Fluid Flow on Living Vascular Cells," *J. Biomech. Eng.,*

106, pp. 31-35, 1984.

[42] Q. Long, X. Y. Xu, K. V. Ramnarine and P. Hoskins, "Numerical Investigation of Physiologically Realistic Pulsatile Flow through Arterial Stenosis," *J. Biomech. Eng.,* 34, pp. 1229-1242, 2001.

[43] S. K. Samijo , R. Barkhuysen, J. Willigers , K. M. Leunissen , L. A. Ledoux, P. J. Kitslaar and A. P. Hoeks, "Wall Shear Stress Assessment in the Common Carotid Artery of End-Stage Renal Failure Patients," *Nephron,* 92, p. 557–563, 2002.

[44] J. N. Oshinski, J. L Curtin, F. Loth, "Mean-Average Wall Shear Stress Measurements in the Common Carotid Artery," *J. Cardiovasc. Magn. Reson. ,* 8, pp. 717-722, 2006.

[45] V. C. Patel and M. R. Head, "Some Observations on Skin Friction and Velocity Profiles in Fully Developed Pipe and Channel Flows," *J. Fluid Mech.,* 38, pp. 181-201, 1969.

[46] M. Dick, P. Jonak and R. L. Leask, "Stain Therapy Influences Endothelial Cell Morphology and F-actin Cytoskeleon Structure When Exposed to Static and Lamianr shear Stress Conditions," *Life Sci.,* 92, pp. 859-865, 2013.

[47] R. B. Abernethy, R. P. Benedict and R. B. Dowdell, "ASME Measurement Uncertainty," *J. Fluids Eng.,* 107, pp. 161-164, 1985.

[48] F. Vozzi, F. Bianchi, A. Ahluwalia and C. Domenici, "Hydrostatic Pressure and Shear Stress Affect Endothelin-1 and Nitric Oxide Release by Endothelial Cells in Bioreactors," J. *Biotechnol.,* 9, pp. 146-154, 2014.

Chapter 3

3 Wall Shear Stress for Laminar, Pulsatile and Low-Reynolds Number Turbulent Flows in a Parallel Plate Flow Chamber (PPFC) using Laser Doppler Velocimetry (LDV)

3.1 Introduction

The pathophysiological effects of hemodynamics on Endothelial Cells (ECs) have been the subject of study for over half a century [1-5]. Due to the difficulties associated with conducting *in vivo* experiments in this field, *in vitro* experiments have been widely carried out [5]. Among various types of apparatus to expose ECs to shear stress, the parallel plate flow chamber (PPFC) has been widely reported [3-4, 6]. Based on theoretical relations the wall shear stress (WSS, τ_w) in a rectangular channel for laminar flow (i.e., $Re= U_b (2\delta)/\nu <1350$, where U_b, δ and ν are the bulk velocity, channel half height and kinematic viscosity [7]) is defined as

$$\tau_w=6Q\mu/(WH^2) \tag{3-1}$$

where Q, μ, W and H are the volume flow rate of the flow, fluid dynamic viscosity, channel width and height, respectively. Although, this equation strictly applies to a channel flow with infinite aspect ratio ($W/H=\infty$), when $W/H>50$, τ_w is within ±1% of that obtained from this equation [8]. When $W/H>20$, more than 85% of the span of the channel is exposed to homogenous wall shear stress [9]. Application of Equation 3-1 has been reported in many research studies using PPFC [3-4, 6, 10]. It is widely accepted that ECs respond differently to various mechanical loading such as steady [3, 5], pulsatile [4, 6], turbulent flow [11] and disturbed flow [5]. Hence, it is critical to examine the effects of such flows on ECs rather than only steady laminar cases. Although it is reported that Equation 1 can be applied to estimate the average and maximum shear stress in a pulsatile flow [9], the accuracy of this estimation remains debatable. Geometrical and dynamical factors, such as the channel aspect ratio and flow frequency (f), respectively, influence the flow field, thus requiring more accurate methods for quantification of the WSS [8-9].

Analytical solutions, as well as numerical simulations, have been applied to solve for pulsatile pressure-driven flows through vessels. An analytical solution of a pulsatile flow in a channel can be obtained by considering the pulsatile gradient of the inlet pressure. The oscillating pressure gradient needs to be defined (e.g., as a Fourier representation) for each flow in order to proceed with the analytical solution [12]. Due to the complex geometry of arteries in locations such as at bifurcations (e.g., common carotid artery), as well as the narrowing of the artery associated with cardiovascular disease (e.g., Atherosclerosis), pulsatile blood flow regimes can become intermittently turbulent before re-laminarization, followed by an unsteady recirculation region [13-14]. No analytical solution is capable of solving such a flow regime. For the sake of simplicity, in a PPFC, an occlusion (narrowing) can be represented by an obstacle of selected shape (e.g., a step). Numerical methods have been applied to quantify the pulsatile WSS in a PPFC without an obstacle [15-17], as well as with an obstacle [18-20]. Different numerical methods and turbulent models have been developed for quantifying pulsatile flows that show transitional or turbulent characteristics [14, 21]. However, the results from those studies depict substantial discrepancies from reported detailed experimental studies [22] due to the limitations of the applied turbulent models as well as the boundary condition specifications [22]. Recently, more accurate numerical methods such as direct numerical simulation (DNS) have been shown to better predict the transition to turbulence in pulsatile flows [23]. However, since the results are highly sensitive to the inflow boundary conditions [19], such studies can benefit from the detailed statistics from experimental studies for specification of those boundary conditions. Experimental studies cover a wide spectrum of methods and techniques for the channel flow measurements. Owing to the confined size and geometry, invasive methods such as hot-film anemometry are not feasible. On the other hand, WSS measurement requires techniques that have an acceptable resolution for near wall velocity gradient measurements, as well as the capability of measuring the velocity fluctuations accurately in a pulsatile, transitional or turbulent flow. Velocity measurements in a pulsating flow are more challenging than for steady flow due to the necessity of a synchronization between the measuring instrument and the flow, as well as the need for a high frequency (f) response of the instrument in case of high frequency pulsatile flow [24]. A recent review shows that hot-wire anemometery (HWA), LDV, ultrasound Doppler velocimetry (UDV) and Particle image velocimetry (PIV) are the most reported techniques in pulsatile flow measurements [24]. Hot film anemometry (only applicable to non-liquid fluids) and UDV are not suitable techniques in a small-scale channel flow due to being intrusive and of poor spatial resolution [25], respectively. Whilst conventional PIV is not convenient for high frequency flows, time resolved-PIV (TR-PIV) may be used, although this method is more expensive than LDV. LDV has been reported in many studies for flow quantifications in a channel/tube flow due to its high frequency response as well as more accurate spatial resolution. There are numerous reported studies using LDV for conventional channel flow measurements (i.e., D_h>3 mm [26] where D_h, hydraulic diameter, is defined as $D_h=4A_t/p_t$ where A_t and p_t are the cross-sectional area and wetted perimeter of the test section). Most of the reported studies on wall-bounded flows using LDV have been carried out on vessels with larger sizes (e.g., H>60 mm for channel flows [27-28]). Very few studies were found in the literature where LDV was employed in a smaller size conventional channel (H<60 mm) which have been listed briefly in Table 3-1. These studies included steady laminar [29-31], pulsatile laminar [32] or turbulent flows [33-34]. The smallest and largest H among these studies was 7 mm [33] and 54 mm [32], respectively. The closest and furthest first measured point from the wall was reported to be 14 µm [32] and 700 µm [33], respectively. One of the major challenges that needs to be overcome for boundary layer measurement using LDV, is the method by which the wall location is determined with respect to the LDV measuring volume which becomes more critical with reduced H and the need for resolving closer points to the wall. Unfortunately, wall position determination methods remain under-reported in most studies. However, So *et al.* determined the wall location from the scattered light and then they confirmed it with the log-law of the wall (fitted to the measured mean velocity data) and found the uncertainty to be within ±50 µm [29]. In studies such as that reported by Castrejon *et al.* [32] where the first measured point is extremely close to the wall (14 µm), information regarding the experimental set-up required to resolve this high spatial resolution seems to be critical. Those studies that utilized both LDV and PIV reported that the LDV had higher spatial resolution than PIV (i.e., 14 µm vs. 55 µm and 200 µm vs. 1 mm, for the studies reported by Castrejon *et al.* [32] and Marx *et al.* [34], respectively).

LDV has been used for flow measurements in very few mini-channels (200 μm<D_h<3 mm). As an example, Arbeiter *et al.* [35] studied the evolution of the flow field in the entrance region of a rectangular mini-channel with H=1 mm (D_h=1.92 mm), along the channel centre-line, using an LDV system with measurement volume diameter of 39 μm. They used a traversing system with an uncertainty of 10 μm, although streamwise velocities across the channel height (boundary layer) were not measured.

The review of the literature discussed above (to the best of the authors' knowledge) shows that the smallest channel flow measurement using LDV has been carried out in channels at least four times larger than the conventional channel threshold ($D_h \geq 3$ mm). Although the hydraulic diameter is used as a scaling parameter to differentiate between different types of channels, for streamwise velocity measurements, it is H that plays the key role. The confined geometry of a channel along with the effects of the walls (e.g., on light scatter) and the limitations associated with the LDV measuring volume size and beam half-angle, have made these measurements challenging, particularly for boundary layer measurements.

Table 3-1 A brief relevant literature review on channel flow (H<60 mm) measurements by LDV

Reference	Main dimension (mm)	D_h (mm)	Flow regime	Re	Closest measured point to the wall (μm)
Castrejon *et al.* [32]	H=54	69	pulsatile laminar (f=68.5 and 114.5)	-	14
Appel *et al.* [33]	H=7	14	turbulent	17,800-30,100	250-650
Marx *et al.* [34]	H=20	32	turbulent	130,600	200
So *et al.* [29]	H=40	73	laminar and turbulent	1350, 4100, 8200	500
Verhelst *et al.* [30]	W=20	35	laminar	0.23	50
Zhang *et al* [31]	H=20	33	laminar	7200, 17,400	-

The current paper reports on the use of LDV to experimentally quantify the WSS by measuring the velocities in laminar, pulsatile and low-Re turbulent flow regimes in a small-scale conventional channel. The methods and challenges associated with measuring velocity components in such a confined region are discussed, through examination of the experimental results. Some results and their discussion will also be presented. The experimental set-up and analysis procedure will also be applied for further studies of pulsatile channel flows in the vicinity of an obstacle to mimic atherosclerosis.

3.2 Experimental Setup

In this section, the flow facility, instruments and measuring techniques, selection of seeding particles, wall location determination method and experimental conditions will be discussed.

3.2.1 Closed-loop Flow Facility

A PPFC was designed and developed for this study to mimic a wide variety of flow regimes and shear stresses. The channel is mainly manufactured from ULTEM 1000 resin (except the glass test section for optical access) and consists of top and bottom cavities with the coverslip test section positioned on the bottom cavity and upstream and downstream flow development transition lengths of 251 mm (chosen based on theoretical calculations [36] to ensure fully developed flow at the test section) and 94 mm, respectively. The channel test section has a length L=22 mm with rectangular cross section (height, H=1.8 mm and width, W=17.5 mm) giving a hydraulic diameter (D_h) of 3.26 mm. There is a smooth transition from a circular (I.D 3.18 mm) to a rectangular cross section and *vice versa*, upstream and downstream of the channel, respectively, from/to the hose installation. The test working section is made from precision glass (Angstrom Precision Optics Inc., USA) for optical access on the top cavity and there is a shallow square insert 22 × 22 mm in the bottom cavity for installation of 0.22 mm thick coverslips to be flush-mounted with the lower wall of the channel.

The flow was driven by a positive displacement pump (CompuFlow 1000 MR, Shelley Medical Imaging Technology, Canada), capable of producing steady flows (volume flow rate Q=0.1-50 ml/s), realistic physiological flows (e.g., carotid), and user defined waveforms (e.g., non-zero mean sinusoidal waveforms). The flow loop also included a reservoir and a controlled heating unit to maintain the fluid temperature at 37 ºC, since the primary goal of the current study was to quantify the flow conditions for biological experiments.

A biological fluid, composed of Dulbecco's Modified Eagle Medium (DMEM), HEPES, NaOH pellets and antibiotics was prepared in-house for each experiment. The viscosity was measured using an Ubbelohde viscometer in a 37 ºC water-bath and was found to be 0.737±0.0012 mPa.s which is in the range of similar solutions used in other studies [4, 37]. The fluid density was measured to be 997.96±0.12 kg/m^3 (see Chapter 2 for detailed information).

3.2.2 Instruments and Measurement Techniques

3.2.2.1 LDV System

An LDV system (with a customized setup) was developed and applied in this study. The system consisted of a 5 Watt water-cooled Argon-ion laser (COHERENT, USA), a 2-component (4 beams) mini-probe (TRx20, TSI, USA) with measuring control volume size of 68 μm × 64 μm × 1.1 mm (horizontal axis, vertical axis, length), a photo detector multiplier (PDM 1000, TSI, USA), a FSA 3500 signal processor (TSI, USA) and FlowSizer software (version 2.0.4) [38]. Two pairs of shifted and unshifted beams (green and blue with wavelengths λ=514.5 and 488.0 nm, respectively) were used to measure the u- and v- velocity components. The mini-probe, with its focal length of f_L=110 mm and beam spacing of 15 mm, was an appropriate tool for the confined geometry of the PPFC working section. A Bragg cell was used to shift the frequency of each colour by 40 MHz to eliminate directional ambiguity. The probe was mounted on a multi-axis traverse (THORLABS, USA) with positional accuracy of ±5 μm (in all three directions) to ensure accurate translation in all three directions. Typical LDV data rates were 50-100 Hz near the wall and 500-2000 Hz (depending on the distance from the wall and flow velocity) further from the wall. All the acquired data were analyzed with MATLAB (Total Academic Headcount license, 2013a). A schematic of the LDV layout, as well as a photograph representing the mini-probe setup with regards to the PPFC, are depicted in Figure 3-1.

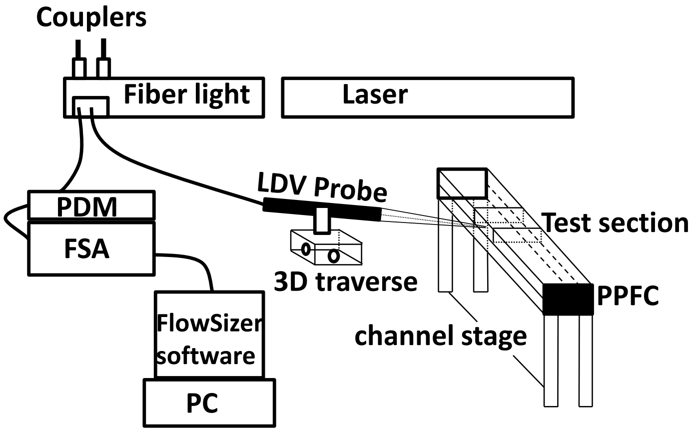

(A)

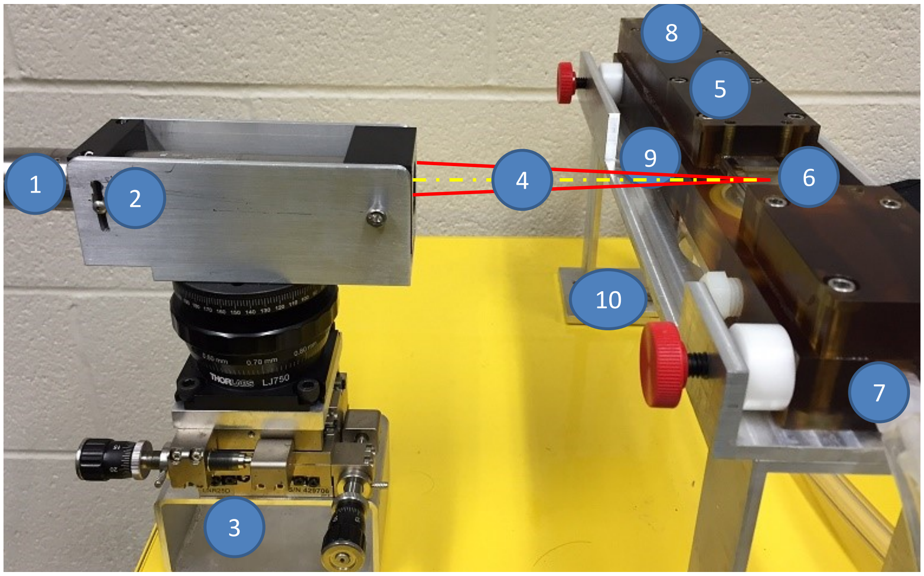

(B)

Figure 3-1 Layout of the LDV system components and probe positioning with respect to the PPFC test section (A); mini-LDV probe setup with respect to the PPFC, 1: mini-LDV probe, 2: custom-designed probe holder capable of tilting, 3: traversing system, 4: laser beam pathways from the probe, 5: PPFC top cavity, 6: PPFC working glass section, 7: PPFC outlet, 8: PPFC inlet, 9: PPFC bottom cavity, 10: PPFC stage (B)

3.2.2.2 Seeding Particles

Choosing seeding particles is a compromise between a sufficient tracer response (requiring smaller particles) and a high signal-to-noise ratio (SNR) of the scattered light signal (requiring larger particles) [39]. Stoke's drag law applies when the particles Reynolds number Re_p is smaller than one. Re_p is defined as [39]

$$Re_p=\rho_f V d_p/\mu \qquad (3\text{-}2)$$

where ρ_f, V, d_p and μ are the fluid density, fluid velocity, particle diameter and fluid viscosity, respectively. In the case of Stoke's flow, a particle's response time τ_p is defined as

$$\tau_p=d_p^2\rho_p/18\mu \qquad (3\text{-}3)$$

where ρ_p is the particle density. According to Loth [40], the degree to which the particle may be considered to be in kinetic equilibrium with the surrounding fluid is given by the (integral-scale) Stoke's number (St_Λ) which is defined as the particle's response time (τ_p) to the local continuous-fluid turbulent integral time scale (τ_Λ)

$$St_\Lambda = \tau_p/\tau_\Lambda \qquad (3\text{-}4)$$

where τ_Λ can be determined by [41]

$$\tau_\Lambda=\Lambda/u_{rms} \qquad (3\text{-}5)$$

where Λ and u_{rms} are the integral length scale and typical turbulence intensity in the fluid, respectively. According to Keirsbulk *et al.* [42] the integral length scale for an order of magnitude analysis relevant to the current study is about 0.92δ, where δ is the channel half height.

For an unsteady pulsatile flow, St_o is defined as

$$St_o=\sqrt{(\omega\, d_p^2/2\nu)} \qquad (3\text{-}6)$$

where $\omega=2\pi f$ and ν are the angular frequency of the flow and kinematic viscosity of the fluid, respectively [43]. If St_Λ or St_o <<1, the particle acts as a tracer. Melling suggests that for good frequency response (10 kHz), d_p should not exceed 1 μm [39]. In the current study, Titanium dioxide particles (Showa America, USA), with size distribution ranging from 0.24-0.47 μm (average of ≈ 0.36 μm) and ρ_p=4.0 gr/cm^3, were used for seeding. Taking V=1.5 m/s (maximum velocity measured), Re_p=0.53 so that from Melling [39], Stoke's drag law is applicable. From Equation 3-3 the particle response time $\tau_p = 3.9\times10^{-8}$ s. Taking a typical value of u_{rms}=0.21 m/s (from the measured data in this study), Equation 3-5 gives $\tau_\Lambda=3.9\times10^{-3}$ such that from Equation 3-4, $St_\Lambda = 10^{-5}$ which is <<1. Taking ω=6.3 rad/s for the pulsatile flows studied here, $St_o=7.4\times10^{-4}$ which is also <<1. These results imply that the particle may be assumed to have the same velocity as the fluid and, hence, it can follow the fluid motion at integral scale with negligible lag.

3.2.2.3 Wall Location Determination Method for LDV Measurements

Determination of the absolute distance of the LDV measuring volume from the wall plays a significant role in accurate quantification of WSS, particularly in the case of a confined geometry. Various methods have been discussed in the literature. Durst *et al.* found that a hot-wire anemometer output voltage increases if the distance from the centre of the wire to the wall is less than 800 μm. Then, they traversed the LDV measuring volume toward the wall across the wire and a voltage change in the LDV photomultiplier voltage was detected due to the Gaussian intensity variation of the light scattered by the wire. The location of the maximum voltage output of the LDV was assigned as being the centre of the measuring volume which was identical to the location of the centre of the wire and, hence, knowing the distance of the wire from the wall, the location of the LDV measuring volume was known [44]. It has also been reported that there is a distinct frequency shift when the LDV beam is traversed into the wall [35-37]. Radomsky *et al.* determined the wall location by tilting the LDV probe by half of the beam angle and using two techniques: (1) lowering the laser power and visually observing the beam crossing just at the wall and (2) monitoring the output from the photomultiplier using an oscilloscope. They reported that both methods were able to determine the location of the wall to within ± 20 μm [45] (a more detailed literature review on this topic is discussed in Appendix 1).

To determine the wall location in the present study, at the start of each experiment, the channel was cleaned to remove any possible particle deposition on the wall. The LDV probe was tilted by $\varphi=4.5^{o}$ (slightly greater than the beam half angle $\theta=3.9^{o}$) to allow for near wall measurements without the beams encountering the lower channel wall, as well as to reduce the interception of reflected light from the wall. After lowering the laser power (e.g., to 50-100 mW), the measuring volume was traversed downward until visually ensuring that the beam crossing was fully inside the wall. The voltage output of the PDM was monitored with an oscilloscope and the measuring location was traversed upward in small increments until an initial voltage change was observed. The more the beam crossing was traversed into the wall, the higher the voltage change recorded. This was followed by a descending pattern until the voltage change diminished to lower values and stayed approximately constant over another short upward traverse increment indicating that the measuring volume was completely within the fluid yet not far enough from the wall for many particles to pass through the volume ($\approx 0<y<40$ μm). The location of the maximum voltage monitored was assigned as being the location of the centre of the measurement volume. This voltage change was due to the intensity variation of the light scattered from the solid-fluid surface (i.e, PPFC lower cavity wall/fluid). Since the intensity variation was proportional to the beam crossing waist (w_s) and the penetration depth of the measuring volume (d_s), the maximum occurred at the centre of the measurement volume. A schematic of this procedure is illustrated in Figure 3-2. The positional uncertainty from this method was determined to be within ±27 μm, as determined by a second-order polynomial regression on the streamwise velocity profile across the channel height for laminar flows to find the distance from the peak (centre-line velocity) to the wall and comparing the results with those from the method described. Note that, according to Durst *et al.*, limiting the measurements to distances larger than half the measurement volume diameter reduces the measurement noise significantly [44].

3.2.3 Experimental Conditions

Flow quantifications for a laminar, two laminar pulsatile (carotid waveform and non-zero-mean sinusoidal) and a low-Re flow cases were carried out. The inlet condition for the flow loop was adjusted by the volume flow rate of the pump (Q, ml/s). Section 3-3-1 discusses all of the details concerning the measurements for each case and the results obtained.

Although tilting the angle of the probe did not affect the u component measurements, the v component measurements were in error by approximately 0.3% and were corrected by trigonometry. The beam crossing was adequate over the entire test section and the measuring volume position (due to the change in f_L in any LDV measurements where the laser beam traveled in more than one medium) was corrected by applying Snell's Law. A detailed discussion about ray analysis within the PPFC glass working section is provided in Appendix 2.

To assess whether fully developed, uniform flow conditions existed in the test section, vertical and lateral profiles of the time-averaged streamwise velocity (U) component were measured at three different streamwise locations in the test section. Figure 3-3 illustrates the schematic of the glass working section along with the reference coordinate system and measurement locations. Vertical streamwise velocity measurements were taken at $x/L=0$, 0.5 and 1, $2z/W=0$ and $0<y<900$ µm ($0<2y/H<1$). Similarly, lateral streamwise velocity measurements were taken at $x/L=0$, 0.5 and 1, $-1<2z/W<1$ and $y=300$ µm ($2y/H=1/3$).

The Re for a channel flow is defined as $Re=U_b(2\delta)/\nu$ or $Re_0=U_0\delta/\nu$, where U_b, U_0, δ and ν are the channel bulk velocity (defined as the volume flow rate divided by the channel test section cross-sectional area), centre-line velocity (maximum velocity), channel half height ($\delta=H/2$) and kinematic viscosity of the fluid, respectively [7]. The flow is reported to be laminar for $Re<1350$ and turbulent for $Re>1800$ [7]; although transitional effects are evident up to $Re=3000$ [46].

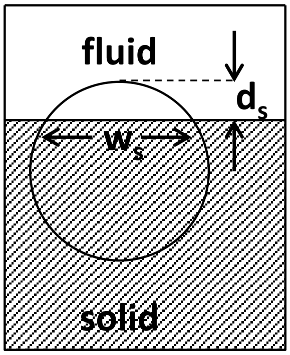

Figure 3-2 A schematic of the measuring volume location penetration at the solid-fluid intersection (d_s and w_s are the distance from the top of measuring volume to the fluid-solid baseline and beam measuring volume waist intersection with the baseline, respectively)

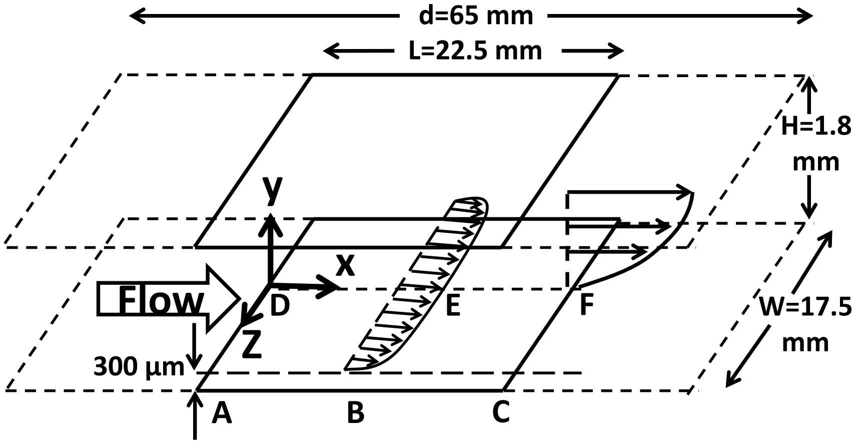

Figure 3-3 Reference coordinate system, working section dimensions and measurement location for spanwise u-velocity at x/L=0, 0.5 and 1, 2y/H=0.33 (A, B and C) and measurement location for streamwise u-velocity x/L=0, 0.5 and 1, z/W=0 (D, E and F).

3.3 Results and Discussion

3.3.1 Uncertainty Analysis

Any experiment suffers from some level of uncertainty which may arise from systematic error (B, bias) and imprecision (S, random errors) [47]. The experimental error can be quantified by

$$\boldsymbol{\varepsilon}_{\mathbf{total}} = \sqrt{\mathbf{B}_{\mathbf{total}}^{2} + \mathbf{P}_{\mathbf{total}}^{2}}$$

$$\mathbf{B}_{\mathbf{total}} = \left[\sum_{\mathbf{i=1}}^{\mathbf{k}} \mathbf{B}_{\mathbf{i}}^{2}\right]^{\mathbf{1/2}} \tag{3-7}$$

$$\mathbf{P}_{\mathbf{total}} = \mathbf{t}_{\mathbf{s}} * \mathbf{S}_{\mathbf{total}}$$

$$\mathbf{S}_{\mathbf{total}} = \left[\sum_{\mathbf{i=1}}^{\mathbf{l}} \mathbf{S}_{\mathbf{i}}^{2}\right]^{\mathbf{1/2}}$$

where ε_{total}, B_{total}, P_{total} and S_{total} denote the total experimental uncertainty, bias errors, random errors and the standard deviation of the random errors, respectively. For an experiment with large sample size (N>30), t_s=1.96 for a 95% confidence level [47].

The LDV measurements are subject to numerous errors. Bias errors are mainly due to the laser beam geometry [48], electronic noise (e.g., signal, frequency-shifting units) [49] and seeding bias errors. Durst *et al.* suggests minimizing the electronic noise by reducing the frequency shift to 200 kHz in the wall region measurements, as was done in the present work. The particle bias is negligible upon proper seeding particle selection (as discussed earlier in section 3.2.2.2). The sources of the statistical bias are mainly velocity, angle and gradient bias. The velocity bias occurs because the particle flux entering the measuring volume depends on the particle spatial distribution and velocity [50]. A transit-time weighting technique was applied to correct this bias [51]. Angle bias can be corrected by applying a frequency shift [48]. Gradient bias is due to the finite size of the measuring volume that can contain particles with different velocities. After the applied corrections these errors are negligible compared to the random errors.

To quantify the imprecision of LDV, various laminar flow velocities at different distances from the wall were measured and, by reducing the flow rate, the root-mean-square (rms) value for the measured velocities did not decrease to less than 0.0025 m/s (2.5 mm/s) and, hence, and any rms velocity less than this was considered insignificant. By increasing the flow rate, typical rms velocities divided by the local mean velocities of 2% and 6-7% were detected at locations away from and close to the wall, respectively (as the velocity increases the fixed bias of 0.0025 m/s becomes less significant). In a similar near wall velocity measurements using LDV by Kehoe, this fixed rms velocity was found to be 0.02 m/s [52]. This bias error was due to a stochastic sampling error resulting from the LDV electronics. The higher error in the wall region was a result of the light scattered from the wall surface in the confined geometry of the current PPFC as well as reduced time-averaged mean velocity (and, hence, a larger ratio between the fixed bias value and mean velocity at the wall region).

The statistical sampling error refers to the statistical uncertainty of the acquired data. According to Kunz *et al.* [48], the random error associated with the first (mean velocity) and second moments (turbulece intensity) of velocity can be estimated using

$$\frac{\varepsilon_U}{U} = \frac{1}{\sqrt{N}}\frac{u_{rms}}{U} \tag{3-8}$$

$$\frac{\varepsilon_{u_{rms}}}{u_{rms}} = \frac{1}{\sqrt{2N}} \tag{3-9}$$

The typical total uncertainties (ε_{total}) associated with the data acquired the near wall (2y/H ≈0.27) for N=2000 are summarized in Table 3-2.

WSS (τ_w) was calculate as

$$\tau_w = \mu\frac{\partial U}{\partial y}|_{y=0} \tag{3-10}$$

Table 3-2 Typical uncertainties of flow statistics for near wall data (2y/H=0.27)

Velocity component	Absolute uncertainty	Reference value	% uncertainty
$\boldsymbol{U}$ (m/s)	0.070	1	7.0
$\boldsymbol{V}$ (m/s)	0.081	1	8.1
$\boldsymbol{u_{rms}}$ (m/s)	0.017	0.22	10.37
$\boldsymbol{v_{rms}}$ (m/s)	0.003	0.03	11.87
$\overline{\boldsymbol{u'v'}}$ (m^2/s^2)	0.0004	0.0025	15.76

The total uncertainty of the distance from the wall ($\boldsymbol{\varepsilon_y}$) arising from the wall location determination method, the traversing system and the manufacturing tolerance of the precision glass canopy was found to be ±30 μm. The uncertainty in the of experimentally measured WSS was estimated from

$$\boldsymbol{\varepsilon_{\tau_w}} = \left(\sum_{i=1}^{n} \left[\varepsilon_{x_i} \frac{\partial \tau_w}{\partial x_i} \right]^2 \right)^{1/2} \tag{3-11}$$

where $\boldsymbol{\varepsilon_{\tau_w}}$, $\boldsymbol{\varepsilon_{x_i}}$ and $\frac{\partial \tau_w}{\partial x_i}$ are the total uncertainty associated with τ_w, uncertainties of the independent variables involved in calculation of τ_w and the partial derivative of τ_w with respect to these variables. The maximum uncertainty associated with τ_w (determined from the time-averaged mean velocity gradient) was found to be ±15.4%.

3.3.2 Curve Fitting and Shear Rate Approximation

WSS measurements through shear rate ($\dot{\gamma} = \frac{\partial U}{\partial y}$) determination using LDV have been reported in previous work [54-56]. Various-degree polynomial interpolation (regression) methods can be used on the measured velocity points close to the wall, such as a polynomial power series of the form

$$U(y)=a_0+a_1y+a_2y^2+a_3y^3+\ldots+a_ny^{(np)} \tag{3-12}$$

where np is the degree of the polynomial [57]. If N_p, the number of the points used in the power series is larger than np+1, the approximation becomes a least square regression of the np-th degree. For WSS estimation, polynomial degrees np=3 and higher are less robust since the results are more sensitive to the random errors distributed in the data [58]. Lou *et al.* have investigated the error associated with the linear and quadratic curve-fitting of measured velocity profiles and showed that a quadratic fit has less error than a linear regression [58]. According to their study, for a steady, fully developed flow in a straight vessel, the error of the quadratic fit is almost zero (considering no uncertainty in the data) since the flow velocity profile is parabolic. However, for an oscillating flow, a quadratic curve fitting method may be subject to some errors. Using the zero-velocity (no-slip) condition at the wall and two measured velocity points with distances from the wall of y_1 and y_2 and a boundary layer thickness of δ_b, the error of the fitted curve is a function of y_1/δ_b and y_2/y_1 where δ_b can be approximated by r/α [57] (r and α are the vessel radius and Womersley number, respectively; the latter will be defined in detail in section 3.5.1), such that the error increases by increasing both y_1/δ_b and y_2/y_1. As an example, taking the first measurement point at 80 μm from the wall and the channel half height as r for the current study, $y_1/\delta_b \approx 0.13$. Considering $y_2/y_1=2$, the error of the quadratic curve-fit is <5%. The two measured points along, with the no-slip condition, suffice for a quadratic fit. However, Lou *et al.* [58] did not consider the errors and uncertainties associated with the wall effects on the measurements themselves which significantly increase closer to the wall. In another study, Fatemi *et al.* [57] reported that the error of the curve fitting method is correlated with y_1, np and N_p. In the present work, a similar approach to that suggested by Fatemi *et al.* [57] was used to assess the error associated with the regression technique. For a steady laminar flow (Re=990), a 2nd order polynomial fit (np=2) was chosen and the regression error with N_p =3, 4, 5 and 6 were investigated for various y_1=40, 80, 120, 160 and 200 μm (i.e., 2y/H=0.04, 0.09, 0.13, 0.18 and 0.22). In each case the shear rate ($\dot{\gamma}$) determined by the regression method was compared with the analytical $\dot{\gamma}$ value calculated by Equation 3-13 and the error was defined as $|((\dot{\gamma}_{regression\,method} - \dot{\gamma}_{analytical})/\dot{\gamma}_{analytical}) \times 100|$. Figure 3-4 represents the results for this analysis. At $2y_1/H=0.09$, the trends in the error bars are consistently smaller for most of the cases with different N_p. Among the regression curves with a different number of points, $N_p=5$ has the least error overall which is equal to about ±9.1% at $2y_1/H=0.09$, being within the uncertainty range of the experiments. Consistent results were obtained with different measurement sets and, hence, a 2nd order regression method with $2y_1/H=0.09$ and $N_p=5$ was applied for WSS estimations from the velocity profiles.

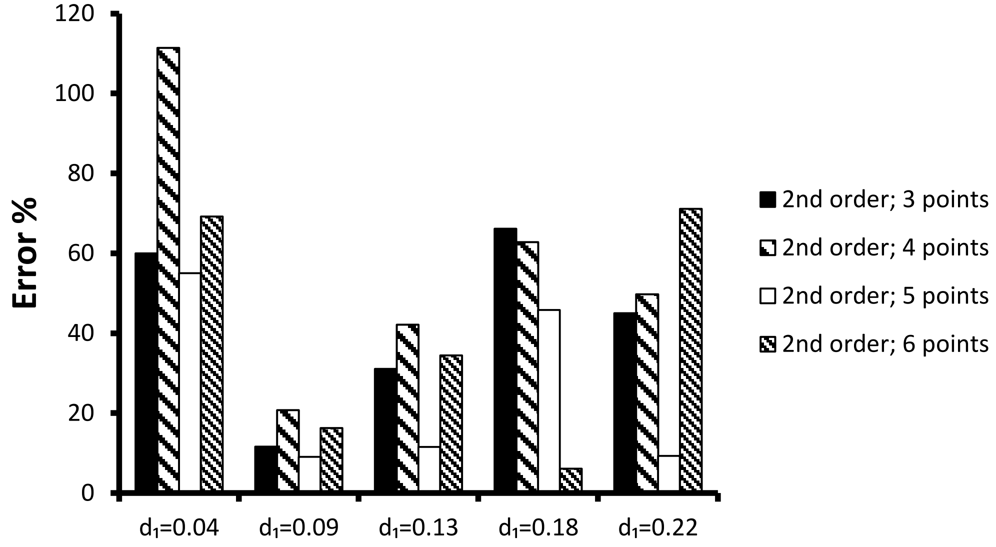

Figure 3-4 Percent shear rate (defined as $\dot{\gamma} = {dU}/{dy}$) error for a 2nd order polynomial fit (np=2) using $N_p=3$, 4, 5 and 6 points for various initial point $d_1=0.04$, 0.09, 0.13, 0.18 and 0.22 ($d_1=2y/H$)

3.3.3 Symmetric Streamwise Velocity Profiles across the Channel Height (H)

In order to demonstrate the symmetric velocity profiles across the channel height ($0<2y/H<2$), the velocity measurements were taken without tilting the LDV probe for a laminar flow with Q=12.8 ml/s (Re=990) where the results are shown in Figure 3-5. For these measurements, the velocity data were obtained by traversing the probe from the lower wall upward up to the channel top wall. After acquiring the data, the location of the measuring volume from the wall was estimated by setting the distance from the profile peak (U_{max}) to the walls to be equal to channel half height since it is known to occur at the channel centre-line [36]. Velocity measurements without tilting the LDV probe resulted in a wall offset of $2y/H\approx0.2$ ($y\approx200$ μm) whereas measurements taken with the probe being tilted can resolve the velocity as close as $2y/H\approx0.04$. Since the results show symmetric profiles with respect to the channel centre-line, all of the measurements were taken at 0<2y/H<1.

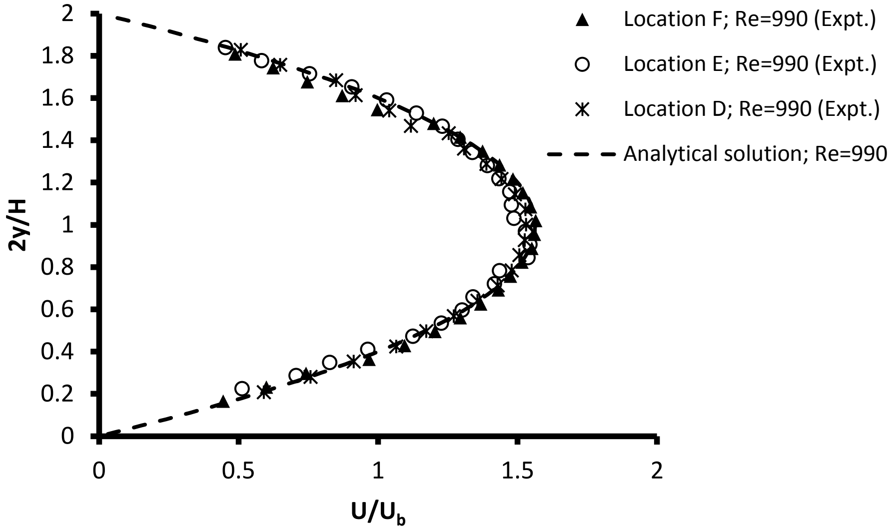

Figure 3-5 Streamwise time-averaged mean velocity U normalized by U_b (bulk velocity) with the analytical solution from Equation 3-13 for 0<2y/H<2 at locations D, E and F for the laminar flow with Re=990 to demonstrate a parabolic and symmetric (with respect to the channel centre-line) profile across the channel height

3.3.4 Steady Laminar Flow

A laminar flow with Q=12.8 ml/s (Re=990) was quantified in the test section. To monitor the uniformity of the flow across the span of the channel, Figure 3-6 illustrates the normalized time-averaged streamwise velocity U measured at locations A, B and C compared with the analytical solution from [8]

$$U(y,z) = \frac{\Delta P H^2}{8\mu L}\left(1 - \frac{4y^2}{H^2}\right) - \frac{4\Delta P H^2}{\mu L}\sum_{n=0}^{\infty}\frac{(-1)^n cosh\left(\frac{(2n+1)\pi z}{H}\right) cos(\frac{(2n+1)\pi y}{H})}{(2n+1)^3\pi^3 cosh(\frac{(2n+1)\pi W}{2H})} \qquad (3\text{-}13)$$

where U(y,z), ΔP, μ and L are the streamwise velocity at any specified y and z coordinate, the pressure loss along (x) the channel, dynamic viscosity and channel length, respectively. The results show that about 65-75% of the test section is exposed to a uniform flow.

The normalized time-averaged streamwise velocity U profiles at A, B and C vs. the analytical solution are plotted in Figure 3-7. The average experimental (using the velocity gradient method) and analytical τ_w (derived from Equation 3-13) were found to be 11.48±0.98 dyne/cm^2 and 10.45±0.37 dyne/cm^2 (≈9% difference), respectively, with this difference being within experimental errors.

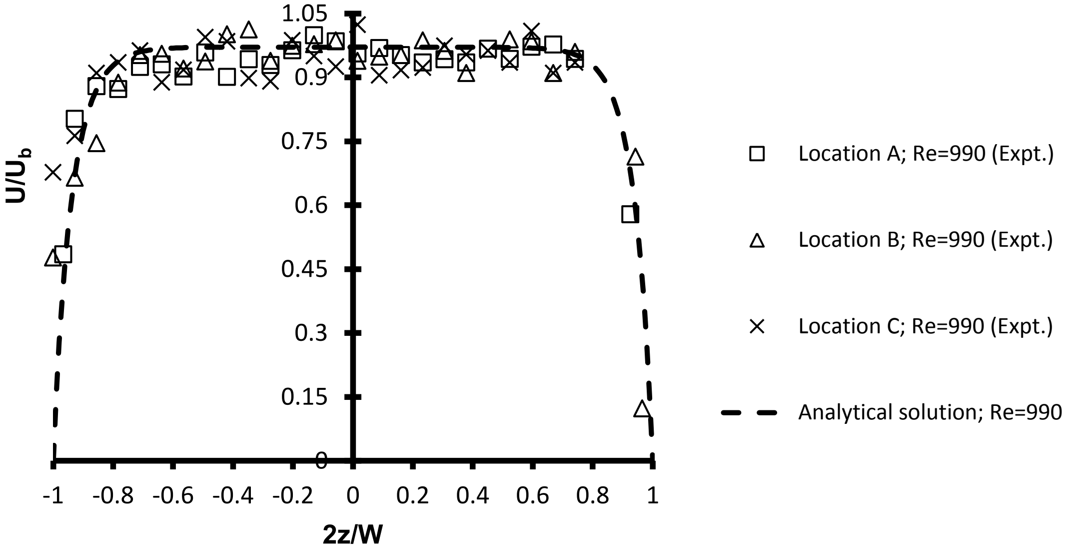

Figure 3-6 Comparison of streamwise direction time-averaged mean velocity U normalized by U$_b$ across the span of the channel with the analytical solution from Equation 3-13 for -1<2z/W<1 at locations A, B and C for Re=990. The average deviation of the experimental data points from the analytical solution at locations A, B and C are ±2.4, ±2.9 and ±4.4%.

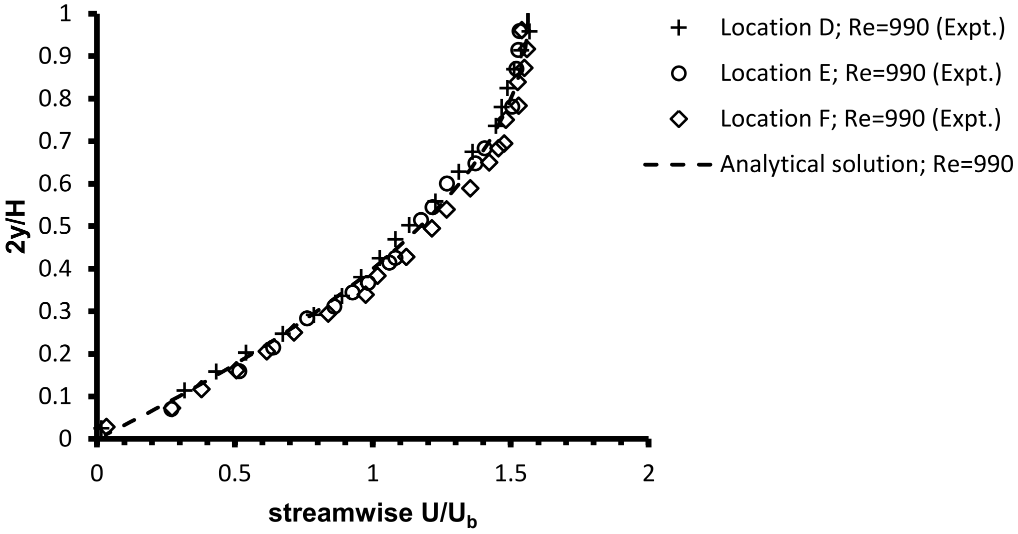

Figure 3-7 Comparison of streamwise time-averaged mean velocity U normalized by U_b (bulk velocity) with the analytical solution from Equation 3-13 for 0<2y/H<1 at locations D, E and F for Re=990. The average deviation of the experimental data points from the analytical solution at locations D, E and F are ±1.8, ±3.2 and ±6.2%.

3.3.5 Pulsatile Flows

For a flow with imposed fluctuations, the instantaneous velocity u(t) can be Reynolds-decomposed [59] as

$$u = U + \tilde{u} + u'; \qquad < u >= U + \tilde{u} \tag{3-14}$$

where u, U, $\tilde{\boldsymbol{u}}$, $\boldsymbol{u}'$and <u> are the u-component instantaneous velocity, the global time-averaged mean velocity, the periodic bin-average velocity, the turbulent fluctuations of the velocity and phase-averaged velocity, respectively. Since the flow was laminar, the $\boldsymbol{u}'$ term was zero [60].

A synchronization encoder pulse from the pump marked the beginning of each cycle. The time series data were then phase-averaged using Equation 3-14. The bin size was determined based on the minimum number of LDV samples (i.e., 50 [47]) required to ensure statistical accuracy. For each measurement location, 200 waveform cycles [61-62] of period (T) of 920 ms were averaged within 23 bins per cycle. Since the WSS calculations were dependent on the velocity data in the wall region (2y/H<0.22) and considering the lower LDV data rate ($\dot{N}$) in the wall region (the data were not evenly sampled), it was found that a bin width of 38-40 ms guaranteed a minimum number of 50 LDV samples in each bin. Due to higher $\dot{N}$ (typical 150-300 Hz) at 2y/H>0.22, the number of LDV samples per bin was much higher (>1000).

To ensure that the pulsatile flow was laminar, examining the spurious rms velocities within each bin for various phase-averaged data with different bin size showed that these values were within the experimental uncertainty.

3.3.5.1 Carotid Pulse

A carotid pulse with f≈1.1 Hz (pulse period=920 ms) was produced by the pump. The Local minimum and maximum Reynolds numbers were $Re_{0\text{-}min}\approx 100$, $Re_{0\text{-}max}\approx 560$ and $Re_{0\text{-}mean}\approx 282$. According to a recent study by Filatova *et al.* [63], Re_{mean} in the internal carotid artery (ICA) ranges between 227±150 and 613±134 depending on age, sex. The Womersley number (α) which is the ratio between the inertial forces with respect to the viscous forces is defined as $\alpha=\delta(\omega/\nu)^{0.5}$ [64] which returns $\alpha=2.76$ for the current case (according to Campbell *et al.* [65] α ranges between 3.3 and 4.69 in the ICA). The normalized phase-averaged streamwise velocity time history $<u>^*$ at 2y/H=1 for location D is illustrated vs. the normalized bulk velocity in Figure 3-8 ($<u>^*$ and t^* representing the phase-averaged streamwise velocity and time normalized by $U_{b,max}$ and T, respectively). A phase-lag of about $\Delta t^*\approx 0.18$ is observed when the systolic peak to peak is compared in these two graphs. The maximum pulse velocity at the centre of the channel was approximately $0.72U_{b\text{-}max}$ whereas, for the steady case presented earlier, the centre-line velocity was about $1.55U_b$. The centre-line velocity is equal to $1.5U_b$ using Equation 13 (for any W/H>5 [8]), as well as from parallel plate flow theory [36], and, hence, the results from this study agrees well with these theoretical relations (within ±3.3%). The normalized phase-averaged streamwise velocity $<u>^*$ at location E is depicted in Figure 3-9 for 2y/H=0.33, 0.66 and 1. There are no significant phase shifts between these profiles. However, the profiles at 0<2y/H<0.44 both have distinct systolic and diastolic peaks (similar to the U_b profile in Figure 3-8) at $t^*=0.33$ and 0.46. At 0.44<2y/H<0.58, the diastolic peak starts to increase and at $0.58<2y/H<1$, the two peak locations merge (the identifiable diastolic peaks diminish) causing an almost flat profile at $0.33<t^*<0.45$.

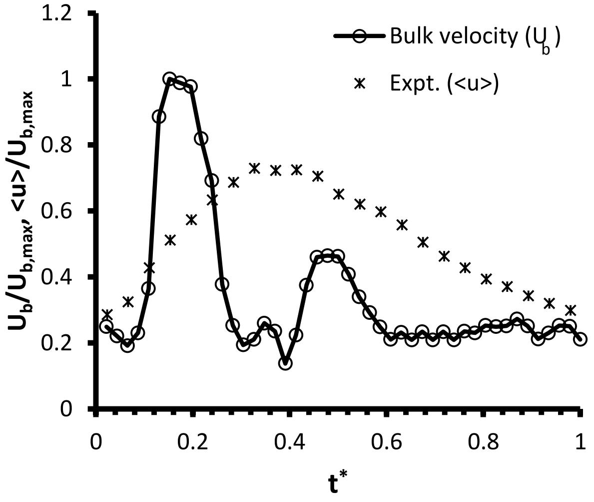

Figure 3-8 Bulk velocity (U_b) and phase-averaged streamwise velocity <u> normalized by $U_{b\text{-}max}$ at location E and 2y/H= 1 vs. normalized time (t^*) for the carotid pulse

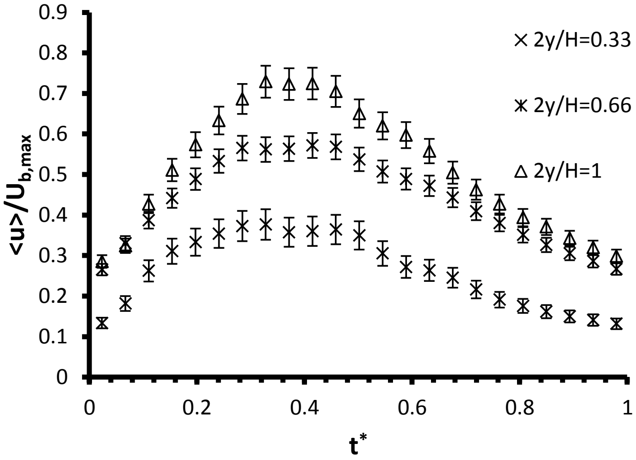

Figure 3-9 Phase-averaged streamwise velocity profiles <u> normalized by $U_{b,max}$ at 2y/H=0.33, 0.66 and 1 for location E for the carotid pulse (error bars are indication of experimental uncertainty)

3.3.5.1.1 Uniformity of the Carotid Pulse Flow

To examine the uniformity of the flow in the test section, the spanwise direction normalized phase-averaged velocity profiles $\langle u\rangle^*$ at $t_1^*=0.19$, $t_2^*=0.33$ and $t_3^*=0.85$ (corresponding to the acceleration phase of systole, peak systole and end of diastole, respectively) for locations A, B and C are illustrated in Figure 3-10. The profiles that belong to the same phase at the three different locations compare well with each other. Examining all of the phases revealed that there is no significant difference in the width of the uniform region of the flow in the test section and about 60% of the channel width ($-0.6<2z/W<0.6$) is exposed to uniform flow.

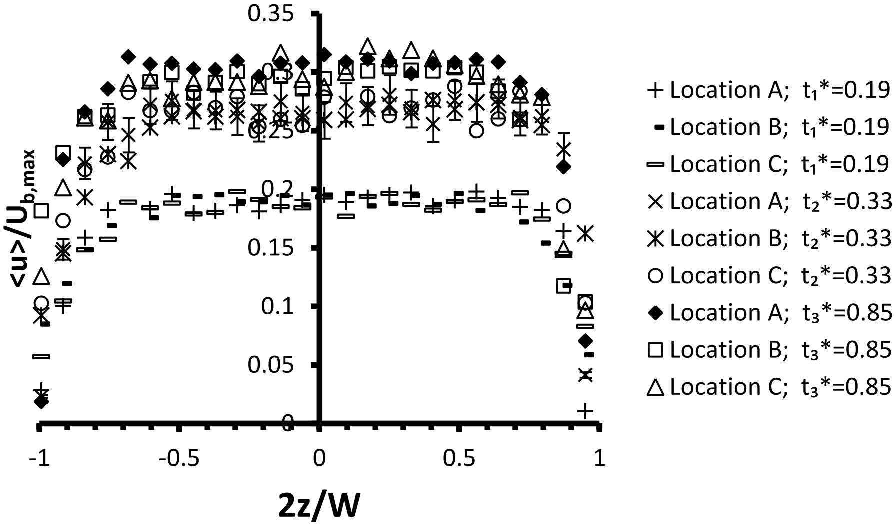

Figure 3-10 Streamwise direction phase-averaged velocity profiles <u> normalized by $U_{b,max}$ at locations A, B and C for the phases $t_1^*= 0.19$, $t_2^*= 0.33$ and $t_3^*= 0.85$ across the span of the channel $-1<2z/W<1$ for the carotid pulse (error bars are representative of experimental uncertainty)

3.3.5.1.2 Streamwise Velocities

After all of the data were phase-averaged, the velocities belonging to the corresponding bins across the channel half-height ($0<2y/H<1$) were examined to quantify the temporal change in the velocity profile. The streamwise direction normalized phase-averaged velocity profiles $<u>^*$ at $t_1^*=0.19$, $t_2^*=0.33$ and $t_3^*=0.85$ for locations D, E and F are presented in Figure 3-11. Comparing the graphs corresponding to the same phase of the cycle but at different locations, shows that there are no significant spatial differences, implying a fully developed pulsatile flow in the test section. Comparison between the temporal changes of the streamwise velocity profiles showed that the profiles become more blunt at $0<t^*<0.33$, then at $0.33<t^*<0.63$, the profiles tend toward a parabolic profile at heights about $0.88<2y/H<1$ and again at $0.63<t^*<1$, they tend to be more blunt at $0.88<2y/H<1$. This distortion of the velocity profiles is dependent upon the value of α [8]. At lower α, the velocity profiles are in phase with the pressure waveform and the velocity is parabolic at all times (consistent with the zero-frequency laminar steady flow for which $\alpha=0$ and the profile is parabolic). As α increases, inertial forces dominate and, hence, the profile becomes more blunt near the centre-line. At $0<t^*<0.33$, the fluid accelerates and the pressure gradients are higher causing the more blunt core region where, at $0.33<t^*<0.63$, the fluid decelerates and the pressure gradients start to increase. Hence, the profiles first gain a “parabola-like” shape and then this increase in pressure gradient causes the blunt region to re-occur at $0.63<t^*<1$ due to dominant inertial force effects. A similar pattern is reported by Ponzini *et al.* for a carotid waveform with $\alpha=4.7$ where about 30% of the vessel diameter near the centre has a blunt region [66].

The phase-averaged shear stresses $<\tau_w>$ at locations D, E and F are depicted in Figure 3-12. The general profile shape is similar to the $<u>$ profiles at locations close to the channel centre-line and both the systolic and diastolic peaks are visible in the graph. The WSS is positive indicating a unidirectional WSS over the test section and the minimum, maximum and average WSS over the entire pulse was found to be 3.32, 6.02 and 4.82 dyne/cm^2. The reported value for the mean WSS in the common carotid artery (CCA) is 4-15 dyne/cm^2 (depending on age, sex and health condition) [67-68].

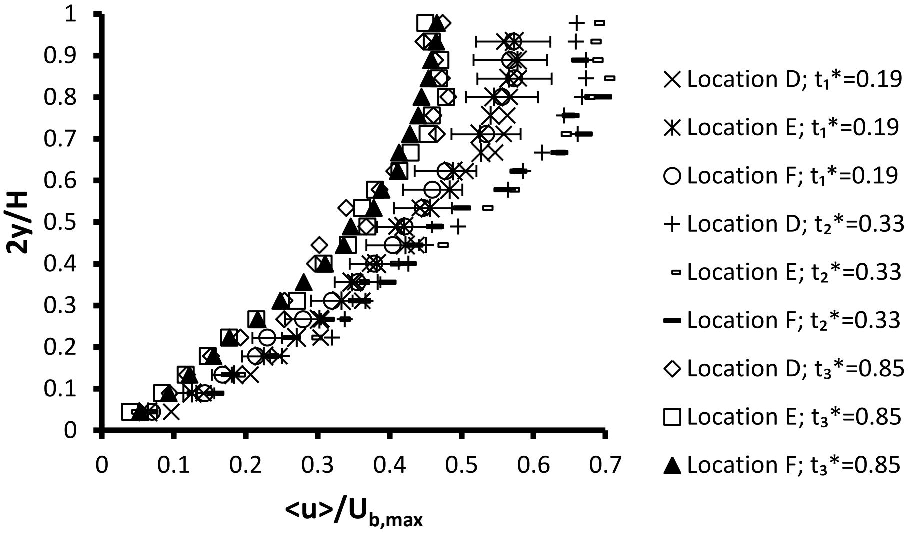

Figure 3-11 Streamwise direction phase-averaged velocity profiles <u> normalized by $U_{b,max}$ at locations D, E and F for the phases t_1^*, t_2^* and t_3^*=0.19, 0.63 and 0.85 across the channel half height 0<2y/H<1 for the carotid pulse (error bars are indication of experimental uncertainty and are drawn on one data set only for the clarity of the graph)

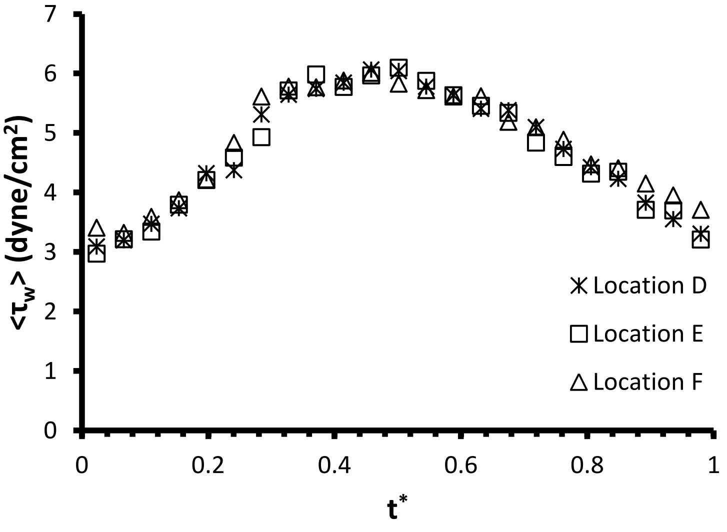

Figure 3-12 Phase-averaged wall shear stress $<\tau_w>$ vs. normalized time at locations D, E and F for the carotid pulse

3.3.5.2 Non-zero-mean Sinusoidal Pulse

A non-zero-mean sinusoidal pulse with f≈1.1 Hz (pulse period=920 ms) was produced by the pump. Local minimum, maximum and mean Re_o and α were $R_{0\text{-min}}$≈0, $Re_{0\text{-max}}$≈155, $R_{0\text{-mean}}$≈45 and α=2.76, respectively. The normalized phase-averaged streamwise velocity profile $<u>^*$ at 2y/H=1 for location D is illustrated vs. the normalized bulk velocity in Figure 3-13. A phase-lag of about Δt^*≈0.44 is observed when the peak-to-peak is compared in these two graphs and the maximum pulse velocity at 2y/H=1 is about $0.68U_{b\text{-max.}}$ The normalized phase-averaged streamwise velocity $<u>^*$ at location E is depicted in Figure 3-14. for 2y/H=0.33, 0.66 and 1. Phase shifts $|\Delta t^*|$ of about 9 and 5 are visible between the profiles at 2y/H=0.33 and 0.66 and between 2y/H=0.66 and 1, respectively.

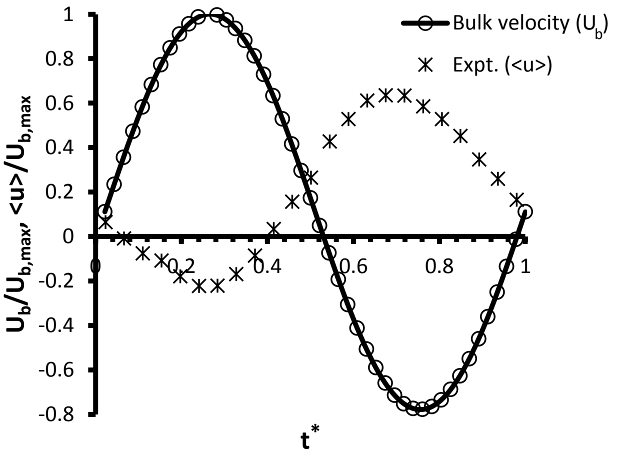

Figure 3-13 Bulk velocity (U_b) and phase-averaged streamwise velocity <u> normalized by $U_{b\text{-max}}$ at location E and 2y/H= 1 vs. normalized time (t^*) for the non-zero-mean sinusoidal pulse

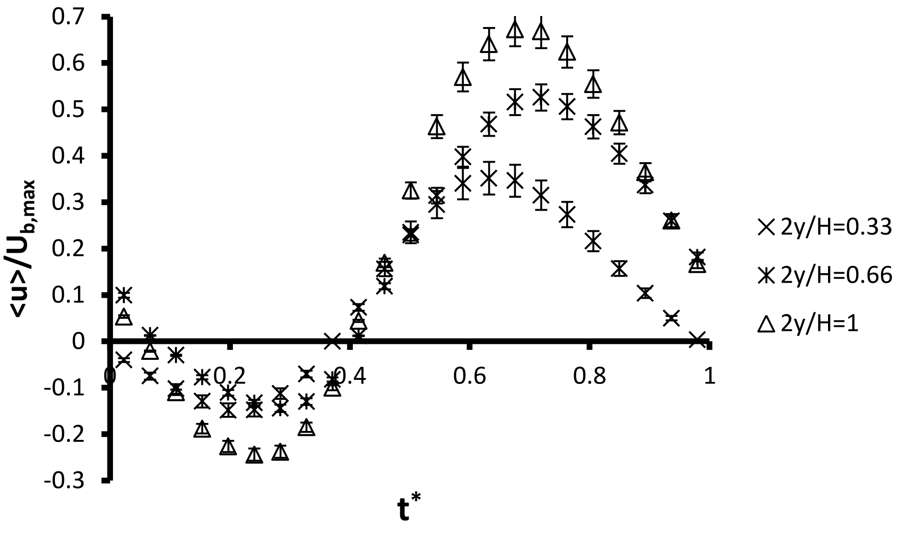

Figure 3-14 Phase-averaged streamwise velocity profiles <u> by $U_{b\text{-max}}$ at 2y/H=0.33, 0.66 and 1 for location E vs. normalized time (t^*) for the non-zero-mean sinusoidal pulse (error bars are indication of experimental uncertainty)

3.3.5.3 Uniformity of the Non-zero-mean Sinusoidal Pulse Flow

To examine the uniformity of the flow in the test section, spanwise direction normalized phase-averaged velocity profiles $<u>^*$ at $t_1^*=0.28$, $t_2^*=0.50$ and $t_3^*=0.72$ (corresponding to the minimum, middle and maximum phases of the cycle, respectively) for locations A, B and C are illustrated in Figure 3-15. The profiles that belong to the same phase at the three different locations compare well (with the differences <10%) with each other. Due to the pulsatility, a different uniform width over the span of the channel was achieved with 40% (-0.6<2z/W<0.6) being the shortest width exposed to uniform flow and, hence, 40% was taken as the overall uniform flow width for this pulsatile flow.

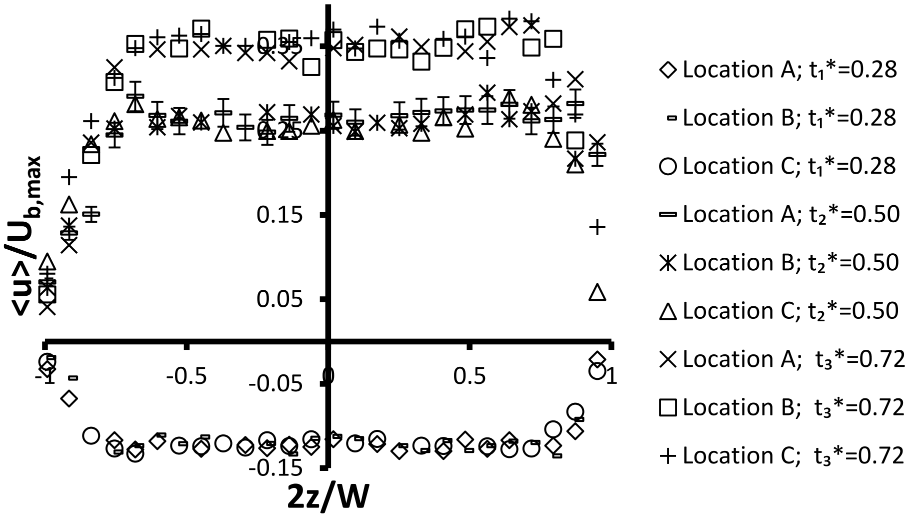

Figure 3-15 Streamwise direction phase-averaged velocity profiles <u> normalized by $U_{b,max}$ at locations A, B and C for the phases $t_1^*= 0.28$, $t_2^*= 0.50$ and $t_3^*= 0.72$ across the span of the channel $-1<2z/W<1$ for the non-zero-mean sinusoidal pulse (error bars are indication of experimental uncertainty and are drawn on one data set only for the clarity of the graphs)

3.3.5.3.1 Streamwise Velocities

The streamwise direction normalized phase-averaged velocity profiles $<u>^*$ at $t_1^*=0.28$, $t_2^*=0.50$ and $t_3^*=0.72$ for locations D, E and F are presented in Figure 3-16. Comparing graphs corresponding to the same phase of the cycle but different locations shows that there are no significant spatial differences (between the locations D, E and F) implying a fully developed pulsatile flow in the test section. Comparison between the temporal changes of the streamwise velocity profiles showed that at $0<t^*<0.088$ the near wall measured velocities are negative whereas the core velocities tend to be positive; these positive core region velocities then start to diminish to negative values at $0.09<t^*<0.40$. At $0.40<t^*<0.44$, the wall region velocities develop toward positive magnitudes and this trend extends to the core region at $0.44<t^*<0.84$. At $0.84<t^*<1$, which is immediately after the cycle peak, unlike the rest of the cycle the wall region connects to the core region smoothly through a "parabola-like" profile. Hence, when the pressure gradients reverse, the fluid near the wall tends to reverse direction easier than the core region. Also, some time must elapse before the viscous diffusion takes place toward the core [69]. This behaviour can also be described by α; since higher α reflects less viscous effects in the core region. Hale *et al.* have presented the velocity profiles for a sinusoidal pressure-driven flow (zero mean) with $\alpha=3.34$ [70]. The velocity profiles have identifiable wall and core regions; with the core region being more blunt (for about 50% of the vessel diameter) [70]. At the phase of the cycle where the bunt region appears, a local maximum was reported at a distance of 0.5 to 0.6 of the vessel radius (measured from the centre), whereas this local region was located at 0.3 to 0.55 of the channel half height for the current study (measured from the centre of the channel or $2y/H=0.45\text{-}0.7$). At $t^*=0.72$ another local maximum appeared at the channel centre-line in the current study which was not reported by Hale *et al.* [70]. Also, the profiles become "parabola-like" at about 30% of the pulse phases in their study. The ratio between the maximum and minimum centre-line velocity in the pulse was found to be ≈2.9 and 2.8 for the results reported by Hale *et al.* [70] and the current study, respectively.

The shear stresses were calculated using the same technique described for the carotid pulse and the phase-averaged shear stresses $<\tau_w>$ at locations D, E and F are depicted in Figure 3-17. The minimum, maximum and average WSS over the entire pulse was found to be -1.28, 2.02 and 0.25 dyne/cm^2, respectively.

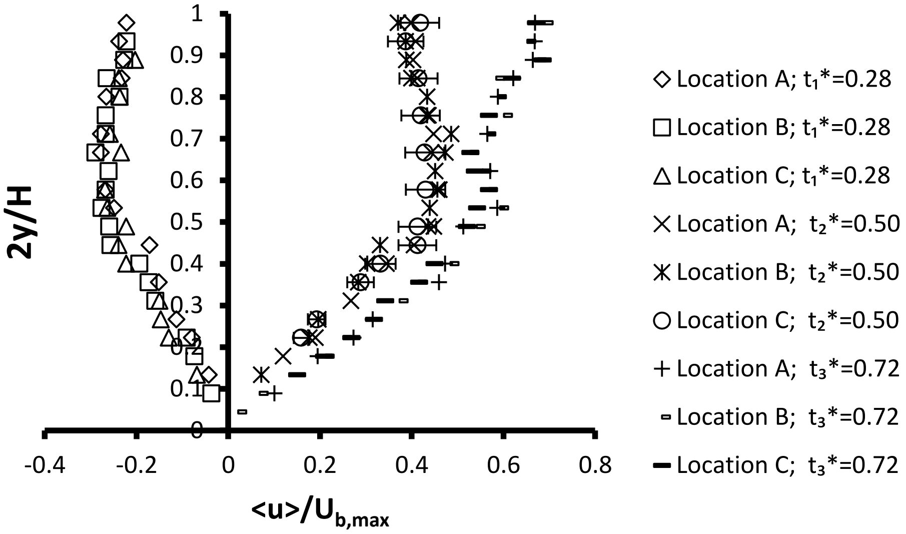

Figure 3-16 Streamwise direction phase-averaged velocity profiles <u> normalized by $U_{b,max}$ at locations D, E and F for the phases $t_1^*= 0.28$, $t_2^*= 0.50$ and $t_3^*= 0.72$ across the channel half height $0<2y/H<1$ for the non-zero-mean sinusoidal pulse (error bars are indication of experimental uncertainty and are drawn on one data set only for the clarity of the graph)

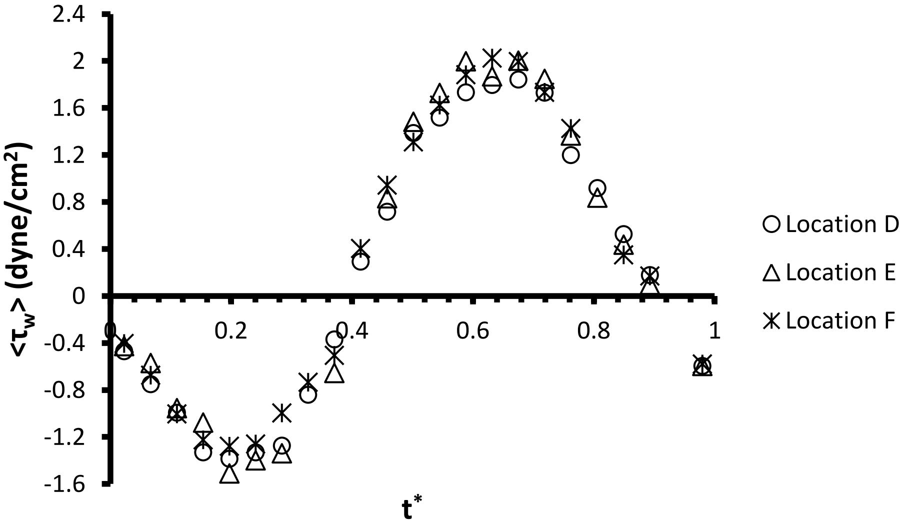

Figure 3-17 Phase-averaged wall shear stress $< \tau_w >$ vs. normalized time (t^*) at locations D, E and F for the non-zero-mean sinusoidal pulse

3.3.5.4 Oscillatory Shear Index

The oscillatory shear index (OSI) is a measure of the oscillatory nature of the shear stress, originally formulated by Ku *et al.* [71], which represents the fraction of the cardiac cycle over which the instantaneous shear stress vector forms an angle greater than 90° to the time-average direction of the same stress [72]. OSI is defined as

$$\mathrm{OSI} = 0.5\left(1.0 - \frac{\left|\int_0^T \tau_W \mathrm{d}t\right|}{\int_0^T |\tau_W|\, \mathrm{d}t}\right) \tag{3-15}$$

The OSI can vary between 0 and 0.5; where the former represents a uni-directional flow, whereas the latter is for the case where the shear stress changes equally in forward and backward directions. In the current study, the OSI for the carotid and the non-zero-mean sinusoidal pulse were found to be 0 and 0.38±0.01, respectively. The OSI is reported to range between 0 to 0.35 in a scale model of human carotid artery where the latter corresponds to an athero-prone location [71] and hence both of the pulsatile cases studied here have physiologically relevant OSI values.

3.3.6 Low-Re Steady Turbulent Flow (Re=2750 or Re_0=1830)

Although, *in vivo*, pulsatile blood flow is mostly laminar, at some complex geometrical locations such as stenosed bifurcations, the flow becomes intermittently turbulent before re-laminarization [14, 40]. Hence, it was critical to quantify WSS in low-Re turbulent flow. The Low-Re transitional behaviour makes WSS assessment more challenging. An aspect ratio of W/H≥7 is sufficient to ensure the two-dimensionality of a turbulent channel flow [73] and, hence, an aspect ratio of 9.72 for the current channel fulfils this condition. Velocity data were taken in coincident mode for blue and green beams. Reynolds decomposition was applied on the u and v velocity measurements to calculate the mean and individual fluctuating components of velocity in the u (U,u′) and v (V,v′) directions.

3.3.6.1 Mean Velocity and Turbulence Intensity Profiles and WSS Determination

In this section, the profiles of the streamwise mean velocity (U), turbulence intensities in the x and y directions (u_{rms}, v_{rms}), Reynolds shear stresses $\boldsymbol{RSS = -\rho\overline{u'v'}}$ obtained from the LDV measurements and WSS determination methods are presented and the results compared with the literature. The measurements were taken at locations D, E and F for verification of a fully-developed turbulent flow in the test section. For the mean velocity, the data were normalized by the bulk velocity (U_b=1.136 m/s). The mean streamwise velocity profiles across the channel half height (0<2y/H<1) at locations D, E and F are shown in Figure 3-18. The maximum normalized mean velocity at the channel centre-line reaches $(U/U_b)_{max}$=1.27 whereas Kim *et al.* have shown that quantity is Re-dependent [74], being 1.19 for Re=5600 and 1.17 for Re=13600. Comparing their data for Re=5600 with the current study, gives good agreement (error=($(U/U_b)_{max,\text{present study}}$- $(U/U_b)_{max,\text{ Kim } et\ al.}$)/$(U/U_b)_{max,\text{ Kim } et\ al.}$ ×100%=6.30%) despite the difference in Re. The friction velocity u_τ is defined as $u_\tau = (\tau_w/\rho)^{0.5}$ where τ_w is the wall shear stress [7]. τ_w and u_τ were evaluated using the polynomial fit to the mean velocity (U) profiles and were found to be 33.85±1.66 dyne/cm^2 and 5.82±0.12 cm/s (standard deviations of the three τ_w and u_τ values calculated at locations D, E and F, respectively). The Mean velocity profile data over 0<y<280 μm (y^+<22 where $y^+ = yu_\tau/\nu$) for location E (being representative of the other locations as well) is shown in Figure 3-19 where it may be seen that the velocity measured at y=0 is not exactly zero (U≈0.03 m/s). The same observation has been reported by Durst *et al.* [75] where the velocity data at a distance to the wall of less than half the LDV measurement volume diameter are overestimated, since the velocity at the wall must be zero (no-slip condition). At y values less than half the measurement volume diameter (≈34 μm or y^+≈2.6, in the current study), a virtual measurement volume centre is created at $d_s/2$ (see Figure 3-2) and, hence, the measured data are slightly larger than zero. A correction was applied to the velocity at y=0 to comply with the no-slip condition. Polynomial fittings for both the measured and corrected data are also shown in Figure 3-19. The shear rate ($\dot{\boldsymbol{\gamma}}$) was found to be 4770 and 4910 for the measured and corrected data, respectively; a difference of 3% $((\dot{\boldsymbol{\gamma}}_{\boldsymbol{corrected}} - \dot{\boldsymbol{\gamma}}_{\boldsymbol{measured}})/\dot{\boldsymbol{\gamma}}_{\boldsymbol{corrected}} \times \boldsymbol{100})$ which is within the experimental uncertainty. The nearest measurement to the wall (that was greater than half the measurement volume diameter) was at $y^+ \approx 2.8$ and at least two points were measured within the viscous sub-layer (i.e., $y^+<5$). Using this approach, τ_w across the three measurement locations was determined to be 33.85±1.35 dyne/cm^2 (standard deviation of the results at the locations D, E and F).

Figure 3-20 shows the turbulence intensity profiles in x and y directions (u_{rms} and v_{rms}) normalized by u_τ (u_{rms}^+ and v_{rms}^+, respectively) versus y^+ which have been compared with experimental data reported by Kreplin *et al.* at Re=5600 [74]. Both u_{rms}^+ and v_{rms}^+ are Re-dependent according to Antonia *et al.* [76] and with the increasing Re, both variables (u_{rms}^+ and v_{rms}^+) increase. For the current study, the maximum u_{rms}^+ is 2.82±0.02 (standard deviation of the three values at locations D, E and F) which is a difference of about +7.6% (within the experimental uncertainty) compared to the results reported by Kreplin *et al.* [74]. The peak values occur at $y^+ \approx 10$-14 and $y^+=13$ for the current study as well as results by Kreplin *et al.*, respectively. These results are also in good agreement with the other literature where the peak value and location are reported to be between 2.7 to 2.9 and at $10<y^+<15$ [77-78]. The scatter in the present u_{rms}^+ data is < ±12.8% which is within experimental uncertainty.

The v_{rms}^+ increases with distance the wall toward the channel centre-line. The agreement between the present data and results from Kreplin *et al.* [74] is good, where the differences (<12%) manifest the experimental uncertainty as well as the difference in Re between the two studies. Data for v_{rms}^+ tend to a value of about 0.7 and 0.8 at $y^+ \approx 30$ in both the present study and for that of Kreplin *et al.* [74]. Similar results are presented in other literature where v_{rms}^+ increases to a constant value of 0.7 to 1 [74, 76, 78] and has a descending trend at $y^+>80$ [42].

In a turbulent flow, the total shear stress is defined as $\tau_{total}=\tau_{viscous}-\boldsymbol{\rho\overline{u'v'}}$ where $\tau_{viscous}$ is calculated through Equation 3-10 and $-\boldsymbol{\rho\overline{u'v'}}$ is the turbulent Reynolds shear stress (RSS). At the wall (y=0) due to the no slip condition, the RSS component approaches zero and, hence, the only contribution is from the viscous shear stress. It has been well established that the RSS profile in a channel flow has a Re-dependent peak, outside of the viscous region, which can be correlated with the WSS [7]. According to channel flow experimental data [76], NRSS (NRSS=$-\overline{\boldsymbol{u'v'}}/u_\tau^2$) for Re_0=2970 and 39580 are approximately 0.65 and 0.90, respectively, with good agreement between experimental and direct numerical simulation (DNS) data. Since the Re_0 in this study is lower than those reported values and no data matching this Re_0 were found [76], an interpolation method was applied to the intermediate data reported by Antonia *et al.* [76] to find the NRSS corresponding to the current Re_0. This value was estimated to be approximately 0.58, returning an average value of u_τ=6.48±0.13 cm/s (standard deviation of the determined values at locations D, E, F). Consequently, τ_w was found to have a mean value of 40.89±1.82 dyne/cm^2 (standard deviation of the calculated values for locations D, E and F). The NRSS at locations D, E and F, along with a comparison with a study by Li *et al.* [79], are depicted in Figure 3-21. In their study, turbulent and transitional flows in microchannels of aspect ratio varying from 1 to 5 (width and height of 320-1080 μm and 190-330 μm, respectively) using micro-PIV were quantified. The peak NRSS values occurred at $y^+\approx$10-12 and y^+=14 for the current study and their study (for an aspect ratio of 5 where channel width and height were 1080 μm and 190 μm, respectively, at Re_0=1837), respectively. For the current study, the small values of NRSS at $y^+<4$ are followed by a sudden increase to a peak value at $y^+\approx7$ and then a sudden decrease to very small values at $y^+\approx17$ which is similar to the results reported by Li *at el.* [79] despite the higher NRSS after the peak (NRSS≈0.04) in that study. Li *et al.* [79] reported a peak value of 0.0010 for $-\overline{\boldsymbol{u'v'}}/U_0^2$ which compares well with the current value of 0.0011. The friction velocity and WSS determined from the gradient of the U profile and NRSS method were found to be different (the difference in parameter O is defined as $(O_{\text{-NRSS}} - O_{\text{-U profile}})/(O_{\text{-NRSS}} + O_{\text{-U profile}})/2$, where O can be substituted by u_τ or τ_w) by ≈3% and 5 %, respectively (these values are the average for locations D, E and F). The NRSS method overestimated both u_τ and τ_w, when compared to the results from the mean velocity (U) gradient method. The experimental conditions and WSS results are summarized in Table 3-3. Another common method for determining the WSS in turbulent flow is to apply the law of wall [36]. It has been reported that this method is not suitable for low-Re turbulent flow. According to the classical theory of Milikam, the log law is only appropriate for high-Re turbulent channel flow (at least order of 10^4) [7, 77] and, hence, this methods was not applied here.

Table 3-3 Summary of test conditions and results for turbulent flow

Location	Re_0	U_b (cm/s)	U_0 (cm/s)	u_τ (cm/s)-from RSS	u_τ (cm/s)-from U profiles	% difference in u_τ	WSS (dyne/cm^2) -from RSS	WSS (dyne/cm^2)-using U gradient
D	1833	113.6	146.7	6.41	5.66	12.4	40.25±6.3	31.97±3.83
E			145.8	6.67	5.93	11.7	43.37±6.8	35.09±4.21
F			144.7	6.35	5.88	7.7	39.05±6.1	34.50±4.14

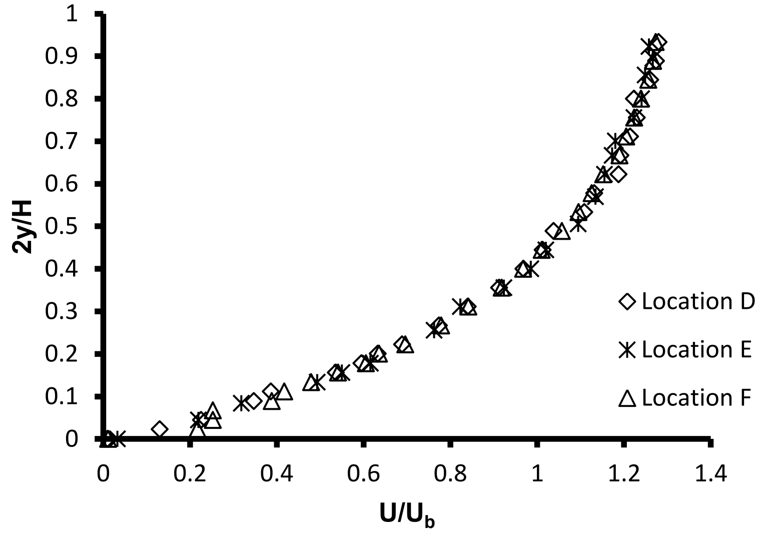

Figure 3-18 Mean streamwise velocity U profiles normalized by bulk velocity U_b at locations D, E and F at $0<2y/H<1$ for the low-Re turbulent flow ($Re_0=1830$)

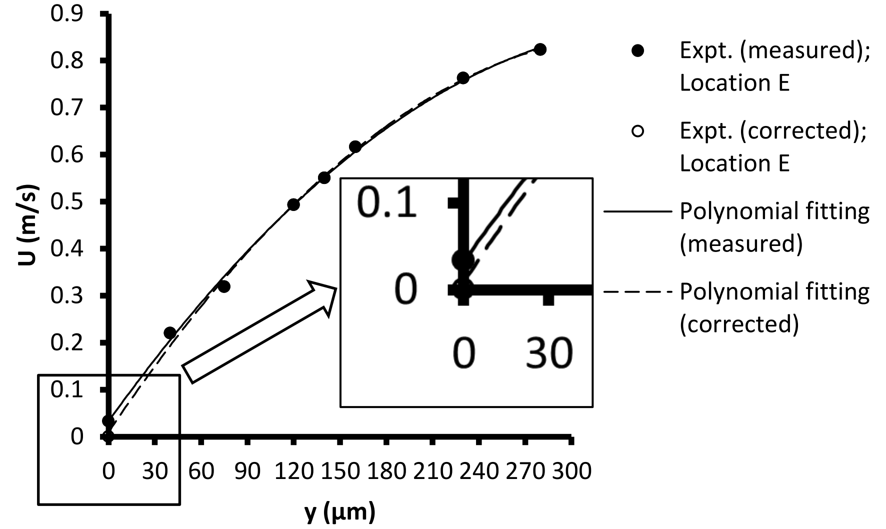

Figure 3-19 Streamwise mean velocity distribution in the near wall region of the channel (y<280 µm, 0<2y/H<0.311) along with polynomial fitting with np=2 for both the measured and corrected profile at y=0 (location E; Re_0=1830)

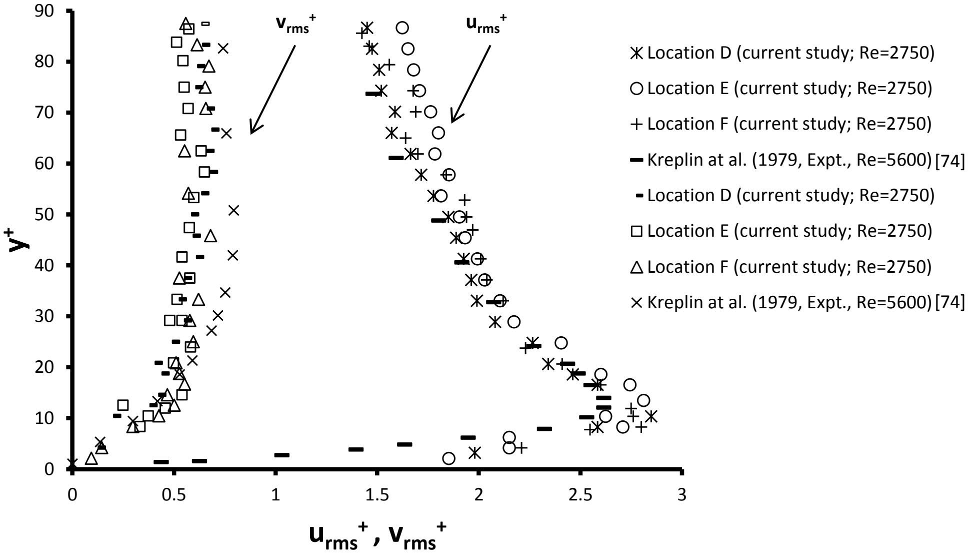

Figure 3-20 Turbulence intensities in x and y directions (u_{rms} and v_{rms}, respectively) normalized by the friction velocity across the channel half-height in wall units (y^+) at locations D, E and F for the low-Re turbulent flow with Re=2750 (Re_0=1830) compared with experimental data from Kreplin *et al.* [74]

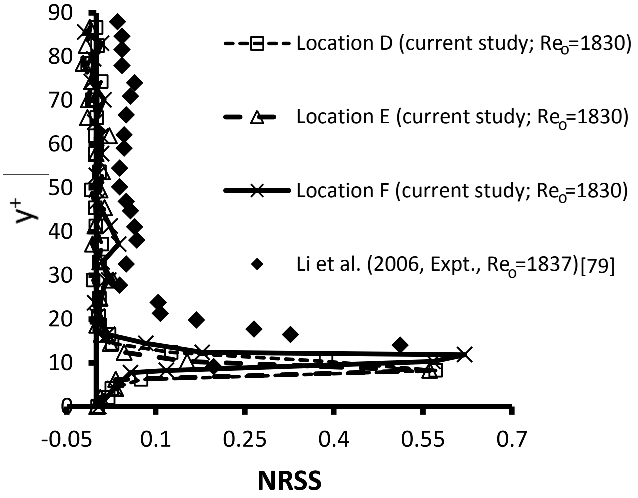

Figure 3-21 NRSS ($-\overline{u'v'}/u_\tau^2$) versus y^+ at locations D, E and F for the low-Re turbulent flow with Re_0=1830 (Re=2750) compared with results reported by Li *et al.* for Re_0=1837 [79]

3.4 Summary and Conclusions

The Laser Doppler Velocimetry (LDV) method was used to quantify the flow in a parallel plate flow chamber (PPFC) with D_h=3.26 mm and aspect ratio of 9.72 under steady (Re_0=750), two laminar pulsatile (carotid $Re_{0\text{-max}}$=560 and non-zero-mean sinusoidal $Re_{0\text{-max}}$=155) and a low-Re turbulent flow Re_0=1830 in order to quantify the wall shear stress (WSS) under various flow regimes. A mini-LDV probe (with a smaller half-angle of 3.9°, compared to conventional probes) was used in order to avoid the laser beams encountering the channel side walls. To the authors' knowledge, the present work represents the first detailed LDV measurements in a channel flow with a small hydraulic diameter which is on the threshold of conventional channels (3 mm). The feasibility of conducting the measurements in such a confined geometry was shown and a precise method for the wall location determination with a positional uncertainty of ($\approx \pm 27$ μm) was established and explained in detail. Additionally, a thorough analysis of the major sources of experimental uncertainty was conducted.

For the steady flow, the WSS was estimated from the experimentally measured data, as well as from the analytical solution of a laminar channel flow and the difference between the two methods was about ±9%. The measured flow was found to be uniform across the central 65-75% of the span of the channel.

Phase-averaged velocity data were analyzed for both pulsatile flow cases and the maximum flow in each pulse was found to be around 0.7 $U_{b\text{-}max}$, whereas this value is about 1.5 U_b for steady laminar flow [36]. The effects of Womersley number (α) on the phase-averaged streamwise velocity profiles were discussed and a consistent agreement between the present results and related studies was found. The flows were found to be uniform over approximately 60% and 40% of span of the channel for the carotid and non-zero-mean sinusoidal flows, respectively.

For the low-Re turbulent flow, at least two data points were measured in the viscous sublayer ($y^+<5$) and the turbulent statistics were also discussed. The WSS was estimated using two methods including determination through the Re-specific normalized Reynolds shear stress ($NRSS=-\overline{u'v'}/u_\tau^2$) and U profile gradient which agreed within ±5%. A sudden decrease in the NRSS values after the peak, similar to that found in previous work [79] could manifest the size of the channel (being in the lower threshold of conventional channels where $D_h>3$ mm) and possible transitional effects reported in $1800<Re_o<3000$ [7]. NRSS in other conventional channel turbulent flow (with D_h and δ of at least 56 mm and 15 mm) is reported to have more gradual decrease after the peak [7, 74].

Since these results are applied to study the effects of WSS on ECs, it was essential to investigate the effects of EC height as roughness elements on the flow. Since EC height (ε_c) is approximately 5 μm, hence, $\varepsilon_c^+=\varepsilon_c u_\tau/\nu\approx 0.4<5$ and the test section can be considered as hydraulically smooth walls and, consequently, the ECs don't have any effects on the friction [36].

3.5 References

[1] C. F. Dewey and S. R. Bussolari, "The Dynamic Response of Vascular Endothelial Cells to Fluid Shear Stress," *J. Biomech. Eng.,* vol. 103, pp. 177-185, 1981.

[2] S. R. Bussolari, F. Dewey and M. A. Gimbrone, "Apparatus for Subjecting Living Cells to Fluid Shear Stress," *Rev. Sci. Instrum.,* vol. 53, no. 12, pp. 1851-1854, 1982.

[3] R. M. Nerem, M. J. Levesque and J. F. Cornhill, "Vascular Endothelial Morphology as an Indicator of the Pattern of Blood Flow," *J. Biomech. Eng.,* vol. 103, pp. 172-176, 1981.

[4] S. Chien, "Mechanotransduction and Endothelial Cell Homeostasis; the Wisdom of the Cell," *Am. J. Physiol. Heart Circ. Physiol.,* vol. 292, pp. 1209-1224, 2007.

[5] J.-J. Chiu and S. Chien, "Effects of Disturbed Flow on Vascular Endothelium; Pathophysiological Basis and Clinical Perspectives," *Physiol. Rev.,* vol. 91, pp. 327-387, 2011.

[6] B. R. Blackman, K. A Barbee and L. E. Thibault, "In vitro Cell Shearing Device to Investigate the Dynamic Response of Cells in a Controlled Hydrodynamic Environment," *Ann. Biomed. Eng.,* vol. 28, no. 4, pp. 363-372, 2000.

[7] S. B. Pope, Turbulent flows, Cambridge: Cambridge, 2000.

[8] G. A. Truskey, F. Yuan and D. F. Katz, Transport Phenomena in Biological Systems, NY: Pearson, 2009.

[9] R. G. Bacabaca, T. H. Smith, S. C. Cowinc, J. J. Van Lanoona, F. T. Nieuwstadtd, R. Heethaarb and J. Klein-Nulend, "Dynamic Shear Stress in Parallel-Plate Flow Chambers," *J. Biomech.,* vol. 38, pp. 159-167, 2005.

[10] M.-a. Koo, J.-K. Kang, M. H. Lee, H. J. Seo, B.-J. Kwon, K. E. You, M. S. Kim, D. Kim and J.-C. Park, "Stimulated Migration and Penetration of Vascular Endothelial Cells into Poly (L-lactic acid) Scaffolds," *Biomat. Res.,* vol. 18, no. 7, pp. 1-8, 2014.

[11] P. F. Davies, A. Remuzzi, E. J. Gordon, C. F. Dewey and A. M. Gimbrone, "Turbulent Fluid Shear Stress Induces Vascular Endothelial Cell Turnover in Vitro," *Proc. Natl. Acad. Sci. USA,* vol. 83, pp. 2114-2117, 1986.

[12] W. E. Langlois and M. Deville, Slow Viscous Flow, Gewerbestrasse: Springer

International Publishing Switzerland, 2014.

[13] G. A. Truskey, A. Pinero and K. Barber, "Effects of Recirculating Flow on U-938 Cell Adhesion to Human Vein Endothelial Cells," *Am. J. Physiol. Heart Circ. Physiol.,* vol. 275, pp. 591-599, 1998.

[14] F. Ghalichi , X. Deng , A. De Champlain , Y. Douville , M. King and R. Guidoin, "Low Reynolds Number Turbulence Modeling of Blood Flow in Arterial Stenoses," *Biorheol.,* vol. 34, no. 4-5, pp. 281-94, 1998.

[15] A. Scotti and U. Piomelli, "Numerical Simulation of Pulsating Turbulent Channel Flow," *Phys. Fluids,* vol. 13, no. 5, pp. 1367-1383, 2001.

[16] J. C. Misra, B. Pal, A. Pal and A. S. Gupta, "Oscillatory Entry Flow in a Plane Channel with Pulsating Walls," *Int. J. Non-linear Mech.,* vol. 36, pp. 731-741, 2001.

[17] M. Seddighi, S. He, A. E. Vardy and P. Orlandi, "Direct Numerical Simulation of an Accelerating Channel Flow," *Flow Turbul. Combust.,* vol. 92, pp. 473-502, 2014.

[18] A. Valencia and L. Hinojosa, "Numerical Solutions of Pulsating Flow and Heat Transfer Characteristics in a Channel with a Backward-facing Step," *Heat Mass Trans.,* vol. 32, pp. 143-148, 1997.

[19] R. Mittal, S. P. Simmons and F. Najjar, "Numerical Study of Pulsatile Flow in a Constricted Channel," *J. Fluid Mech.,* vol. 485, pp. 337-378, 2003.

[20] O. Tutty, "Pulsatile Flow in a Constricted Channel," *J. Biomech. Eng.,* vol. 114, no. 1, pp. 50-61, 1992.

[21] U. Piomelli and J. Liu, "Large-eddy Simulation of Rotating Channels Flows Using a Localized Dynamic Model," *Phys. Fluids,* vol. 7, no. 4, pp. 839-847, 1994.

[22] N. Beratlis, E. Balaras, B. Parvinian and K. Kiger, "A Numerical and Experimental Investigation of Transitional Pulsatile Flow in a Stenosed Channel," *J. Biomech. Eng.,* vol. 127, pp. 1147-1157, 2005.

[23] M. Paul and M. Molla, "Investigation of Physiological Pulsatile flow in a Model

Arterial Stenosis using large-eddy and Direct Numerical Simulations," *Appl. Math. Model.,* vol. 36, no. 9, p. 4393–4413, 2012.

[24] M. Nabavi and K. Siddiqui, "A Critical Review on Advanced Velocity Measurement Techniques in Pulsating Flows," *Meas. Sci. Technol.,* vol. 21 , pp. 1-19, 2010.

[25] M. Teuffl , D. Trimis, A. Lohmoller, Y. Takedat and F. Durst, "Determination of Velocity Profiles in Oscillating Pipe-flows by Using Laser Doppler Velocimetry and Ultrasonic Measuring Devices," *Flow Meas. Instrum.,* vol. 3, pp. 95-101, 1992.

[26] S. G. Kandlikar and W. J. Grande, "Evolution of Microchannel Flow Passages-Thermohydaulic Performance and Fabrication Technology," *IMECE2002*, New Orleans, Louisiana, 2003.

[27] T. Argo and P. Wilson, "Measurement of Resonance Frequency of Single Bubbles using a Laser Doppler Vibrometer," *JASA Exp. Lett.,* vol. 123, no. 6, pp. EL121-EL126, 2008.

[28] S. Nakagawa, K. Nitta and M. Senda, "An Experimental Study on Unsteady Turbulent Near Wake of a Rectangular Cylinder in a Channel Flow," *Exp. Fluids,* vol. 27, pp. 284-294, 1998.

[29] S. So, H. Morikita, S. Takagi and Y. Matsmotu, "Laser Doppler Velocimetry of Turbulent Bubbly Channel Flow," *Exp. Fluids,* vol. 33, pp. 135-142, 2002.

[30] J. M. Verhelst and F. Nieuwstadt, "Visco-elastic Flow Past Circular Cylinders Mounted in a Channel: Experimental Measurements of Velocity and Drag," *J. Non-newton. Fluid Mech.,* vol. 116, pp. 301-328, 2004.

[31] Y. Zhang and D. Che, "Turbulent Statistics in a Rectangular Channel Flow with One Groove-Roughened Wall," in *Sixth International Conference on Fluid Mechanics*, Guangzhou, 2011.

[32] J. R. Castrejón-Pita, A. A. Castrejón-Pita, G. Huelsz and R. Tovar, "Experimental Demonstration of the Rayleigh Acoustic Viscous Boundary Layer Theory," *Phys. Rev.,* vol. 73, pp. 036601-1-5, 2006.

[33] C. Appel, J. Mantzaras, R. Schaeren, R. Bombach and A. Inauen, "Turbulent Catalytically Stabilized Combustion of Hydrogen/Air Mixtures in Entry Channel Flows," *Combast. Flame,* vol. 140, pp. 70-92, 2005.

[34] D. Marx, Y. Auregan, H. Bailliet and J. Valiere, "PIV and LDV Evidence of Hydrodynamic Instability over a Liner in a Duct with Flow," *J. Sound Vib.,* vol. 329, pp. 3797-3812, 2010.

[35] F. Arbeiter, S. Gordeev, V. Heinzel, D. Leichtle and E. Stratmanns, "Mini-channel Flow Experiments and CFD Validation Analyses with the IFMIF Thermo-hydraulic Experimental Facility (ITHEX)," *Fus. Eng. Des.,* vol. 82, p. 2456–2461, 2007.

[36] F. M. White, Fluid mechanics, New York: McGraw Hill, 2009.

[37] W. Lidai, J. Xia, J. Yao, K. I. Maslov and L. V. Wang, "Ultrasonically Encoded Photoacoustic Flowgraphy in Biological Tissue," *Phyical. Rev. Letters,* vol. 111, pp. 204301-1-5, 2013.

[38] TSI, "FlowSizer version 2.0.4," Shoreview, MN, 2011.

[39] A. Melling, "Tracer Particles and Seeding for Particle Image Velocimetry," *Meas. Sci. Technol.,* vol. 8, p. 1406–1416, 1997.

[40] E. Loth, "Numerical Approaches for Motion of Dispersed Particles, Droplets and Bubbles," *Prog. Energ. Combust.,* vol. 26, p. 161–223, 2000.

[41] T. Khadivi, "Experimental and Numerical Study of Flow Structure," *PhD thesis,* University of Western Ontario, Canada, 2012.

[42] L. Keirsbulck , L. Labraga and M. Haddad, "Influence of Blowing on the Anisotropy of the Reynolds Stress Tensor in a Turbulent Channel Flow," *Exp. Fluids,* vol. 40, p. 654–662, 2006.

[43] R. Mei, "Velocity Fidelity of Flow Tracer Particles," *Exp. Fluids.,* vol. 22, pp. 1-13, 1996.

[44] F. Durst, R. Miller and J. Jovanovic, "Determination of the Measuring Position in

Laser-Doppler Anemometry," *Exp. Fluids,* vol. 6, pp. 105- 110, 1988.

[45] R. W. Radomsky and T. A. Thole, "Detailed Boundary Layer Measurements on a Turbine Stator Vane at Elevated Freestream Turbulence Levels," *J. Turbomach.,* vol. 124, pp. 104-118, 2002.

[46] V. C. Patel and M. R. Head, "Some Observations on Skin Friction and Velocity Profiles in Fully Developed Pipe and Channel Flows," *J. Fluid Mech.,* vol. 38, pp. 181-201, 1969.

[47] A. J. Wheeler and A. R. Ganji, Introduction to Engineering Experimentation, Prentice Hall: Pearson, 2010.

[48] R. F. Kunz, S. W. D' Amico, P. Vassallo and M. A. Zaccaria, "LDV Measurements of Confined Parallel Jet Mixing," *J. Fluid Eng.,* vol. 123, pp. 567-573, 2001.

[49] F. Durst, J. Jovanovic and J. Sender, "LDA Measurements in the Near-wall Region of a Turbulent Pipe Flow," *J. Fluid Mech.,* vol. 295, pp. 305-335, 1995.

[51] R. E. Edwards, "Report of the Special Panel on Statistical Particle Bias Problems in Laser Anemometry," *J. Fluid Eng.,* vol. 109, pp. 89-93, 1987.

[52] S. C. Kehoe, "An Experimental Investigation of the Hemodynamic Effects at Mildly Stenosed Carotid Artey Bifurcation," *MESc thesis*, University of Western Ontario, London, Canada, 2001.

[53] J. M. Osterlund, "Experimental Studies of Zero Pressure-Gradient Turbulent Boundary-Layer Flow," *PhD thesis*, Royal Institute of Technology, Stockholm, 1999.

[54] S. Einav, D. Stolero, J. M. Avidor and D. Elad, "Wall Shear Stress Distribution along the Cusp of a Tri-leaflet Prosthetic Valve," *J. Biomech. Eng.,* vol. 12, pp. 13-18, 1990.

[55] F. F. Mark, C. B. Bargeron, O. J. Deters and M. H. Friedman, "Variations in Geometry and Shear Rate Distribution in Casts of Human Aortic Bifurcations.," *J.*

Biomech., vol. 22, pp. 577-582, 1989.

[56] D. N. Ku, D. P. Giddens, C. Z. Zarin and S. Glago, "Pulsatile Flow and atherosclerosis in the Human Carotid bifurcation: Positive Correlation Between Plaque Location and Low Oscillating Shear Stress," *Arterioscler.,* vol. 5, pp. 293-302, 1985.

[57] R. S. Fatemi and S. E. Rittgers, "Derivation of Shear Rates from Near-Wall LDA Measurements under Steady and Pulsatile Flow Conditions," *J. Biomech. Eng.,* vol. 116, pp. 361-367, 1994.

[58] Z. Lou, W. Yang and P. D. Stein, "Errors in the Estimation of Arterial Wall Shear Rates that Results from Curve Fitting of Velocity Profiles," *J. Biomech.,* vol. 26, no. 45, pp. 183-390, 1993.

[59] W. C. Reynolds and A. K. F. M. Hussain, "The Mechanics of an Organized Wave in Turbulent Shear Flow; Part 3, Theoretical Models and Comparisons with Experiments," *J. Fluid Mech.,* vol. 54, pp. 263-268, 1972.

[60] S.-C. Wu, "Phase-averaged Method Applied to Periodic Flow Between Shrouded Co-rotating Disks," *Int. J. Rot. Machin.,* vol. 8, no. 6, pp. 413-421, 2002.

[61] S. Kefayati, J. S. Milner, D. W. Holdsworth and T. L. Poepping, "In Vitro Shear Stress Measurements Using Particle Image Velocimetry in a Family of Carotid Artery Models: Effect of Stenosis Severity, Plaque Eccentricity, and Ulceration," *PLOS ONE,* vol. 9, no. 7, pp. 0098209-1-12, 2014.

[62] B. Enaux, V. Granet, O. Vermorel, C. Lacour, L. Thobois, V. Dugue and T. Poinsot, "Large Eddy Simulation of a Motored Single-Cylinder Piston Engin: Numerical Strategies and Validation," *Flow, Turb. Combust.,* vol. 86, no. 2, pp. 153-177, 2011.

[63] O. V. Filatova, A. A. Sidorenko and Y. Y. Shorobogatov, "Age and Sex Dependence of Hemodynamic Parameters of Human Internal Carotid Artery," *Hum. Physiol.,* vol. 40, no. 5, pp. 93-102, 2014.

[64] J. A. Cosgrove, J. M. Buick, S. J. Tonge, C. G. Munro, C. A. Greated and D. M.

Campbell, "Application of the Lattice Boltzmann Method to Transition in Oscillatory Channel Flow," *J. Physics,* vol. 36, p. 2609–2620, 2003.

[65] I. C. Campbell, J. Ries, S. S. Dhawan, A. A. Quyyumi, W. R. Taylor and J. N. Oshinski, "Effect of Inlet Velocity Profiles on Patient-Specific Computational Fluid Dynamics Simulations of Carotid Bifurcations," *J. Biomech. Eng.,* vol. 134, pp. 051001-8, 2012.

[66] R. Ponzini, C. Vergara, G. Riz, A. Veneziani, A. Roghi, A. Vanzul, O. Parodi and A. Redaelli, "Womersley Number-Based Estimates of Blood Flow Rate in Doppler Analysis: In Vivo Validation by Means of Phase-Contrast MRI," *IEEE Trans. Biomed. Eng,* vol. 57, no. 7, pp. 1807-1714, 2010.

[67] S. K. Samijo , R. Barkhuysen, J. Willigers , K. M. Leunissen , L. A. Ledoux, P. J. Kitslaar and A. P. Hoeks, "Wall Shear Stress Assessment in the Common Carotid Artery of End-stage Renal Failure Patients," *Nephron.,* vol. 92, p. 557–563, 2002.

[68] J. N. Oshinski, J. L. Curtin and F. Loth, "Mean-average Wall Shear Stress Measurements in the Common Carotid Artery," *J. Cardiovasc. Mag. Res.,* vol. 8, pp. 717-722, 2006.

[69] K. B. Chandran, S. E. Rittgers and A. P. Yoganathan, Biofluid Mechanics, Boca Raton: CRC Press, 2012.

[70] J. F. Hale, D. A. McDonald and J. R. Womersley, "Velocity Profiles of Oscillating Arterial Flow, with Some Calculations of Viscous Drag and Reynolds Number," *J. Physiol.,* vol. 128, pp. 629-640, 1955.

[71] D. N. Ku, D. P. Giddens and C. K. Zarins, "Pulsatile Flow and Atherosclerosis in the Human Carotid Bifurcation," *Atherosclerosis,* vol. 5, no. 3, pp. 293-302, 1985.

[72] P. K. Singha, A. Marzoc, B. Howa, D. A. Rufenacht , P. Bijlenga, A. F. Frangi , P. Lawford, S. C. Coley, D. R. Hose and U. J. Patel, "Effects of Smoking and Hypertension on Wall Shear Stress and Oscillatory Shear Index at the Site of Intracranial Aneurysm Formation," *Clin. Neurol. Neurosurg,* vol. 112, p. 306–313,

2010.

[73] M. P. Schultz and K. A. Flack, "Reynolds-number Scaling of Turbulent Channel Flow," *Phy. Fluids,* vol. 25, pp. 025104-1-14, 2013.

[74] J. Kim, P. Moin and R. Moser , "Turbulent Statistics in Fully Developed Channel Flow at Low Reynolds Number," *J. Fluid. Mech.,* vol. 177, pp. 133-166, 1987.

[75] F. Durst, J. Lekakis, J. Jovanovic and Q. Ye, "Wall Shear Stress Determination from Near-Wall Mean Velocity Data in Turbulent Pipe and Channel Flows," *Exp. Fluids,* pp. 417-428, 1996.

[76] R. A. Antonia, M. Teitel and J. Kim, "Low-Reynolds-Number Effects in a Fully Developed Turbulent Channel Flow," *J. Fluid. Mech.,* vol. 236, pp. 579-605, 1992.

[77] R. Moser, "Direct Numerical Simulation of Turbulent Channel Flow up to Re=590," *Phy. Fluids,* vol. 11, pp. 934-945, 1999.

[78] C.-Y. Chen, P. G. Menon, W. Kowalski and K. Pekkan, "Time resolved OCT-μPIV: A New Microscopic PIV Technique for Non-Invasive Depth Resolved Pulsatile Flow Profile Aquision," *Exp. Fluids.,* 54, pp. 1426-1435, 2013.

[79] H. Li, M. G. Olsen, "Aspect Ratio Effects on Turbulent and Transitional Flow in Rectangular Microchannels as Measured With MicroPIV, " J. Fluids Eng., vol. 128, pp. 305-315, 2006.

Chapter 4

4 Quantification of Morphological Modulation, F-Actin Remodeling and PECAM-1 (CD-31) Re-distribution in Endothelial Cells in Response to Fluid-Induced Shear Stress under Various Flow Conditions

4.1 Introduction

This section provides a detailed literature review on the effects of fluid-induced shear stress on EC morphometric parameters, F-actin and PECAM-1 (and the quantification methods, if applicable) followed by an outline of the experimental details. Finally, the main results are discussed and conclusions are drawn.

4.1.1 Endothelial Dysfunction and Relevance to Atherosclerosis

Cardiovascular diseases (CVDs) are the number one cause of mortality globally [1]. Atherosclerosis which is a type of CVD is an inflammatory disease of blood arteries in which the luminal diameter of the artery is decreased due to the accumulation of substances such as low density lipoproteins (LDL) that become trapped in the extracellular matrix of the subendothelial space [2] (for more details on artery wall structure, see section 1-2 in Chapter 1). Research has revealed that the development of advanced atherosclerosis can lead to serious clinical events such as heart attack or stroke due to the occlusion and/or rupture of the affected vessel [3] (for more details, see section 1-5 in Chapter 1).

There are many risk factors associated with this multifunctional inflammatory disease such as elevated LDL [4], hypertension, genetics and smoking [3]. Although the exact mechanism by which the disease develops remains elusive, it is widely accepted that the endothelial dysfunction due to the response-to-injury hypothesis is the first step in the initiation of atherosclerosis [3, 5]. Healthy endothelial cells (ECs) maintain vascular hemostasis through monitoring/controlling of permeability, inflammation, injury repair and vascular tone [6]. ECs are capable of sensing both mechanical and biochemical signals and transducing them into intra-/extracellular responses which modulate the tissue structure/function [7]. Endothelial dysfunction is often associated with an inconsistent vasoconstriction in response to vasodilating agents, due to an impaired activity of endothelial nitric oxide synthase (eNOS) or the inactivation of NO [8]. Increased expression of adhesion molecules such as intracellular adhesion molecule-1 (ICAM-1), vascular cell adhesion molecule-1 (VCAM-1) and E-Elastin/P-Elastin [9] can be initiated by pro-inflammatory mediators facilitating the recruiting and adhering the inflammatory cells into the endothelium which is also considered as an atherogenic process [10].

4.1.2 EC Morphological change and Stress Fibre Re-localization in Response to Wall Shear Stress

ECs respond to blood flow induced mechanical stimuli (e.g., wall shear stress-WSS) through mechanotransduction [9] (for more details on mechanotransduction, see section 1-4 in Chapter 1) which leads to inflammation and tissue remodeling by events such as proliferation, apoptosis, cell-cell and cell-extracellular matrix interaction [7]. It has been known for almost five decades that hemodynamic factors play a key role in EC dysfunction [11-12]. Previous research has shown that WSS-induced mechanical stimuli alter EC morphology and cytoskeleton organization [13-15] (see Figure 1-9 for representative images on the effects of hemodynamics on EC morphology and cytoskeletal organization). There has been much effort put into studying the relationship between the EC morphology and the flow direction *in vivo* [16-17] since it has been shown that EC morphology is a key indicator of EC health [18]. For example, Dewey reported that the stress fibres in the lower thoracic aorta where the WSS was expected to be high were strongly aligned with the direction of flow while ECs with very few stress fibres with no distinct orientation were seen when samples were taken from the inferior vena cava where WSS was expected to be low [14]. Due to the difficulties and restrictions associated with *in vivo* studies in this area, most have been conducted *in vitro* demonstrating similar results to *in vivo* studies. The results from *in vitro* studies reveal differential remodeling patterns of ECs when exposed to various hemodynamic forces such as steady, pulsatile and disturbed flows [13, 15, 19-20].

Dewey exposed bovine aortic endothelial cells (BAECs) to a WSS of 1-5 dyne/cm^2 in a cone and plate viscometer for up to 8 days and the typical closed-packed polygonal configuration of the cells remained unchanged. In contrast, ECs exposed to a WSS of 8 dyne/cm^2 were remodeled into a uniform ellipsoidal configuration with their major axes aligned with the flow direction [14] with the actin filaments being prominent and oriented with the major axis of the cell (i.e., in the flow direction) [14]. Levesque *et al.* investigated the morphometric parameters of ECs exposed to 10, 30 and 85 dyne/cm^2 and showed that with EC exposure to 85 dyne/cm^2, the shape index (S.I.=$4\pi A_c/P_c^2$ where A_c and P_c are the cell area and perimeter, respectively) and angle of orientation with the flow direction after about 10 hours were around 0.5 (S.I. for static control was 0.83) and 18° (45° for the static control), respectively They also showed that S.I., for the same exposure time, is dependent on the WSS magnitude [21].

Helmlinger *et al.* studied the effects of three pulsatile flow patterns including a non-reversing sinusoidal (type 1) WSS of 40±20 dyne/cm^2, reversing sinusoidal (type 2) WSS of 20±40 dyne/cm^2 and 10±15 dyne/cm^2 and purely oscillatory (type 3) WSS of 0±20 dyne/cm^2 and 0±40 dyne/cm^2 (all with frequency of 1 Hz) [22]. For types 1 and 2, the S.I. was decreased (compared to control) proportional to the mean value of each pulsatile case. ECs exposed to these flow types (i.e., 1 and 2) reorganized their actin filaments into long stress fibres aligned with the flow direction and appeared to be somewhat thicker than the stress fibres in the ECs treated with a steady WSS. ECs subjected to type 3 flow, however, did not become aligned with flow direction and the S.I. remained almost the same as in the static (control) condition. The actin distribution was diffuse and the high concentration centres, with randomly oriented stress fibres, were present, similar to the static condition. Levesque *et al.* [23] reported that the S.I. tended to decrease with increasing constant laminar WSS ranging from 15-90 dyne/cm^2 (increments of 15 dyne/cm^2) using bovine aortic endothelial cell BAECs as a model. They have also shown that the S.I. for non-reversing pulsatile flow was smaller than the S.I. when the ECs were exposed to a steady WSS having either the maximum or minimum WSS of that pulsatile flow, indicating a stronger elongation effect due to the pulsatile nature of the flow.

Galbraith *et al.* [24] found that both cell and F-actin alignment initially increased (in the first 3 hours) and then decreased to about 20°, in the presence of 15 dyne/cm^2 WSS. Schnittler *et al.* [25] exposed ECs to 5 dyne/cm^2 of WSS for the duration of 4 hours and significant F-actin density and alignment were observed compared to the control conditions. The cells were not fully aligned and this could have been due to the duration of the exposure. Vozzi *et al.* [26] quantified the structural re-organization of ECs when exposed to very low WSS values of 0, 0.105, 0.35 and 1.05 dyne/cm^2 by defining the eccentricity factor as $e=\sqrt{(1-(b/a)^2)}$ where a and b were defined as the length of the major and minor axes of the cell separately. They reported the e value to be around 0.4 for the static condition and around 0.95 for the other three cases. They also reported a similar e value (about 0.9-0.95) for an *in vivo* case, revealing that ECs respond to even very low values of WSS. Simmers *et al.* [27] examined the effects of growth media on ECs under arterial flow with the minimum and maximum WSS being about -2 and 18 dyne/cm^2 and found that the static condition S.I. of about 0.75, dropped to (and stabilized at) about 0.65 under flow conditions.

Dick *et al.* [18] investigated the effects of statin therapy on EC morphology and F-actin filaments under static conditions and a steady WSS of 12.5 dyne/cm^2 and found that the ECs in both cases had disorganized F-actin filaments and a round shape suggesting that, despite the application of physiologically relevant level of WSS, other factors (e.g., drugs) may alter the remodeling pattern of ECs. Wang *et al.* [28] showed that ECs pre-aligned with the primary flow direction started to re-align in the new direction when the primary flow was switched to an orthogonal direction. The studies discussed above reveal that ECs have a robust cytoskeletal structure that is also flow dependent.

4.1.3 Quantification of F-actin Filaments (Bundles) Organization

The majority of the research studies carried out on the effects of the WSS on stress fibres in ECs have been limited to a qualitative description of the events occurring during re-localization of the actin filaments. These qualitative evaluations mostly indicate whether or not the stress fibres are aligned with flow direction, if they are central/peripheral and what their density and thickness look like [9-10, 12-13, 15, 18, 29]. Despite the beneficial general knowledge conveyed by qualitative descriptions, quantitative analyses better aid our understanding regarding the polarity of the stress fibres, their time-dependent remodeling pattern and how well the cells become aligned with the application of WSS. Petrol *et al.* [30] presented a quantitative analysis of stress fibre orientation during a corneal wound contraction by using a Fourier transform technique and defined an orientation index (O.I.) to describe the temporal and spatial changes in stress fibres and their relevance to the wound healing process. Yoshighi *et al.* [31] developed an image processing filter to quantify the orientation and density of actin fibres. Ayres *et al.* [32] described, in detail, how to measure fibre alignment in electrospun material using a two-dimensional fast Fourier transform (2D FFT). Van der Meel *et al.* [33] applied 2D FFT to analyze the actin filament alignment and defined the summation of the normalized intensities in the first peak 30° as an alignment index. Lai *et al.* [34] applied a similar technique to study EC organization and migration on aligned vs. randomly distributed collagen fibrils. Cetera *et al.* [35] used an algorithm to define the boundaries of cells in a given epithelium and applied 2D FFT on actin bundles within each cell to assign an overall alignment angle per cell. These angles were then employed to define an order parameter (S). From the literature discussed here it is clear that FFT-based quantification of actin filament alignment provides more accurate information in a single cell/cellular network, when compared to merely descriptive reports on the imaging results.

4.1.4 Effects of WSS on PECAM-1

Platelet endothelial cell adhesion molecule (PECAM-1) also known as cluster of differentiation 31 (CD31), is a protein that makes up a large portion of EC intercellular junctions. It is a member of the immunoglobulin superfamily expressed by the entire vascular endothelium in the adult [36].

Schnittler *et al.* [37] found that junctional staining for PECAM-1 in ECs exposed to 20 dyne/cm^2 remained unchanged for several hours. Osawa *et al.* [38] have reported rapid tyrosine phosphorylation (i.e., considered to be one of the main steps in signal transduction) of PECAM-1 when ECs are exposed to 5 dyne/cm^2 or higher and have suggested that PECAM-1 is a mechanotransduction molecule. Sho *et al.* [39] reported up-regulation of PECAM-1 for ECs exposed to high flow preceding cell proliferation in an *in vivo* study. Tzima *et al.* [40] showed that PECAM-1, along with two other adhesion molecules, comprise a mechanosensory complex which are sufficient to confer responsiveness to hemodynamic forces and that this pathway is required for the earliest events in atherogenesis. By *in vivo* and *in vitro* studies, Harry *et al.* [41] showed that

PECAM-1 contributed to atherosclerotic lesion formation in regions with disturbed flow by NFκB-mediated gene expression. Chiu *et al.* [42] investigated the effect of flow on an *in vitro* model of ECs cultured on smooth muscle cells (SMC) by exposure to 12 dyne/cm^2 and found that ECs in both static and flow conditions showed clear circumferential PECAM-1 bands while the actin filaments were elongated with the flow direction. These studies show that PECAM-1, as a junctional protein, can be visualized to serve as an indicator of the cell-cell contact. Although PECAM-1 is shown to be a part of a mechanosensory pathway activated by mechanical stress, its modulation when exposed to different flow regimes and the exact role this protein plays in atherogenesis, is not fully understood yet.

4.1.5 Summary of the Literature Review

Both *in vivo* and *in vitro* studies have confirmed that ECs are responsive to different flow conditions. These studies have shown that randomly oriented polygonal-shaped ECs, initially in static condition, become elongated (ellipsoidal), with their major axes and F-actin filaments aligned with the flow direction, when exposed to steady laminar or non-reversing pulsatile flow (including arterial flows) of average or high WSS (>4 dyne/cm^2 [8]). In contrast, ECs exposed to low WSS or disturbed (i.e., low velocity and reversing) flows did not show any significant morphological changes compared to the static control, with short and randomly oriented stress fibres. No literature was found on the effects of low WSS on the F-actin organization. Also, some discrepancies were seen between the results of different studies (e.g., between [14] and [26]) where it is not clear how the low WSS affects the EC morphology. Gaining insight into EC response is crucial to understanding the robustness of the EC cytoskeletal structure and whether a certain level of WSS is required to initiate the F-actin remodeling. Also, from the literature, the correlation between a cell angle of orientation vs. its F-actin filament alignment when exposed to the flow condition remains elusive.

Although some quantitative methods have been developed and formulated recently for analysis of F-actin in ECs, these methods have not yet been applied as a comparative tool between various flow conditions. Since *in vitro* experiments are highly sensitive to factors such as EC type and passage number, examining the EC response to different

WSS profiles using an identical experimental set-up is beneficial in terms of reducing the bias due to the cell phenotype.

Finally, PECAM-1, as a junctional protein, is found to be a part of a mechanosensory complex; yet its morphological response to different flow conditions has not yet been investigated.

4.1.6 Objectives

In this study, an *in vitro*, physiologically-relevant facility, based on the parallel plate flow chamber (PPFC) concept was designed, developed and tested for the feasibility of conducting EC culture exposure to hemodynamic environments (for details see Chapter 2). Since flow quantification in a PPFC has somewhat remained elusive in the majority of the related published work (for more details see Chapter 3), experimental flow quantification techniques were employed to precisely measure the WSS over the endothelium model (EC coverslip). The objective was to investigate the effects of various flow regimes (including those known to have athero-promoting vs. athero-protective effects) on EC morphology and cytoskeletal structure under similar experimental conditions, to quantitatively analyze the results for any significant trends that can extend our current knowledge of EC response to hemodynamics flow and to make new contributions toward the understanding of the cellular events in the initiation and development of diseases such as atherosclerosis.

The current research program aims to provide both descriptive as well as quantitative analysis to link the findings with the current knowledge in this area. Also, the results from the quantitative analysis will be applied to examine the hypothesis that EC elongation with flow correlates with the F-actin bundle flow-induced alignment. No other work was found in the literature that has applied an in-depth quantitative approach to the study of the morphometric changes and remodeling patterns of ECs under diverse flow conditions and, hence, the present results also represent a data base for comparison purposes in future studies.

4.2 Materials and Methods

4.2.1 Flow Apparatus

A PPFC was employed as the major component of the flow facility in a closed-loop system connected to a positive displacement pump (CompuFlow 1000 MR, Shelley Medical Imaging Technology, Canada), capable of producing steady flows (volume flow rate Q=0.1-50 ml/s), realistic physiological flows (e.g., carotid waveform) and user defined waveforms (e.g., non-zero mean sinusoidal waveform). The flow loop also consisted of a reservoir for the cell culture medium and a controlled heating unit to maintain the fluid temperature at 37 ºC in the vicinity of the cellular monolayer (see Figure 2-2 for a schematic of the experimental set-up).

The flow chamber consisted of top and bottom cavities both manufactured from ULTEM 1000 with the exception of the working section which was made from precision glass (Angstrom Precision Optics Inc., USA). The top and bottom cavities were held together by evenly-distributed fine threaded screws. Beneath the bottom cavity of the test section, a cylindrical cavity (53 mm diameter, 15.9 mm depth) was fabricated. This insert, along with the glass working section on the top cavity, provided optical access for sample visualization as well as flow measurement. Vacuum silicon grease (Dow Corning, USA) was applied to prevent leakage between the glass working section and the top cavity (see Figure 2-4 for a schematic of the PPFC employed in this study).

Upstream and downstream flow development transition lengths of 251 mm and 94 mm (based on theoretical calculations [43]), respectively, were chosen to ensure fully developed flow over ECs. The channel had a rectangular cross section and the test section dimensions were 22 × 17.5 × 1.8 mm (L × W × H =length, width and height, respectively) where the endothelium monolayer model (on the coverslip) was placed flush with the wall flow in an insert on the bottom cavity. The flow medium was stored in a reservoir which was hooked up to a filtering unit consisting of a peristaltic pump (Piper Pump, Canada) and a sterile disposable filtering unit with pore size of 0.45 µm (Mellipak, Sigma Aldrich, USA). The filtration loop was circulated at volume flow rate of about 1.5-2 ml/s. For sample condition monitoring while the experiments were in progress, a

Micromaster infinity optics microscope (Fisher Scientific Inc., USA) was employed.

Dulbecco's Modified Eagle Medium (DMEM) solution was used for the flow experiments. This medium was prepared in-house for each experiment. 12.78 g/L DMEM powder (without phenol red, Wisent, USA), 10 mM/L HEPES (Wisent, USA), and 10 mL/L Antibiotic-Antimycotic (the original solution containing 10,000 units/mL of penicillin, 10,000 µg/mL of streptomycin, and 25 µg/mL of Fungizone, Life Technologies Inc., Canada) were dissolved in nano-pure water. After the medium was prepared, the pH level was adjusted to 7.4 by adding NaOH pellets to comply with physiological conditions. Characterization of the media including density and viscosity measurements, as well as its suitability for use with live cells was carried out. The viscosity and the fluid density were measured to be 0.737±0.0012 mPa.s and 997.96±0.12 kg/m^3 (see Chapter 2 for details).

4.2.2 Cell Culture

Passage 2 Porcine Aortic Endothelial cells (PAECs) were chosen for this study as their response to shear stress has been studied previously [44]. ECs were cultured on 100 mm diameter culture dishes in DMEM (Gibco, Canada) and 20 % fetal bovine serum (FBS, Gibco, Canada) and were kept at 37 ºC in a 5% CO_2 incubator until grown confluent. The cell medium was refreshed every 48 hours. Cell passages of 5 to 10 were used for the flow experiments. Once confluent, the cells were detached by 0.25 % Trypsin-EDTA (Life Technologies Inc., Canada) and plated on 22 × 22 mm (number 2) autoclaved coverslips (VWR, USA) using DMEM and 10% FBS and kept in the incubator until confluent (about two to three days). No antibiotics were used in the cell culture medium. The coverslips were then mounted in the hemodynamic channel for flow exposure experiments.

4.2.3 Flow Quantification

The effects of four different types of flow, including low steady laminar (LSL), medium steady laminar (MSL), non-zero-mean sinusoidal laminar (NZMSL) and laminar carotid (LCRD) waveforms on ECs were studied. The flow quantification was carried out in separate experiments using Laser Doppler Velocimetry (LDV), which is a single-point velocity measurement technique based on the Doppler frequency shift of light scattered from very small particles in the fluid (for more details see section 1-5-1 in Chapter 1). The WSS then was calculated by polynomial regression to determine the velocity gradient and, hence, WSS (see Chapter 3 for detailed information on the WSS measurements). The WSS profiles produced by the four flow conditions are depicted in Figure 4-1. The small mean value of the WSS for the NZMSL flow was imposed to ensure nutrition delivery to the cells [9]. The flow was found to be uniform over 65-75 %, 40% and 60% in the span of the endothelium monolayer (coverslip) for the LSL/MSL, NZMSL and LCRD flow conditions, respectively. Both pulsatile flows had a physiologically relevant [45] period of 920 ms (frequency of about 1.1 Hz).

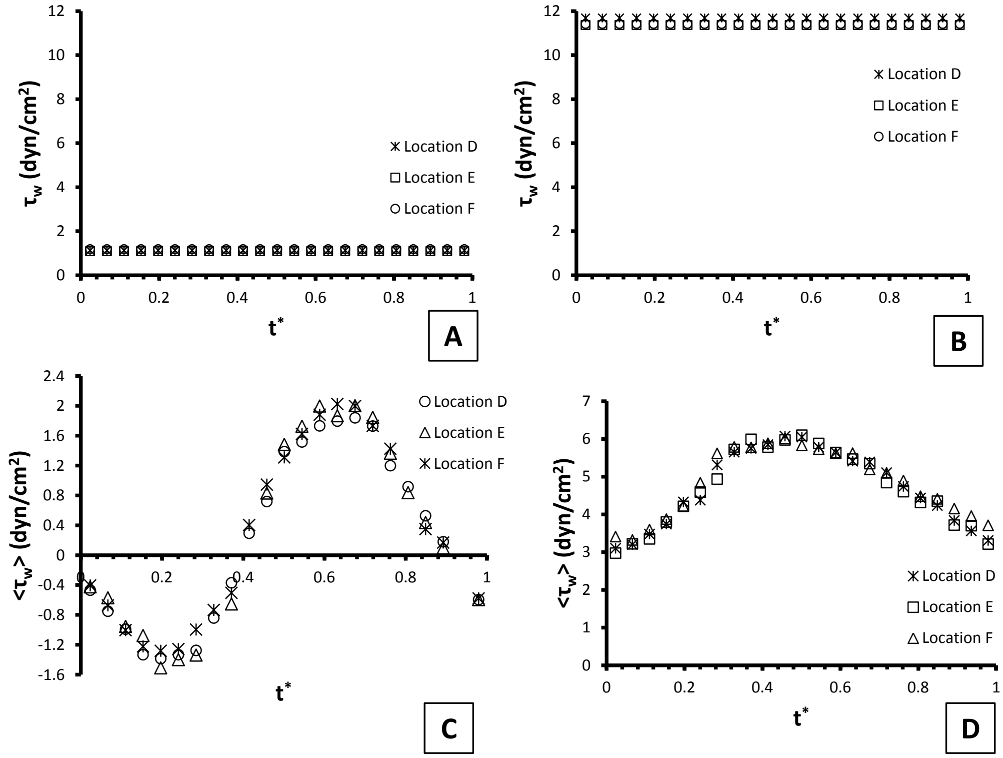

Figure 4-1 Illustration of the experimentally-quantified WSS associated with the four different flow regimes studied (τ_w and t^* representing the WSS and the time normalized by the pulse period for pulsatile cases. For cases A and B, since the flow is steady, the graph representation of the WSS is only illustrative for comparison purposes); (A) low steady laminar (LSL) with WSS of 1.13±0.10 dyne/cm^2; (B) medium steady laminar (MSL) with WSS of 11.5±0.9 dyne/cm^2; (C) non-zero-mean sinusoidal laminar (NZMSL) with the minimum, maximum and mean WSS of -1.28, 2.02 and 0.25 dyne/cm^2; (D) laminar Carotid (LCRD) with the minimum, maximum and mean WSS of 3.32, 6.02 and 4.82 dyne/cm^2.

4.2.4 Flow Experiment Procedure

For each experiment, after sterilization (for detailed information see Chapter 2), the flow loop was filled with the filtered medium and the operating conditions adjusted until the desired temperature of 37 °C was achieved. A variable transformer (Superior Electric, Canada) ranging from 0-240 V was used to adjust the temperature according to the applied flow rates. By trial and error, the set value for the LSL, MSL, NZMSL and

LCRD flows were found to be 50, 85, 33 and 70 V, respectively. The flow loop then was halted to install the coverslips in the PPFC test section. Natural light was found to be a source of contamination, due to the cytotoxic effects of light-exposed HEPES in the medium, and, hence, the experiments were carried out in a dark room [46-47]. According to Helmlinger *et al.*, the S.I. change between various flow conditions (including steady laminar ranging from 10-60 dyne/cm^2 and reversing flows) for WSS exposure durations of 6 and 22 hour, was not greater than 16% [22]. Similarly, Levesque *et al.* reported that the S.I. remained unchanged after 10 hours for ECs subjected to 10 dyne/cm^2 of WSS [16]. Also, considering the smaller magnitudes of WSS in the current study, each experiment was run for 10 hours.

After each experiment, the coverslip was disassembled from the flow chamber, marked for the flow direction and washed with a phosphate buffered saline (PBS) prior to fixation in 3.7% formaldehyde/PBS in a 4 °C fridge for 30 minutes. The fixative was then removed and the coverslips were kept in PBS in the 4 °C fridge.

4.2.5 Immunofluorescent Staining

A 2% bovine serum albumin (BSA) solution was prepared by adding 0.02 g BSA (powder) per mL of PBS. For blocking non-specific antibody binding, each coverslip, with fixed ECs, was placed on 100 mm diameter dish (covered with parafilm), and 360 μL of BSA solution was added to the coverslip to incubate the ECs at room temperature (RT) for 45 min. The BSA was then aspirated and the coverslip was washed in PBS. The cells were incubated with 360 μL of mouse anti-pig CD31 (PECAM-1) antibody (AbD Serotec, USA) at a concentration of 1:50 in BSA for 45 min at RT and then washed in PBS three times (5 min each). Cells were then incubated with 360 μL of anti-mouse lgG Alexa Fluor® 488 conjugate (Life Technologies, Canada) at a concentration of 1:50 (as the secondary antibody) for 45 min at RT. The coverslip was then washed with PBS three times (5 min each). To stain for F-actin filaments, the cells were incubated with 360 μL of Alexa Fluor® 568 Phalloidin (Life Technologies, Canada) at a concentration of 1:10 for 45 min at RT and then washed in PBS three times (5 min each). Hoechst 33342 (10 mg/mL solution in water, Life Technologies, Canada) at a concentration of 1:1000 was used to stain the cell nuclei. The coverslip was then washed again three times in PBS (5 min each) and the excess PBS on the back of the coverslip was gently wiped off. A single drop of Fluoromount aqueous mounting medium (Sigma Aldrich, Canada) was added on a glass microscope slide and the coverslip was gently mounted on the slide so that the cell containing side faced the mounting media. The slides were kept in a 4 °C fridge for 24 hours before confocal microscopy.

4.2.6 Confocal Microscopy

The cells were imaged on a Zeiss LSM410 confocal microscope (Carl Zeiss) using a 40x Plan Apo water immersion objective. The magnification was set such that the region of interest (ROI) was 320 μm × 320 μm or 512 × 512 pixels. Z-stacks (1 μm increments) were taken for the entire cell thickness (height). Zeiss LSM Image Browser (ver. 4.2.0.121) software was used to apply the maximum 3D projection on the z- stacks. Five fields of view were chosen, based on the previous findings related to the uniform flow region for each experiment. All the treatments (i.e., coverslips) were blinded (by assigning random codes) for quantification.

4.2.7 Image Processing

All the images were imported to NIH ImageJ software (ver. 1.6.0_20) [48] for image processing. Morphological measurements, as well as cytoskeletal remodeling quantification, were carried out as described in the following sections.

4.2.7.1 Morphological Analysis

The morphological parameters of EC area, perimeter, angle of orientation with the flow direction and S.I. were quantified. The cell area and perimeter were measured manually using the freehand selection tool to trace the cell boundaries. The angle of orientation (θ_o), was defined as being the angle between the cell major axis and the flow direction ($-90° < \theta_o < +90°$) where $\theta_o=0°$ and ±90° represent those cells fully aligned with and orthogonal to the flow, respectively. The angle tool was used to for quantification of θ_o. Chiu *et al.* reported the accuracy of this manual method to be within 1% when applied to calculating the angles for shapes with known angles [42]. The S.I. is a measure of how round or elongated a cell is and it ranges between 0 and 1, the former corresponding to a straight line whereas the latter describes a circle. A schematic of the morphological parameters discussed here is depicted in Figure 4-2. To quantify the number of cells per ROI, nuclei count (Hoechst staining) was used.

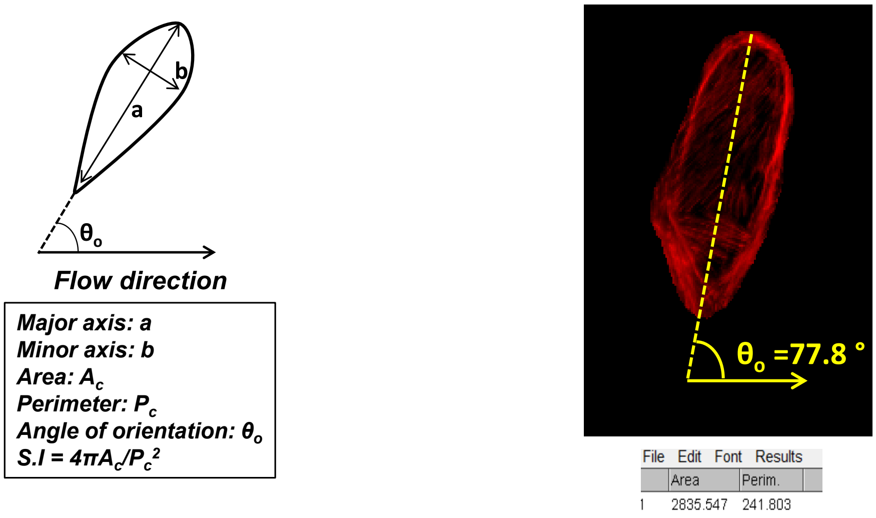

	Area	Perim.
1	2835.547	241.803

Figure 4-2 (A) Illustration of the morphological parameters of an EC; (B) a representative morphological calculation for an EC using ImageJ software. The angle was measured by the angle tool and the cell was traced using the freehand selection tool (F-actin filaments are shown as red bundles)

4.2.7.2 F-actin Filaments Directionality Quantification

For determining the directionality of F-actin filaments within the ECs, a 2D FFT method was applied. The 2D FFT function converts the spatial information (pixel intensity) in an image to a frequency domain representation and shows the power spectrum [32]. This function in ImageJ is based on an implementation of the 2D Fast Hartley Transform (FHT). A 2D Hartley transform, H(k,l), of function I(n,m), which is the pixel intensity in this case, on an M ×N domain is given by [49]

$$\mathbf{H(k,l)} = \sum_{\mathbf{m=0}}^{\mathbf{M-1}}\sum_{\mathbf{n=0}}^{\mathbf{N-1}} \mathbf{I(n,m)}\left[\mathbf{cos}\left(\frac{\mathbf{2\pi nk}}{\mathbf{N}}\right)+\mathbf{sin}\left(\frac{\mathbf{2\pi nk}}{\mathbf{N}}\right)\right]\left[\mathbf{cos}\left(\frac{\mathbf{2\pi ml}}{\mathbf{M}}\right)+\mathbf{sin}\left(\frac{\mathbf{2\pi ml}}{\mathbf{M}}\right)\right] \tag{4-1}$$

$$\mathbf{k = 0, \ldots, N-1, \qquad l = 0, \ldots, M-1}$$

In order to perform this analysis, the ROI containing F-actin filaments was converted into an 8-bit grayscale image. The 2D FFT was applied using the Process>FFT function in the ImageJ software. The transformed image was then contrasted to exclude the low intensity, high frequency signal (further from the centre of the image) including the noise and image edge effects [32-33]. The remaining frequency domain contains grayscale pixels representing information regarding the general fibre (F-actin) directional structure in the original image. The resulting image was rotated by 90° (the direction was irrelevant) since this method applied a 90° rotation on the F-actin filament directions [33, 35]. Using the Edit>Selections>Fit circle tool, a circle was located at the centre of the resulting image. Applying the ImageJ oval profile plug-in (authored by B. O'Connell, available for download at: http://rsb.info.nih.gov/ij/plugins/oval-profile.html), radial sums of the pixel intensities along each radial slice from the centre of the circle to the periphery were plotted against the corresponding angle (0°-360°). Radial sums of the intensities for every 10° [33] from 0° to 180° [32] (due to symmetry) in the frequency domain image were calculated (for visualization of the location of these bands within the ECs, see Figure 4-3). The resulting intensities for each angle were correlated with the number of fibres in that direction in the original image of the F-actin filaments.

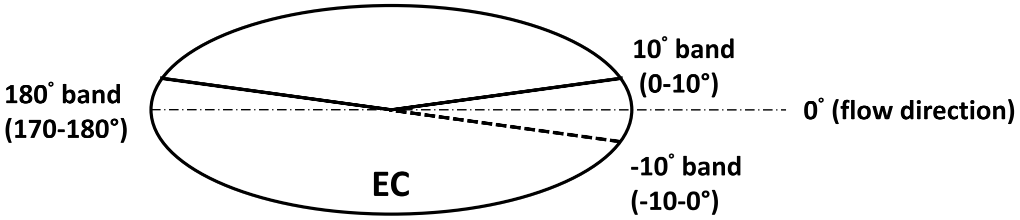

Figure 4-3 **Schematic of locating the 10° bands. The angles were measured with respect to the flow direction (i.e., 0°).**

In order to gain more comparative values for quantifying the F-actin arrangement in various cases, the radial intensity sums were normalized. For normalization, a base value equal to 98% of the minimum intensity (calculated as the outcome of the FFT analysis) was subtracted from all of the intensity values. The 98% level was chosen by examining various values ranging from 95 to 99% and the resulting normalized profiles for 97 and 98% were in close agreement; with the maximum error associated with respective points (in a given radial band) being within 7.8%. All of the modified values were then normalized by the sum of these values and the results were reported in percent. As a summary the normalized intensity was defined as

Normalized intensity=((original intensity in each 10° increment-98% of the minimum intensity among all of the bands)/(sum of the intensities after subtracting the 98% of the minimum intensity from each intensity value) (4-2)

For an illustration of the method described, see Figure 4-4. An alignment index (A.I.) was defined as

A.I=(sum of the relative pixel intensities in the 10° and 180° bands) (4-3)

The A.I. is a measure of the alignment of the actin filament with the flow direction. If all of the filaments are in the first and last 10° bands, the A.I. equals to 1, whilst no alignment in these two bands returns a value of zero.

4.2.7.3 PECAM-1 Morphological Analysis

For quantifying the PECAM-1 peripheral band density in cell-cell junctional sites, ROI was converted into Red/Green/Blue (RGB) colour format and the colour threshold tool was used to manually adjust the brightness for choosing only the peripheral PECAM-1 and excluding the intercellular PECAM-1. The total area associated with the chosen pixels was then calculated. The cell count was quantified by the blue nuclei stain. PECAM-1 relative density (P.R.D.) per EC was defined as

P.R.D. = total peripheral PECAM-1 area in a ROI/ (Number of ECs in that ROI × Average EC area in the ROI) × 100 % (4-4)

For visualization on quantifying the PECAM-1 localization technique described, see Figure 4-5.

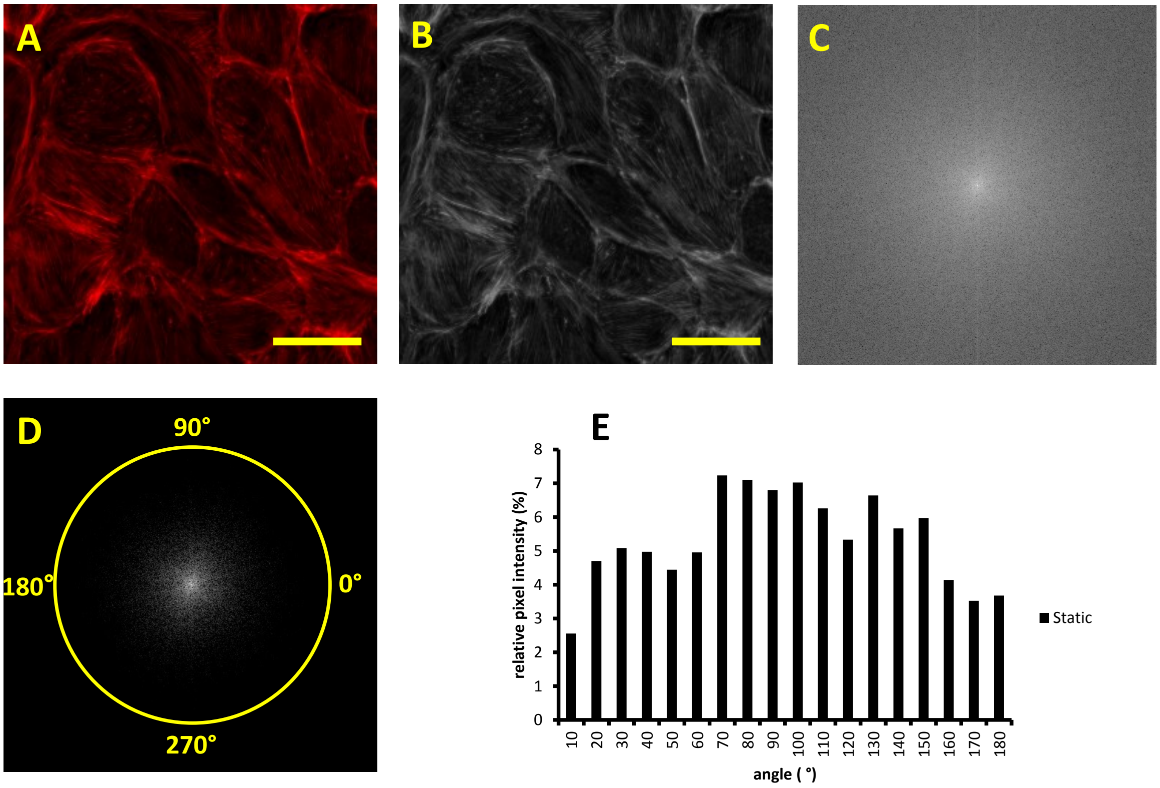

Figure 4-4 Illustration of the method for determining the F-actin filament directionality using 2D FFT for the cells in the static control. (A) A 160 × 160 μm^2 image cutout of F-actin filaments (red) was taken from an image. (B) The image was converted into an 8-bit grayscale image. (C) Then, it was transformed to the frequency domain applying the 2D FFT function and the resulting image was rotated by 90°. (D) The image was then contrasted and the pixel intensities were summed for every 10° peripheral band. (E) Histogram showing the relative pixel intensities (%) in 10° increments. In the present case, a somewhat uniform distribution of the relative intensities represents the orientation of the F-actin filaments in every direction for the static condition. The maximum values observed at angles 70°-110° may also represent noise due to edge effects, as described by Ayres *et al.* [32]. Scale bar=40 μm

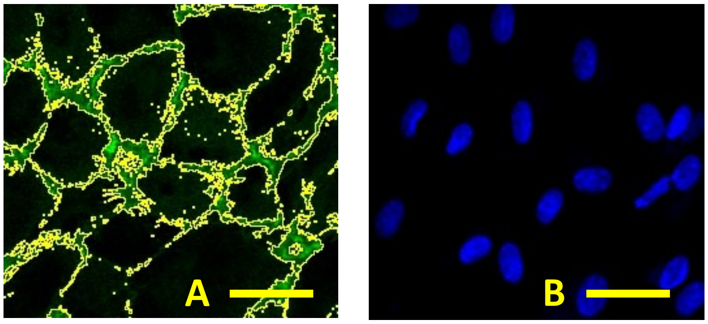

Figure 4-5 Illustration of quantifying the PECAM-1 localization for ECs in the static condition. (A) A ROI representing the PECAM-1 (CD31, marked by green stain) was converted into a RGB colour image and the brightness was adjusted through colour threshold adjustments to select the peripheral PECAM-1 for calculating the desired area occupied by the selected pixels. The average of the two repetitions of the manual area selection, along with the default area selection by ImageJ, was considered as the total peripheral PECAM-1 area where the ROI (B) nuclei were stained in blue for the EC cell count.

4.2.8 Statistical Analysis

All of the experiments were run in triplicate (n=3). The images were taken at least at 5 different ROI for each sample. At least N=80-100 ECs were analyzed for each sample. All the samples were analyzed by a one-way analysis of variance (one-way ANOVA) followed by a Tukey's *post hoc* test with a 95% confidence level. Values were reported as mean ± standard deviation error of the mean (SEM). Statistical analysis was performed using SPSS (ver. 22) software [50]. A p-value of less than 0.05 was considered statistically significant. A statistical difference is indicated by different superscripts on the bar graphs representing the results.

4.3 Results and Discussion

4.3.1 Visual Observations

As described in Chapter 2, one of the advantages of the current hemodynamic facility is real time microscopy. After installation of the sample in the test rig, the ECs were monitored for any detectable change in their morphology. In the first 1 hour after cell exposure to the flow, no observable change was noted in any of the experiments. However after 1-2 hours of flow exposure, the ECs had undergone a change in cell morphology detectable as a size change. This initial cell response was likely due to the initiation of cytoskeletal remodeling of ECs. Levesque *et al.* [21] reported the S.I. to be 0.83, 0.75 and 0.7 after a time (t) = 60, 90 and 120 minutes of exposure to a WSS of 85 dyne/cm^2. Time dependent S.I. monitoring of ECs exposed to a pulsatile arterial flow (maximum WSS of 20 dyne/cm^2) by Simmers *et al.* [27] showed the largest gradient of S.I. vs. time at $0<t<6$ hours. Our visual observation confirms the other reported studies that EC remodeling in response to flow is highly dynamic and rapid, with significant changes occurring in the first few hours of flow exposure.

4.3.2 Effect of WSS on EC morphology

In this section the effects of the four quantified flows on the EC area, perimeter, angle of orientation and S.I. will be presented and discussed.

4.3.2.1 Effect of WSS on EC Area

The PAEC area exposed to LSL, MSL, NZMSL and LCRD flow conditions for 10 hours, as well as for cells in static conditions, were measured, and analyzed with the results presented in Figure 4-6. Although an increasing pattern (with respect to the static condition) is observed in all of the flow conditions, no significant difference was observed between the static case and three of the flow conditions including the MSL, NZMSL and LCRD ($p>0.05$). However, a significant increase in the area was observed when the ECs were exposed to LSL flow compared with the static control (2,739±207 μm^2 vs. 1,587±128 μm^2, respectively, $p<0.0001$). Also ECs exposed to LSL flow had a significantly larger area when compared to the ECs subjected to the MSL, NZMSL and LCRD flow conditions (2,739±207 μm^2 vs. 1,728±269 μm^2, 1,871±316 μm^2 and 1,813±41 μm^2, respectively, $p<0.01$). The significant area increase of the ECs exposed to a low WSS LSL flow is evidence of the robust and sensitive EC mechanotransduction. The same pattern is reported by Vozzi *et al.* [26] where the eccentricity (defined in the introduction section of this chapter) was increased from 0.4 (for static conditions) to 0.95 when the ECs were exposed to WSS as low as 1.05 dyne/cm^2 (comparable to LSL flow).

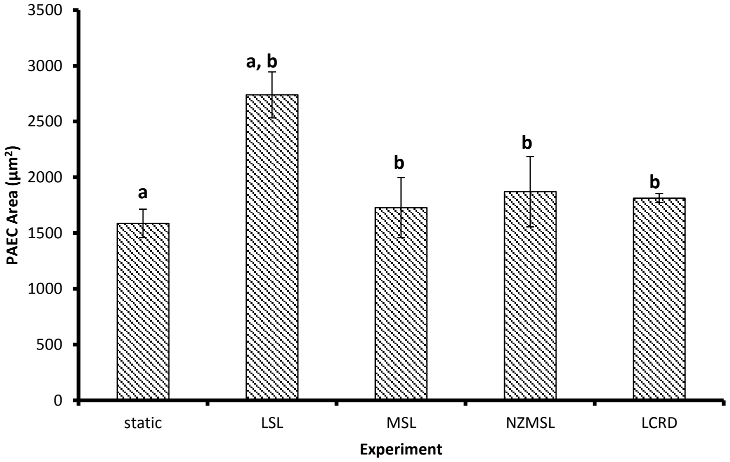

Figure 4-6 Bar graph illustrating the PAEC area (µm^2) variation between the static and the flow treated conditions (LSL, MSL, NZMSL and LCRD). A significant area decreased was observed in LSL flow conditions compared to the static control (a, p<0.0001). The PAEC area when exposed to LSL was also significantly higher than the other three flow treated conditions (b, p<0.01). n=3 and N=100

4.3.2.2 Effect of WSS on EC Perimeter

The changes in perimeter seen when PAECs were subjected to the LSL, MSL, NZMSL or LCRD flows, as well as for static conditions, are illustrated in Figure 4-7. These results did not show any statistically significant difference (p>0.05) between any of the four flows (LSL, MSL, NZMSL and LCRD). However, a significant perimeter increase was observed between the static and the LSL flow cases (172±14 µm vs. 235±5 µm, respectively, p<0.05), as well as between the static and the MSL flow (P=223±9 µm, p<0.05). These results also show that, regardless of the type of the mechanical force on the ECs, whether steady uni-directional (LSL and MSL), pulsatile uni-directional (LCRD) or pulsatile reversing (NZMSL), the EC perimeter increases compared to the static control which could be an indication of EC cytoskeletal structure re-localization. A significant perimeter increase by cell exposure to a low magnitude steady WSS (i.e., LSL) may be explained by an insufficient magnitude of shear stress being produced by this type of flow, which is nevertheless large enough to start disassembling the cytoskeletal bonds (the F-actin organization for all cases will be presented and discussed in detail). The NZMLS flow is similar to that found in an athero-prone flow regime (i.e., low and reversing WSS [29]). However, the reversing WSS may be acting as a continuous tension/contraction load on the cell which could be the main factor in the insignificant perimeter increase compared to the LSL flow.

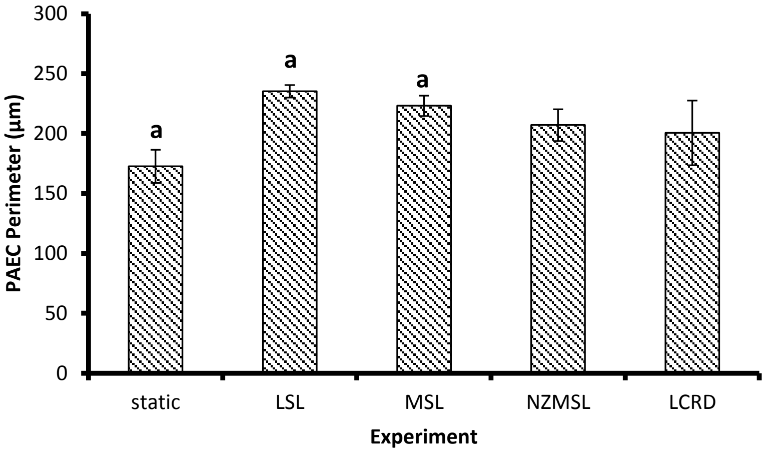

Figure 4-7 Bar graph illustrating the PAEC perimeter (µm) variation between the static and the flow treated conditions (LSL, MSL, NZMSL and LCRD). A significant increase was observed between the perimeter of the samples treated with the LSL and MSL flow conditions when compared with the static control (a, $p<0.05$). n=3 and N=100

4.3.2.3 Effect of WSS on EC Angle of Orientation

Figure 4-8 illustrates the histograms of the distribution of PAEC angle of orientation with the flow direction (θ_o, in the 10° increments) for the static control, as well as for the LSL, MSL, NZMSL and LCRD flow conditions. The occurrence frequency was normalized (relative frequency in %) by the total number of cells. The higher the relative frequency, the larger the number of cells oriented in that direction. These distribution histograms are also representative of the one dimensionality of the flow over the endothelium model (i.e., uni-directional flow over the coverslip) since the angular distribution shows symmetry with respect to 0°. The ECs were distributed in every direction from $\theta_o = -90°$ to 90° in the static conditions, with a larger frequency at $\theta_o = \pm 40°$ (at a frequency of about 16%). The ECs exposed to LSL flow start elongating with the flow direction since the maximum angle of orientation reduces to about $\theta_o = \pm 30°$ with a corresponding relative frequency of about 17%. For the MSL flow case, the ECs elongate more with the flow direction ($\theta_o = \pm 20°$) where the relative frequency also increased to about 30%. For the case where the ECs were exposed to the reversing NZMSL flow, although the elongation process is initiated (θ_o = ±30°), the histogram shows a pattern similar to the static condition. LCRD flow is a non-reversing flow and has a similar pattern to that seen in the graphs illustrating the LSL and MSL flows. The maximum elongation for this flow (LCRD) occurred at θ_o = ±30° and the relative frequency (about 21%) is higher than for LSL flow (17%) but lower than the MSL flow (30%).

The histogram illustration method for cell angle of orientation has been reported in very few previous works [51-52], even though this method provides more detailed information for the assessment of how the cells are aligned with the flow and at what occurrence frequency. The present results show that the cell angle of orientation is proportional to the magnitude of the WSS where the MSL flow with the highest WSS causes more cells to be aligned with the flow. Farcas *et al.* [52] studied the cell orientation by application of steady WSS of 20 dyne/cm^2 in two types of in vitro 3D models and found that after 12 hours, the initially randomly orientated ECs at the start of the experiment were aligned at about θ_o=0° with highest frequencies occurring between $-30 < \theta_o < 30$, although one of the models showed better alignment. Hence, they used this method as an evaluation technique to see how well their model could replicate the *in vivo* flow conditions. The present results, also show that, in case of pulsatile flow, provided that there is a non-zero mean WSS, the elongation process is initiated. However, the larger the mean value and the amplitude of the pulse, the more the cells are aligned with the flow. These results agree well with the study by Peng *et al.* [51] where they showed that by cell exposure to pulsatile flows with different amplitude (all uni-directional with a mean WSS of 1.6 dyne/cm^2), the relative frequency increased with an increase in the pulsation amplitude.

The average angles of orientation, $<\theta_o>$, for the PAECs in static control conditions as well as exposed to the LSL, MSL, NZMSL and LCRD flow conditions are shown in Figure 4-9. A decreasing trend in the angle of orientation was found for all of the flow conditions compared to the static control, although a significant decrease in the angle of orientation was observed only between the ECs exposed to MSL and LCRD flow conditions compared to the static condition (16.9±4.6° and 29.9±3.9° vs. 51.5±8.1°, respectively, $p<0.001$). Also, the angle of orientation for the MSL and LCRD flow cases were significantly smaller than the LSL (39.2±4.6°, $p<0.05$) and NZMSL flow conditions (41.1±3.7°, $p<0.05$).

These results suggest that ECs start to align with the direction of the flow even with low WSS, although the angle of orientation and the rate at which this alignment occurs depend on the net forward direction WSS. Similar results are reported in the literature as well [51].

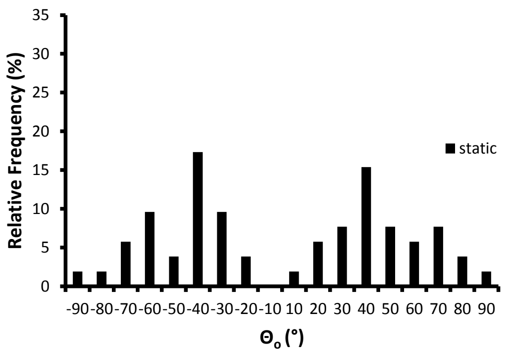

static

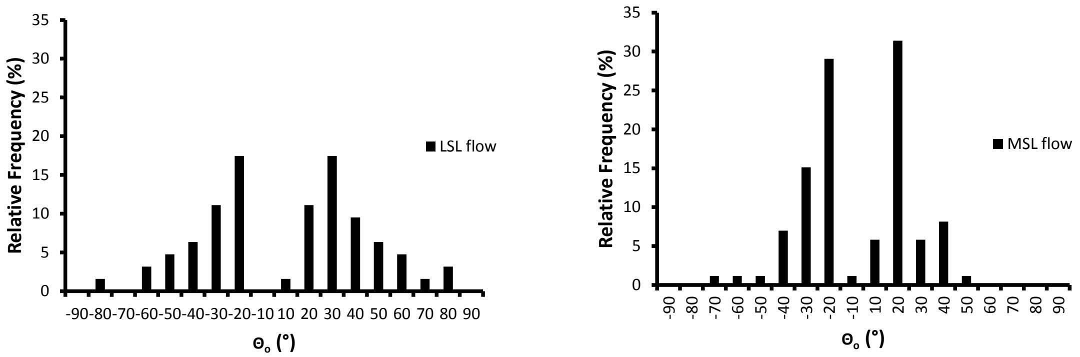

LSL **MSL**

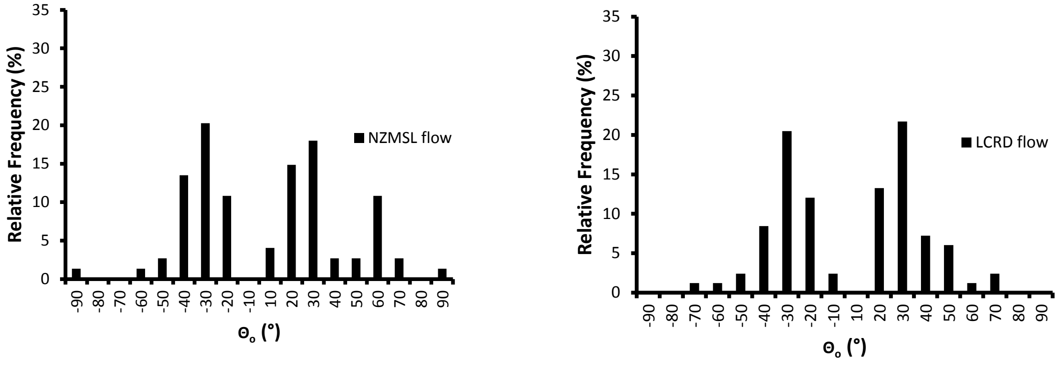

NZMSL **LCRD**

Figure 4-8 Histograms illustrating the distribution of PAEC angle of orientation with the flow direction, θ_o (in the 10° increments) for the static, LSL, MSL, NZMSL and LCRD conditions. n=3 and N=80

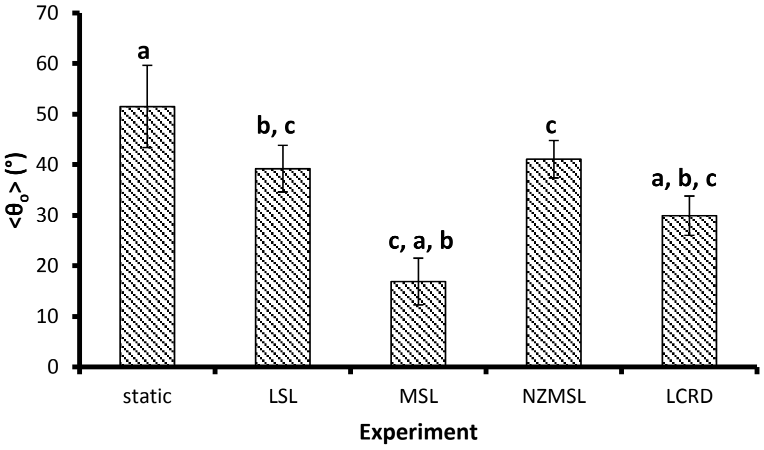

Figure 4-9 Average angles of orientation <θ_o> for the PAECs in static condition, as well as the LSL, MSL , NZMSL and LCRD flow conditions. A significant decrease was observed in the angle of orientation of the cells exposed to the MSL and LCRD flow conditions compared to the static condition (a, $p<0.001$). <θ_o> for the MSL and LCRD flow cases was significantly smaller than for the LSL (b, $p<0.05$) and the NZMSL (c, $p<0.05$) cases. n=3 and N=100

4.3.2.4 Effect of WSS on Shape Index (S.I.)

A significant decrease in S.I. was found (see Figure 4-10) when the LSL, MSL, NZMSL and LCRD flows, were compared with the static control case (0.57±0.03, 0.47±0.04, 0.64±0.04 and 0.60±0.03 vs. 0.73±0.03, respectively, $p<0.001$). The S.I. for the MSL flow was significantly smaller than the other three experimental conditions (i.e., LSL, NZMSL and LCRD, $p<0.01$). According to these findings, S.I. can be considered as a more flow-sensitive morphometric parameter for ECs compared to the cell area and perimeter (A_c and P_c, respectively) since even a low WSS level (e.g., LSL flow) caused a decreased difference between the flow experiment and the static control case. Smaller values of S.I. indicate more elongation with the flow direction.

Comparing the absolute value of S.I. for different types of ECs (even in the static condition) is not a suitable parameter; rather, the S.I. change (between the flow-subjected ECs and the corresponding control) conveys more information for comparison purposes. The difference reported for S.I. between different studies despite similar experimental facilities, is mainly due to the difference between the EC types (e.g., PAEC vs. BAEC), the flow quality (e.g., uniform flown regions), the staining technique [52] and the confluency of the cells [24]. Accurate quantification of the flow in terms of WSS and the uniformity of the flow over the coverslip is one of the main contributions of the present study. By precisely quantifying the flow, the bias arising from flow quality affecting the reported magnitude of WSS significantly decreases and, hence, the contribution of flow quality in reported S.I. values is eliminated, although the other-mentioned factors may still exist.

It has been widely accepted that ECs elongate under WSS and, hence, the S.I. decreases to values less than the corresponding static control. The present findings are in good agreement with previous work. For example, Dick *et al.* showed that applying 12.5 dyne/cm^2 WSS (similar to the MSL flow in the present study) to ECs, reduced the S.I. from 0.52 to 0.40 [18]. Farcas *et al.* showed that the S.I. for ECs exposed to 20 dyne/cm^2 for 8 hours reduced the S.I. from 0.63 to 0.45 in a tubular model [52]. Helmlinger *et al.* reported that the S.I. for ECs subjected to a non-reversing pulsatile WSS of 40±20 dyne/cm^2 was reduced to 0.60 (compared to the static S.I. of 0.80), whereas the reversing WSS of 20±40 dyne/cm^2 decreased the S.I. only to 0.68, with 8 hours flow treatment [22]. These findings suggest that reversing the flow has an adverse effect on EC elongation. In the current study, NZMSL, as a reversing flow with a very low net WSS, had the largest S.I. (smallest S.I. change compares to the static control) among all the other cases.

Helmlinger *et al.* also showed that the S.I. for a steady WSS of 40 or 60 dyne/cm^2 was lower (i.e., 0.55 and 0.50, respectively) than for a pulsatile case (S.I.= 0.60) with WSS of 40±20 dyne/cm^2 [22] (for comparison, the data extracted from previous work is represented in Figure 4-11). These findings suggest that pulsatile flow, although being uni-directional (similar to the LCRD flow in the current study), caused less elongation (larger S.I.) than a steady flow with a WSS comparable to the mean or maximum of the pulsatile flow.

The elongation of ECs with pulsatile flow is not only correlated with the pulse mean

WSS but also dependent on the reversing/non-reversing pattern of the flow, since a pulsatile flow with no net forward direction causes almost no change in S.I. compared to the static control [22].

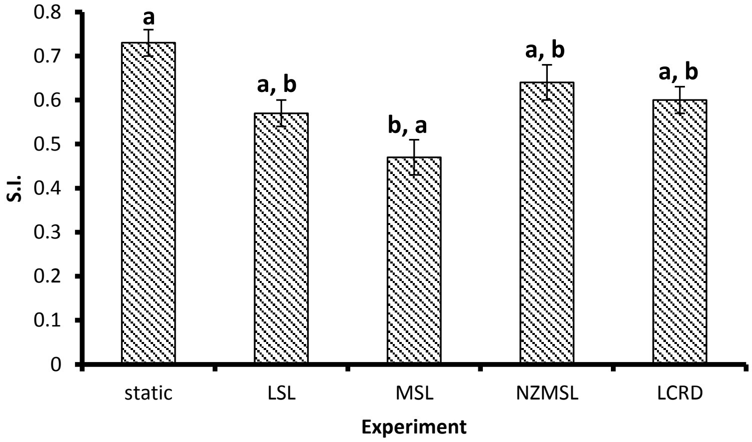

Figure 4-10 The S.I. for PAEC in static, as well as the LSL, MSL, NZMSL and LCRD flow conditions. The S.I. ranges between 0 and 1, the former describing a straight line whereas the latter corresponds to a circle. A significant decrease was found for all four flow experiments when compared with the static control (a, p<0.001). The S.I. for the MSL flow was significantly smaller than for the other three (LSL, NZMSL and LCRD) experiments (b, p<0.01). n=3 and N=100

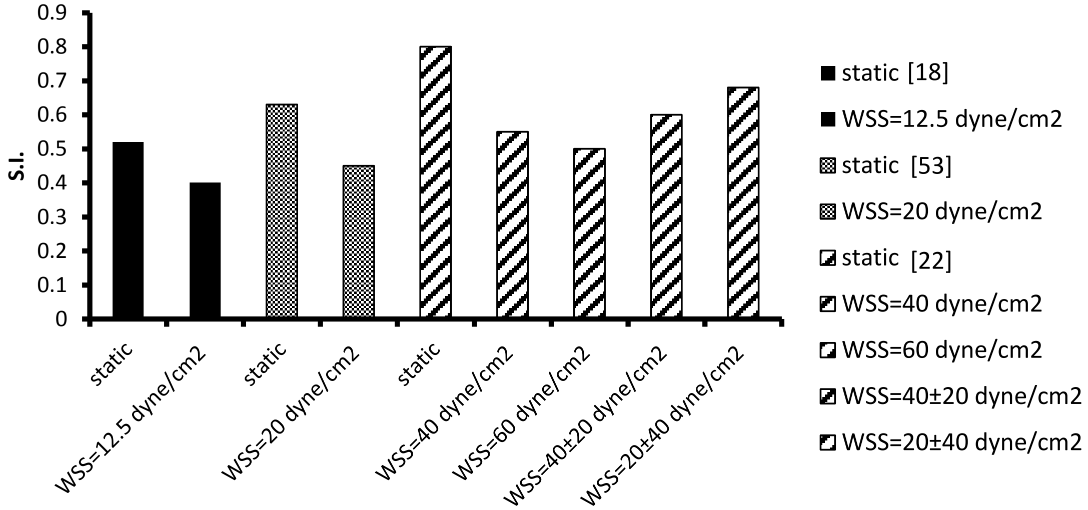

Figure 4-11 The S.I. for the static control as well as for the flow conditions reported in previous work. The bars with the similar pattern represent the results of the same study.

4.3.3 Effect of WSS on F-actin Bundles

Representative images showing the F-actin bundles for ECs in static conditions as well as LSL, MSL, NZMSL and LCRD flow conditions are depicted in Figure 4-12 (A, E, I, M and Q). To further analyze the actin alignment with the imposed flow-induced WSS, the quantification method described in section 4.2.7.2 was employed. Representative histograms of the relative pixel intensity, indicator of the actin alignment with the flow direction, for PAECs exposed to the LSL, MSL, NZMSL and LCRD flows are presented in Figure 4-13 (also see Figure 4-4-E for comparison with the static control). The higher the peak in the histogram, the more aligned are the actin bundles in that 10° band (i.e., the band ranging from 0 to10°). For an ideal ROI with fully aligned actin filaments, all the values except 10° and 180° must be zero. An unusual peak is detectable for most of the histograms at 100° (angles between 90°-100°) which has been mentioned in the literature as the noise due to the image edge effects [32]. The A.I. (i.e., a measure of the actin filament alignment with the flow direction) for the static control as well as the four flow cases are presented in Figure 4-14. The A.I. corresponding to the LSL, MSL, NZMSL and LCRD flows were significantly increased compared to the static control

(0.149±0.045, 0.214±0.008, 0.153±0.015 and 0.211±0.008 vs. 0.070±0.014, respectively, $p<0.01$). The A.I for the MSL and LCRD flows were significantly higher than for the LSL flow ($p<0.05$), whilst the A.I. for the NZMSL flow case was significantly lower than for the MSL flow ($p<0.05$). These results show that the A.I. was directly proportional to the magnitude of the WSS applied on the ECs; the higher the applied WSS, the higher the A.I. value.

The EC under static control conditions (Figure 4-12-A) have short and thin randomly oriented F-actin filaments with denser peripheral F-actin bands around the cell edge. The histogram illustration of the actin alignment for static control (Figure 4-4-E) also shows a somewhat even distribution of the actin bundles in random directions (relative pixel intensities ranging from about 2-7%) with a higher frequency of filaments in the 70°-100° bands. The actin structure seen here is similar to what has been reported in the literature where ECs under static conditions are described as having a diffuse F-actin distribution exhibiting "star-like" configurations [18, 22]. The ECs exposed to the LSL flow (Figure 4-12-E) had aligned F-actin within each individual cell, although each cell had an overall random F-actin bundle polarity, not being predominantly in the flow direction. The peripheral actin band also disappeared in the ECs subjected to the LSL flow. In contrast, the actin cytoskeleton in those ECs subjected to the MSL flow (Figure 4-12-I) was reorganized such that the filaments became aligned with the flow direction with thicker and denser actin bundles across the entire cell. The histogram illustration of the actin bundle alignment (Figure 4-13) also shows that the ECs subjected to the LSL flow started to align their actin filaments although the alignment was uniform over the first 60° band followed by a decreasing pattern until 120° (-60°), whereas, for the MSL case, the actin filaments were more symmetrically aligned about the 90° (V-shape) with the highest alignment (relative pixel intensity of 10-12%) being in the 0-20° and 160-180° (0 to -20°) directions. A similar remodeling pattern of ECs exposed to a MSL flow is reported in the literature where the F-actin bundles of ECs subjected to 15 [24], 12.5 [18] and 20 [53] dyne/cm^2 of WSS were aligned in the flow direction and were thicker than the static control. The NZMSL flow (Figure 4-12-M) initiated the F-actin remodeling, although the thickness of the actin bundles appeared to be similar to the static control cases, whereas their length increased. Denser actin bundles were observed in regions close to the apex or around the edges of the cells. The histogram illustration of the actin bundles alignment (Figure 4-13) for the NZMSL flow (A.I. = 0.153±0.015) showed more and less alignment compared to the LSL and MSL flow cases (A.I. = 0.149±0.045 and 0.214±0.008), respectively. Helmlinger *et al.* [22] reported that the F-actin cytoskeleton of ECs subjected to a reversing WSS of 10±15 dyne/cm^2 underwent the similar remodeling pattern (i.e., long stress fibres, aligned with the flow direction) as to the steady flow case, although their stress fibres appeared somewhat thicker. Comparing the F-actin distribution for the NZMSL (reversing flow) with the LSL (i.e., a comparable steady flow) yields similar results, where actin alignment occurred in both cases, although the LSL flow resulted in thicker actin bundles.

The EC F-actin remodeling pattern when exposed to the LCRD flow (Figure 4-12-Q), which is a non-reversing physiological pulsatile flow, was similar to the MSL flow with thick, dense and aligned actin bundles across the entire cell, although the actin bundles in those ECs exposed to the MSL flow were more aligned with the flow direction, thicker and denser which was due to a a higher level of applied WSS. The LCRD flow exerted a similar pattern on the actin bundle alignment (V-shape) as the MSL flow (as seen by comparing the histograms corresponding to these two flow conditions in Figure 4-13), although the alignment of the actin filaments in the first 30° band was more uniform (≈10%). The current results confirm the reported finding by Voyvodic *et al.* [54], where comparison between the actin bundles in ECs exposed to both steady (WSS of 20 dyne/cm^2) and non-reversing physiological flows (mean WSS of 20 dyne/cm^2) showed an increased formation of actin stress fibres in the presence of steady flow.

A.I. has been defined differently in previous studies such that no universal definition has been established. For example, Van der Meer *et al.* [33] defined the A.I. as the sum of the intensities in the first 30° peak. Although this definition provides a quantitative value for the alignment of the actin bundles, it does not consider the alignment of those bundles in the last bands (e.g., the 180° band also represents the -10° band). For comparison, the A.I. values for the present cell experiments were also calculated using their definition (Figure 4-14). In all cases, the A.I. calculated by Van der Meer *et al.'s* definition resulted in higher values than those defined in the present work. However, the A.I. for the LCRD case was found to be greater than for the MSL case, which is contradictory to the current A.I. results, where comparing the angle of orientation, as well as the F-actin filament alignment histograms and visual observations (Figure 4-12), shows greater alignment in the MSL flow case. From this comparison of methods, the current A.I. definition seems to be more appropriate for quantifying the flow effects on the actin filaments.

In this study, in order to analyze and interpret the effects of the flow on EC actin bundles, the visual observations were combined with the quantitative analysis through 2D FFT and consequently the A.I. was defined for each case. The discussion above showed that both visual and quantitative results are consistent, although quantitative methods provide more detailed information with regards to the actin distribution within a sample. This approach for the actin analysis has never been reported anywhere else and is considered as one of the major contributions of the present work and the results may shed light into the current knowledge of EC mechanotransduction in response to flow. For example, the correlation between the cell vs. actin alignment might be a signaling pathway in ECs modulated by WSS that can be investigated through further experimentation to gain better insight into cellular events in mechanotransduction.

The results from this section suggest that EC actin bundle alignment with the flow direction is initiated when the cells are exposed to all of the four flow cases studied here. As an example, the analysis results revealed that even in the vicinity of a NZMSL flow (i.e., representative of athero-prone flow [9] which may occur just downstream of an atherosclerotic lesion [29, 44, 55]), the actin filaments start to align with the flow direction. However, the reversing flow pattern, as well as the low mean and low peak amplitude of the WSS in this flow condition, did not allow for sufficient alignment of actin (such as in the well-aligned pattern seen in the MSL flow).

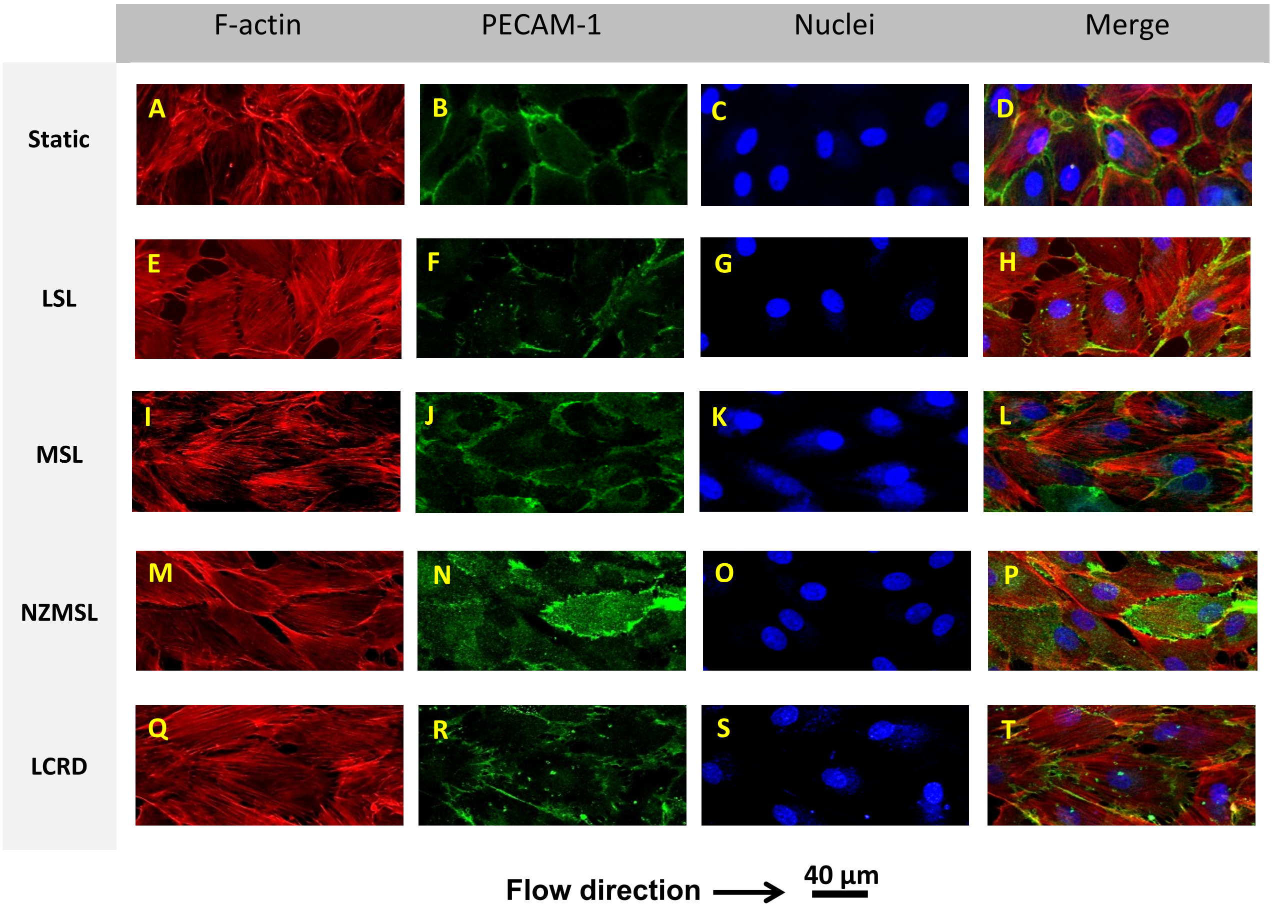

Figure 4-12 The WSS remodels PAEC F-actin bundles and PECAM-1 localization. Immunofluorescence staining of F-actin bundles with Phalloidin (red), PECAM-1 with mouse anti-pig CD31 (green) and nuclei (blue) are presented. The images represent the static control (A-D) as well as LSL (E-H), MSL (I-L), NZMSL (M-P) and LCRD (Q-T) flow conditions. Localization of PECAM-1 is shown in images B, F, J, N and R. Nuclei staining is seen in images C, G, K, O and S. Also, F-actin, PECAM-1 and nuclei merge images are presented in images D, H, L, P, T (see appendix 3 for low magnification images).

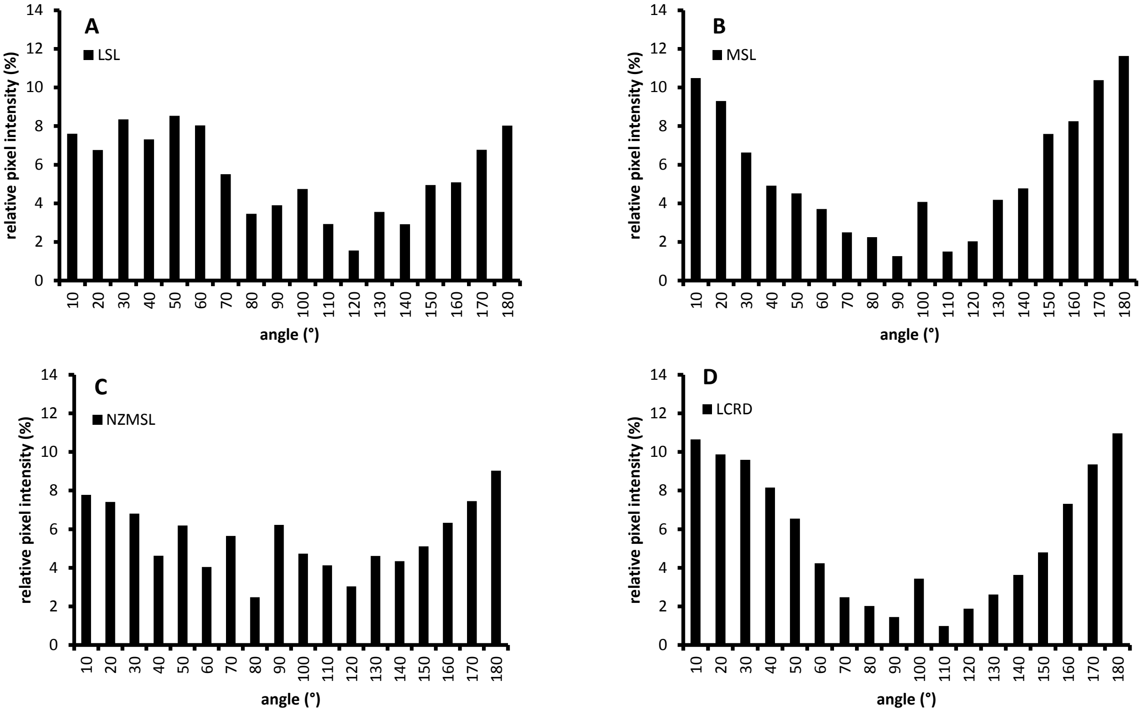

Figure 4-13 Representative histograms illustrating the alignment of the actin filaments using a 2D FFT method for PAECs subjected to LSL (A), MSL (B), NZMSL (C) and LCRD (D) flows. The higher the peak in the histogram, the more aligned are the actin filaments in that 10° band. For comparison with the static control see Figure 4-4-E.

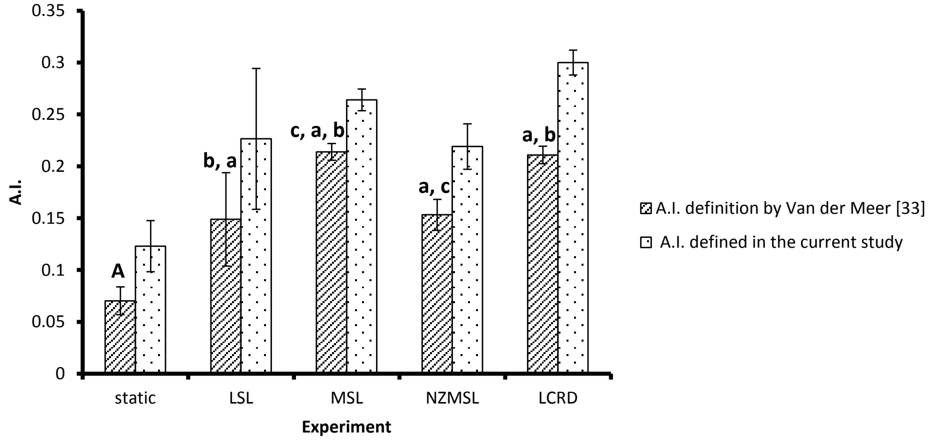

Figure 4-14 The effect of WSS on the A.I. for all cases. A significant increase was found between the static and all the flow treated conditions (a, $p<0.01$). Also, the results showed a significant decrease when the A.I. for the MSL and LCRD flow treated ECs was compared with the LSL flow conditions (b, $p<0.05$) as well as a significant decrease when the A.I. for the NZMSL flow condition was compared with the MSL flow condition (c, $p<0.05$). For comparison, the A.I. has also been calculated as defined by Van der Meer *et al.* [33] (dotted pattern). n=3 and N=100

4.3.3.1 Is there a Correlation between the F-actin and EC Alignment with the Flow Direction?

The PAEC angle of orientation vs. A.I. for all the cases is presented in Figure 4-15. An overall decreasing linear trend is seen with increasing A.I. suggesting that the larger the A.I., the more the ECs are aligned with the flow direction. Since the uncertainties in determination of the A.I. as well as the angle of orientation were found to be 21 and 27% (95% confidence interval), respectively, the deviations seen for the MSL and LCRD flow cases, from the linear fit are within these uncertainties.

The correlation between the EC morphology and F-actin alignment with the flow has been qualitatively mentioned in some of the previous work [9, 13]. However, to the best of the author's knowledge, the mathematical correlation between the cell alignment vs. F-actin alignment is presented for the first time in the present work (i.e., one of the novelties of the present work). What can be concluded from the present results, together with previously reported evidence, is that the EC angle of orientation (which may be considered as a macroscopic orientation) and the F-actin orientation (which may be considered as a microscopic orientation) are correlated and that both occur under the same flow conditions.

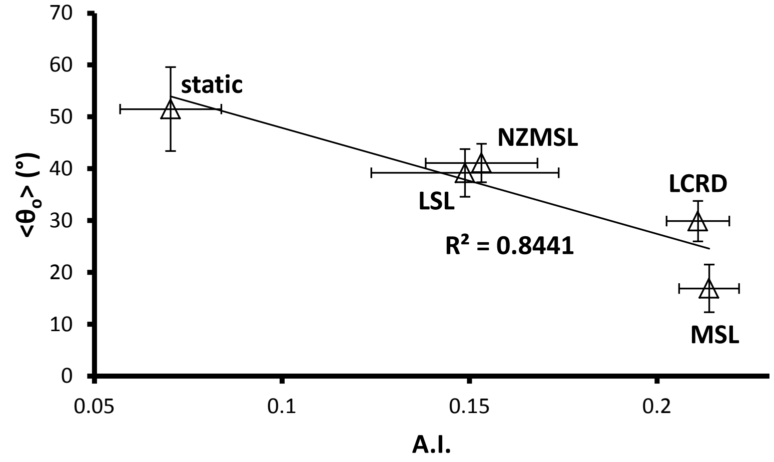

Figure 4-15 <θ_o> vs. A.I. for the static control as well as the LSL, MSL, NZMSL and LCRD flow conditions. The linear regression method depicts an overall decreasing trend with the increasing A.I. suggesting that the larger the A.I. the more the ECs are aligned.

4.3.4 Effect of WSS on PECAM-1 Morphology

Representative images of the PECAM-1 localization in PAECs for all the case are presented in Figure 4-12 (B, F, J, N and R). PECAM-1 was localized as a peripheral band at the borders of adjacent cells (Figure 4-12-B) under static conditions as reported in the literature [56]. The variable thickness of the PECAM-1 at different sites is due to the variable overlap thickness of the ECs at the cell-cell junctions.

Figure 4-12-F shows staining of PECAM-1 for the LSL case. As can be seen, the circumferential PECAM-1 band is not uniform around the edge of the cell and the continuous PECAM-1 band (found in static control) is no longer seen. Figure 4-12-J represents the PECAM-1 localization for the MSL case. The peripheral PECAM-1 is almost conserved and it seems to be thicker than in the static case which, may be due to the change of the overlapping edge at the cell-cell junctions. Also, some internal PECAM-1 (which is confirmed by the presence of hollow elliptical spaces inside the cell, indicating the nuclei location within the cell) is observed in this figure. Similarly Chiu *et al.* reported that the peripheral PECAM-1 distribution in ECs subjected to 12 dyne/cm^2 of WSS for 24 hours was the same as the static control [42].

Those ECs subjected to the reciprocating (NZMSL) flow lost most of the peripheral PECAM-1 band and, in turn, had the largest amount of internal PECAM-1. PECAM-1 localization in the LCRD case (Figure 4-12-R) was similar to the MSL case where the peripheral PECAM-1 band is preserved. However, less internal PECAM-1 was observed in the LCRD case compared to the MSL flow. Since a major constituent of the EC cell-cell contact is PECAM-1 [36], the results presented here suggest, that for both the MSL and LCRD flow conditions, the cell-cell junctions were conserved whereas the LSL and NZMSL flows caused the cell-cell junction to be partially/fully corrupted and, hence, the EC cell-cell junctions were not stably maintained, which could affect vascular permeability (a factor in the initiation of atherosclerosis [27]). These observations on the flow effects on PECAM-1 morphology are not reported in any other previous work and, hence, can be considered significant for linking the role of this protein in mechanotransduction.

The P.R.D. (as a quantitative measure for the peripheral PECAM-1density) variation measured for each flow case is shown in Figure 4-16. These results suggest that fluid-induced wall shear stress (WSS) modulates the localization of PECAM-1. PECAM-1 has been used to verify the confluency of the ECs since it is localized in the EC junctions [57] and, hence, it can be an indicator of cell-cell junctions (cell spreading). The current results demonstrate that for all of the samples subjected to the low WSS (LSL) or reciprocating low WSS (NZMSL flow), the peripheral PECAM-1 were partially or completely lost. This loss cannot be due to the magnitude of the WSS (or the consequent hemodynamic shear force) on this adhesion protein since the MSL flow (exerting almost ten times greater WSS on the ECs than LSL flow) or LCRD (with a mean WSS of about five times greater than LSL flow) almost completely preserved the PECAM-1 localization at the cell-cell sites. The EC junctional mechanosensory complex consists of VE-cadherin, PECAM-1 and VEGFR-2 [58]. A recent study by Conway *et al.* [59] suggests that cells actively respond to the extracellular tension by modulating that tension across junctional proteins. It is known that PECAM-1 also plays a crucial role in the activation of NFκB and Akt pathways and inflammatory cell accumulation during vascular remodeling [41, 60]. Although no literature was found on the localization of PECAM-1 by exposing EC to various flow regimes, the results observed here (e.g., the partial loss of cell-cell contact under athero-prone LSL and NZMSL flow conditions), could be part of the transient response (mechanotransduction) of the cells to the flow-induced shear stress. In this scenario, the internalization of the PECAM-1 in the presence of LSL and NZMSL flows can be interpreted as a signaling pathway (with intracellular molecules) for an inflammatory response. The 10 hour duration WSS exposure time in this study was significantly beneficial since the internalization of junctional PECAM-1 may be a transient mechanosensory response of cells to athero-prone flow and, hence, these results provide valuable insight for further investigation of the mechanosensory events occurring to the PECAM-1 under mechanical stimuli.

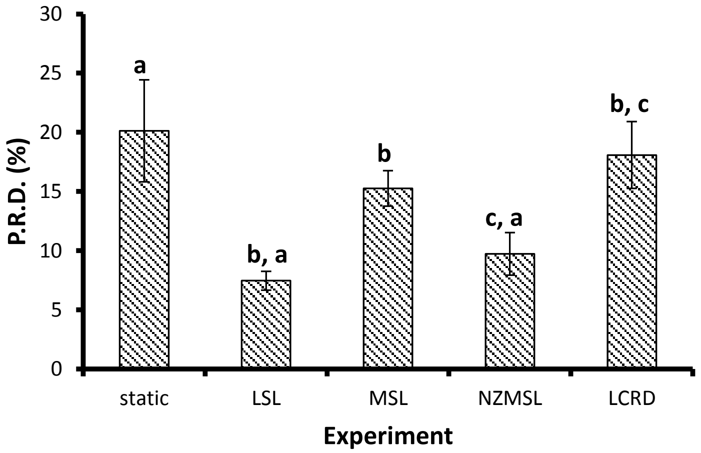

Figure 4-16 Fluid-induced shear stress (WSS) modulates distribution of PECAM-1. The P.R.D. was defined as a measure of peripheral PECAM-1. A significant decrease in the P.R.D. was seen for the LSL and NZMSL flow treated ECs when compared to the static control (a, $p<0.01$). These results also depict a significant increase in the P.R.D. for the MSL and LCRD flow treated ECs when compared to the LSL flow condition (b, $p<0.05$). Similarly, a significant increase was observed in the results of the LCRD flow conditions when compared with the NZMSL flow case (c, $p<0.05$). n=3 and N=100

4.4 Conclusions

In this *in vitro* study, the effects of fluid-induced shear stress (WSS) on PAECs were investigated. The focus of this study was on the morphological modulation (a well-accepted indicator of a healthy vs. dysfunctional ECs [18, 21]), F-actin bundle arrangement and PECAM-1 morphological re-distribution while exposed to four different types of flow regime each representing a different hemodynamic stress on the ECs. The current study is the only work among other related studies in this area that has applied four WSS profiles to ECs using the same experimental facility for comparison of the EC responses to those flows. For each flow case, the hemodynamic parameters (e.g., Reynolds number and Womersley number) were precisely quantified and found to be within the physiological range, thereby minimizing the bias in the results due to irrelevant experimental conditions. The uniformity of the flow over the ECs was also precisely quantified to ensure that the analyzed ECs were all subjected to uniform conditions. These hemodynamic quantifications, flow uniformity in particular, have been under-reported in most of the previous work.

The results show that although the cell area and perimeter were modulated by WSS exposure, the S.I. may be considered as being a more useful morphological parameter by which to differentiate between the various loading conditions. Although in many previous studies, the S.I. and angle of orientation have been applied as morphometric parameters, no study was found that investigated the efficiency of those morphological parameters in a set of different experiments.

The S.I. decreased for all of the flow exposed samples despite a very low level of WSS for some cases, such as LSL flow. It has also been concluded that the S.I. changes are correlated with the reversing/uni-directional nature of the flow as well as with the mean and peak amplitude of the pulse for the pulsatile flow conditions (confirming previous studies).

The angle of orientation of the ECs was also quantified and investigated by histograms demonstrating the relative frequency of EC orientation for every 10° band and it was shown that, in all of the flow cases, the cells started to align with the flow. However, with increased WSS, the frequency of the cells in the bands closer to zero increased (i.e., the higher the WSS, the more the cells are aligned with the flow). Also, the symmetry seen in these histograms was used as evidence of there being no lateral flow across the channel span. This method is not argued/discussed in any other study and yet it would seem to be crucial in any study that aims to investigate the effects of the flow in a single direction.

Visual and quantitative 2D FFT-based analysis of F-actin revealed that, regardless of the flow type, the F-actin bundles rearranged themselves to gain a certain polarity within a single cell, something not previously reported. The 2D FFT technique has been gaining popularity in fibre-directionality analysis and yet no prior study was found that applied this approach as a comparative tool to analyze the flow effects on EC F-actin bundles for various flow conditions. An A.I. was defined, based on the findings from the FFT-analysis, and it was shown to offer a better comparative tool than another definition previously reported in the literature. The higher the magnitude of the WSS, the more the cells had their F-actin aligned with the flow direction which resulted in a uniform distribution within the entire sample. For the first time, a mathematical linear correlation between the cell vs. F-actin alignment was proposed based on the findings of the current study.

PECAM-1 morphology (localization) was only shown in static and moderate-level WSS in previous studies. The current results shows that the peripheral PECAM-1 band seen in static control was conserved in the MSL and LCRD cases, whereas both the LSL and NZMSL cases resulted in partial/full peripheral PECAM-1 band loss. A P.R.D. was defined to account for the peripheral PECAM-1 band area and was shown to be a very suitable discriminating parameter between all the cases. An interesting observation about PECAM-1 was a significant internalization and/or increased internal production of this protein by those ECs exposed to athero-prone flows (LSL and NZMSL). Since PECAM-1 is characterized as having a role in inflammation in vascular biology, this observation might shed light on the mechanosensory pathway that occurs by the WSS acting on PECAM-1 stress sensors. However, more experimentation, such as investigation of the up-/down- regulation of VCAM-1 is required. Up-regulation of VCAM-1 in ECs exposed to LSL and NZMSL flow conditions would provide strong proof for the observed mechanosensory events found in the current research study.

4.5 References

[1] "World Health Organization (WHO)," [Online]. Available: http://www.who.int/mediacentre/factsheets/fs317/en/. [Accessed 3 February 2015].

[2] J. A. Berliner, M. Navab, A. M. Fogelman, J. S. Frank, L. L. Demer, P. Edwards, A. D. Watson and A. J. Lusis, "Atherosclerosis: Basic Mechanisms, Oxidation, Inflammation, and Genetics," *Circ.,* vol. 91, pp. 2488-2496, 1995.

[3] R. Ross, "Atherosclerosis: An Inflammatory Disease," *New Engl. J. Med.,* vol. 340, no. 2, pp. 115-126, 1999.

[4] R. Ross, "The Pathogenesis of Atherosclerosis: a Perspective for the 1990s,"

Naturue, vol. 362, pp. 801 - 809, 1993.

[5] J. Ferrières, "Effects on Coronary Atherosclerosis by Targeting Low-density Lipoprotein Cholesterol with Statins," *Am J Cardiovasc Drugs,* vol. 9, no. 2, pp. 109-115, 2009 .

[6] S. F. Kemeny, D. S. Figueroa and A. M. Clyne, "Hypo- and Hyperglycemia Impair Endothelial Cell Actin Alignment and Nitric Oxide Synthase activation in Response to Shear Stress," *PLOS ONE,* vol. 8, no. 6, p. e66176, 2013.

[7] S. Estrada, G. A. Giridharan, M. Nguyen, T. J. Roussel, M. Shakeri, V. Parichehreh, S. D. Prabhu and P. Sethu, "Endothelial Cell Culture Model for Replication of Physiological Profiles," *Anal. Chem.,* vol. 83, pp. 3170-3177, 2011.

[8] Q. Guo, "The Effect of Biomechanical and Biochemical Factors on Endothelial Cells: Relevance to Atherosclerosis," *PhD theis,* University of Western Ontario, Canada, 2011.

[9] J. J. Chiu and S. Chien, "Effects of Disturbed Flow on Vascular Endothelium; Pathophysiological basis and clinical perspectives," *Physiol Rev,* vol. 91, pp. 327-387, 2011.

[10] P. F. Davies, "Flow-Mediated Endothelial Mechanotransduction," *Physiol. Rev.,* vol. 75, no. 3, pp. 519-560, 1995.

[11] D. N. Ku, D. P. Giddens, C. K. Zarins and S. Glagov, "Pulsatile Flow and Atherosclerosis in the Human Carotid Bifurcation; Positive Correlation Between Plaque Location and Low Oscillating Shear Stress," *Throm. Vasc. Biol. ,* vol. 5, pp. 293-302, 1985.

[12] C. F. Dewey and S. R. Bussolari, "The Dynamic Response of Vascular Endothelial Cells to Fluid Shear Stress," *J. Biomech. Eng.,* vol. 103, pp. 177-185, 1981.

[13] R. M. Nerem, M. J. Levesque and J. F. Cornhill, "Vascular Endothelial Morphology as an Indicator of the Pattern of Blood Flow," *J. Biomech. Eng.,* vol. 103, pp. 172-176, 1981.

[14] C. F. Dewey, "Effects of Fluid Flow on Living Vascular Cells," *J. Biomech. Eng.,* vol. 106, pp. 31-35, 1984.

[15] B. R. Blackman, K. a Barbee and L. E. Thibault, "In Vitro Cell Shearing Device to Investigate the Dynamic Response of Cells in a Controlled Hydrodynamic Environment," *Ann. Biomed. Eng.,* vol. 28, no. 4, pp. 363-372, 2000.

[16] P. F. Davies, M. A. Reidy, T. B. Goode and D. Bowyer, "Scanning Electron Microscopy in the Elevation of Endothelial Integrity of the Fatty Lesion in Atherosclerosis," *Atherosclerosis,* vol. 25, p. 125–130, 1976.

[17] J. T. Flaherty, J. E. Pierce, V. J. Ferrans, D. J. Patel, W. K. Tucker and D. Fry, "Endothelial Nuclear Patterns in the Canine Arterial Tree with a Reference to Hemodynamic Events," *Circ. Res.,* vol. 30, p. 23–33, 1972.

[18] M. Dick, P. Joank and R. L. Leask, "Statin Therapy Influences Endothelial Cell Morphology and F-actin Cytoskeleton Structure When Exposed to Static and Laminar Shear Stress Conditions," *Life Sci.,* vol. 92, pp. 859-865, 2013.

[19] A. Dardik, L. Chen, J. Frattini and F. Aziz, "Differential Effects of Orbital and Laminar Shear Stress on Endothelial Cells," *J. Vasc. Surg.,* vol. 41, no. 5, pp. 869-880, 2005.

[20] P. F. Davies, A. Remuzzitt, E. J. Gordon, C. F. Dewey and M. A. Gimbrone, "Turbulent Flow Shear Stress Induces Vascular Enothelial Cell Turn Over in Vitro," *Proc. Natl. Acad. Sci.,* vol. 83, pp. 2114-2117, 1986.

[21] M. J. Levesque and R. M. Nerem, "The Elongation and Orientation of Cultured Endothelail Cells in Response to Shear Stress," *J. Biomech. Eng.,* vol. 170, pp. 341-347, 1985.

[22] G. Helmlinger, R. V. Geiger, S. Schreck and R. M. Nerem, "Effects of Pulsatile Flow on Cultured Vascular Endothelial Cell Morphology," *J. Biomech. Eng.,* vol. 113, pp. 123-131, 1991.

[23] M. J. Levesque, E. A. Sprague , C. J. Schwartz and R. M. Nerem, "The Influence of Shear Stress on Cultured Vascular Endothelial Cells: The Stress Response of an Anchorage-Dependent Mammalian Cell," *Biotech. Prog.,* vol. 5, no. 1, pp. 1-8, 1989.

[24] C. G. Galbraith, R. Skalak and S. Chien, "Shear Stress Induces Spatial Reorganization of the Endothelial Cell Cytoskeleton," *Cell Motil. Cytoskel.,* vol. 40, pp. 317-330, 1998.

[25] H.-J. Schnittler, R. P. Franke, U. Akbay, C. Mrowietz and D. Drenckhahn, "Improved In Vitro Rheological System for Studying the effect of Fluid Shear Stress on Cultured Cells," *Am. J. Physiol.,* vol. 265, pp. C289-C298, 1993.

[26] F. Vozzi, F. Bianchi, A. Ahluwali and C. Domenici, "Hydrostatic Pressure and Shear Stress Affect Endothelin-1 and Nitric Oxide Release by Endothelial Cells in Bioreactors," *Biotechnol. J.,* vol. 9, pp. 146-154, 2014.

[27] M. B. Simmers, A. W. Pryor and B. R. Blackman, "Arterial Shear Stress Regulated Endothelail Cell-directed Migration, Polarity and Morphology," *Am. J. Physiol. Heart Circ. Physiol.,* vol. 293, pp. H1937-H1946, 2007.

[28] C. Wang, H. Lu and M. A. Schwartz, "A Novel In Vitro Flow System for Changing Flow Direction on Endothelial Cells," *J. Biomech.,* vol. 45, pp. 1212-1218, 2012.

[29] S. Chien, "Mechanotransduction and Endothelial Cell Homeostasis; the Wisdom of the Cell," *Am. J. Physiol. Heart Circ. Physiol.,* vol. 292, pp. 1209-1224, 2007.

[30] W. M. Petroll, H. D. Cavanagh, P. Barry, P. Andrews and J. V. Jester, "Quantitative Analysis of Stress Fibre Orientation During Corneal Wound Contraction," *J. Cell Sci.,* vol. 104, pp. 353-363, 1993.

[31] M. Yoshighi, E. B. Clark and H. J. Yost, "Quantification of Stretch-Induced Cytoskeletal Remodeling in Vascular Endothelial Cells by Image Processing," *Cytom. Part A.,* vol. 55, no. 2, pp. 109-118, 2003.

[32] C. E. Ayres, B. Shekharjha, H. Meredith, J. R. Bowman, G. R. Bowlin and S. C. Henderson, "Measuring Fibre Alignment in Electrospun Scaffolds: A User's Guide to the 2D Fast Fourier Transfrom Approach," *J. Biomater. Sci.,* vol. 19, no. 5, pp. 603-621, 2008.

[33] A. D. van der Meel, A. A. Poot, J. Feijen and I. Vermes, "Analyzing Shear-Induced Alignmnet of Actin Filaments in Endothelial Cells with a Microfluid Assay," *Biomicrofluidics,* vol. 4, pp. 011103-1-5, 2010.

[34] E. S. Lai, N. F. Huang, J. P. Cooke and G. G. Fuller, "Aligned Nanofibrillar Collagen Regulated Endothelial Organization and Migration," *Regen. Med.,* vol. 7, no. 5, pp. 649-661, 2012.

[35] M. Cetera, G. R. Ramirez-San Juan, P. W. Oakes, L. Lewellyn, M. J. Fairchild, G. Tanentzaof, M. L. Gardel and S. Horne-Bardovinac, "Epithelial Rotation Promotes the Global Alignmnet of Contractile Actin Bundles During Drosophila Egg Chamber Elongation," *Nat. Commun.,* vol. 5, no. 5511, pp. 1-12, 2014.

[36] H. S. Baldwin, H. M. Shen, H. C. Yan, H. M. DeLiss, A. Chunh, C. Mickanin, T. Trask, N. E. Kirschbuaum, P. J. Newman and S. M. Albelda, "Platelet Endothelial Cell Adhesion Molecule-1 (PECAM-1/CD31): Alternatively Spliced, Functionally Distinct Isoforms Expressed During Mammalian Cardiovascular Development," *Development,* vol. 120, pp. 2539-2553, 1994.

[37] H.-J. Schnittler, B. Puschel and D. Drenckhahn, "Role of Cadherins and Plakoglobin in Interendothelial Adhesion Under Resting Condition and Shear Stress," *Am. J. Physiol. ,* vol. 273, no. 5 p 2, pp. H2396-H2405, 1997.

[38] M. Osawa, M. Masuda, K.-I. Kusano and K. Fujiwara, "Evidence for the Role of Platelet Endothelial Cell Adhesion Molecule-1 in Endothelial Cell Mechanosignal Transduction: Is It a Mechanoresponsive Molecule?," *J. Cell Bio.,* vol. 158, no. 4, pp. 773-775, 2002.

[39] E. Sho, M. Komatsu, M. Sho, H. Nanjo, T. M. Singh, C. Xu, H. Masuda and C. K.

Zarins, "High Flow Drives Vascular Endothelial Cell Proliferation During Flow-Induced Arterial Remodeling Associated with the Expression of Vascular Endothelial Growth Factor," *Exp. Mol. Pathol.,* vol. 75, pp. 1-11, 2003.

[40] E. Tzima, M. Irani-Tehrani, W. B. Kiosses, E. Dejana, D. A. Schultz, B. Engelhardt, G. Cao, H. DeLisser and M. A. Schwartz, "A Mechanosensory Complex that Mediates the Endothelial Cell Response to Fluid Shear Stress," *Nature,* vol. 437, pp. 426-431, 2005.

[41] B. L. Harry, J. M. Sanders, R. E. Feaver, M. Lansey, T. L. Deem, A. Zarbock, A. C. Bruce, A. W. Proyer, B. D. Gelfand, B. R. Blackman, M. A. Shwartz and K. Ley, "Endothelial Cell PECAM-1 Promotes Atherosclerotic Lesions in Areas of Disturbed Flow in ApoE-Deficient Mice," *Atheroscler. Thromb. Vasc. Biol.,* vol. 28, pp. 2003-2008, 2008.

[42] J.-J. Chiu, L.-J. Chen, C.-N. Chen, P.-L. Lee and C.-I. Lee, "A Model for Studying the Effect of Shear Stress on Interactions Between Vascular Endothelial Cells and Smooth Muscle Cells," *J. Biomech.,* vol. 37, pp. 531-539, 2004.

[43] F. M. White, Fluid Mechanics, *7th edition*, New York: McGraw Hill, 2009.

[44] S. F. Kemeny, S. F. Dannielle and M. C. Alisa, "Hypo- and Hyperglycemia Impair Endothelial Cell Actin Alignment and Nitric Oxide Synthase Activation in Response to Shear Stress," *PLOS ONE,* vol. 8, no. 6, p. e66176, 2013.

[45] P. Poirier, "Exercise, Heart Rate Variability, and Longevity: The Cocoon Mystery?," *Circulation,* vol. 129, pp. 2085-2087, 2014.

[46] J. S. Zigler , J. L. Lepe-Zuniga, B. Vistica and I. Grey, "Analysis of the Cytotoxic Effects of Light-Exposed HEPES-Containing Culture Medium," *In Vitro Cell. Dev. Biol.,* vol. 21, no. 5, pp. 282-287, 1985.

[47] J. L. Lepe-Zuniga , J. S. Zigler and I. Gery , "Toxicity of Light-Exposed HEPES Media," *J. Immunol. Methods,* vol. 103, no. 1, pp. 145-150, 1987.

[48] W. Rasband, "ImgaeJ 1.48V," [computer software], National Health Institue (NIH),

retrieved from: http://imagej.nih.gov/ij/, December 2014.

[49] A. B. Watson and A. Poison, "Separable Two-dimensional Discrete Hartley Transform," *J. Opt. Soc. Am.,* vol. 3, no. 12, pp. 2001-2004, 1986.

[50] IBM, "SPSS Statistics 22, " [computer software], retrieved from: http://myvlab.uwo.ca/, February 2015.

[51] X. Peng, F. A. Recchia, B. J. Byrne, I. S. Wittstein, R. C. Zeigelstein, D. A. Kass and S. Ryoo, "In Vitro System to Study Realistic Pulsatile Flow and Stretch Signaling in Cultured Vascular Cells," *Am. J. Cell Physiol.,* vol. 279, pp. C797-C805, 2000.

[52] M. A. Farcas, L. Rouleau, R. Fraser and R. L. Leask, "Development of 3-D, in Vitro, Endothelial Culture Models for the Study of Coronary Artery Disease," *Biomed Central,* vol. 8, pp. 1-11, 2009.

[53] N. Kataoka, S. Ujita and M. Sato, "Effect of Flow Direction on the Morphological Responses of Cultured Bovine Endothelail Cells," *Med. Biol. Eng. Comput.,* vol. 36, no. 1, pp. 122-128, 1998 .

[54] L. P. Voyvodic, D. Min and A. B. Baker, "A Multichannel Dapmed Flow System for Studies on Shear Stress-Mediated Mechanotransduction," *Lab on a Chip,* vol. 12, pp. 3322-3330, 2012.

[55] P. F. Davies, C. Shi, N. Depaola, B. P. Helmek and D. C. Polacek, "Hemodynamics and the Focal Origin of the Atherosclerosis: A Spatial Approach to Endothelial Structure, Gener Expression, and Function," *Ann. N. Y. Acad. Sci.,* vol. 947, pp. 7-16, 2001.

[56] A. Woodfin, M. Voisin and S. Nourshargh, "PECAM-1: A Multifunctional Molecule in Inflammation and Vascular Biology," *Arterioscler. Thromb. Vasc. Biol.,* vol. 27, pp. 1870-1878, 2007.

[57] L. Cao, A. Wu and G. A. Truskey, "Biomechanical Effects of Flow and Conculture on Human Aortic and Cord Blood Derived Endothelial Cells," *J. Biomech.,* vol. 44,

pp. 2150-2157, 2011.

[58] D. E. Conway, M. T. Breckennridge, E. Hinde, E. Gratton and C. S. Chen, "Fluid Shear Stress on Endothelial Cells Modulates Mechanical Tension across VE-Cadherin and PECAM-1," *Curr. Biol.,* vol. 23, no. 11, pp. 1024-1030, 2013.

[59] D. E. Conway and M. A. Schwartz, "Mechanotransduction of Shear Stress Occurs through Changes in VE-Cadherin and PECAM-1 Tension: Implications for Cell Migration," *Cell Adh. Migr.,* p. DOI:10.4161/19336918.2014.968498, 2014.

[60] Z. Chen and E. Tzima, "PECAM-1 is Necessary for Flow-Induced Vascular Remodeling," *Atheros. Thromb. Vasc. Biol.,* vol. 29, pp. 1067-1073, 2009.

Chapter 5

5 Conclusions and Recommendations

The following sections will present a summary of this dissertation followed by conclusions and the significance of the conducted research as well as the recommendations for the future directions.

5.1 Summary

In this dissertation, an *in vitro* hemodynamic facility based on the parallel plate flow chamber (PPFC) concept was developed to study the effects of wall shear stress (WSS) on endothelial cells (ECs). The major problems addressed here were (1) development and testing a hemodynamic facility with improved features compared to the similar facilities; (2) precise quantification of the flow-related parameters in the PPFC and (3) Quantification of the EC morphological and cytoskeletal remodeling in response to various quantified flow cases.

5.2 Conclusions

The current PPFC was manufactured from ULTEM 1000 which is autoclavable, economic in terms of manufacturing, resistant to chemical corrosion and of reasonable strength (compared to other materials used in similar apparatus such as 316 SS [1-3]) along with a lighter weight. This channel enabled an easy and quick assembly/disassembly (i.e., essential feature of a biological apparatus). An adjustable height obstacle that can be manufactured in any desired shape (to mimic a more realistic occlusion structure) along with a glass working section for the optical access required in real-time microscopy as well as for the flow measurements, make this channel a valuable and novel research tool. The channel dimensions were chosen so that a wide range of physiologically-relevant hemodynamic factors are achievable through application of a physiological pump. Porcine aortic endothelial cell (PAEC) survival within the experimental facility was successfully tested.

The Laser Doppler Velocimetry (LDV) method was used to quantify the flow in the PPFC with D_h=3.26 mm and aspect ratio of 9.72 (i.e., to the authors' knowledge, these are the first detailed LDV measurements in a channel flow with a small hydraulic diameter which is on the threshold of conventional channels (3 mm)). Application of a mini-LDV probe (with a smaller half-angle of 3.9°, compared to conventional probes) tilted by slightly larger than its half angle, facilitated both u- and v- velocity measurements without the laser beams encountering the channel side walls. A method, based on monitoring the voltage change in the LDV photomultiplier output, for determination of the wall location with respect to the LDV measuring volume centre was established with a positional uncertainty of ≈ ±27 μm which was in good agreement with the previous works where a similar method was employed [4-5]. The first measurement point from the channel wall with and without tilting the LDV probe was found to be at 2y/H=0.04 and 2y/H=0.22, respectively, and hence, tilting the probe was found to facilitate the boundary layer measurements, significantly. The experimental uncertainties associated with U, V, u_{rms}, v_{rms}, $\overline{u'v'}$ and WSS (determined from the velocity gradient method) were found to be within ±7, ±8.1, ±10.37, ±11.87, ±15.76 and ±15.4% respectively.

Five flow cases including the low steady laminar (LSL, Re=100), medium steady laminar (MSL, Re=990), non-zero-mean sinusoidal laminar (NZMSL, $R_{0\text{-}min}\approx 0$, $Re_{0\text{-}max}\approx 155$, $R_{0\text{-}mean}\approx 45$ and α=2.76), laminar carotid (LCRD, $Re_{0\text{-}min}\approx 100$, $Re_{0\text{-}max}\approx 560$ and $Re_{0\text{-}mean}\approx 282$, α=2.76) and low-Re turbulent (Re=2750 or Re_0=1830) flows were quantified. For the low-Re turbulent flow, at least two data points were measured in the viscous sublayer ($y^+<5$ [6]) and the turbulent statistics were also discussed. In majority of the previous studies, the flow uniformity across the channel width remains under-reported [1, 7], whereas in the present, flow uniformity was investigated for all the four laminar cases. These flows were found to be uniform over 65-75% across the span of the channel for the LSL and MSL cases which were in good agreement with the theoretical relation [7] with the differences< ±5%. Similarly, the flow was found to be uniform over 40 and 60% across the span of the channel for the NZMSL and LCRD cases, respectively. For the laminar flow regimes, the WSS was assessed by multiplication of the dynamic viscosity of the biological fluid by the velocity gradient at the wall. Second order polynomial regression with $2y_1/H=0.09$ and $N_p=5$ yielded the best accuracy for the WSS determinations. For the steady cases (LSL and MSL), the WSS was estimated from the experimentally measured data, as well as from the analytical solution of a laminar channel flow and the difference between the two methods was about ±9%. Comparison between the experimental results with the analytical solution for a laminar channel flow returned a better agreement (≈6% less difference) than the simplified WSS equation in a channel flow which has been widely applied in PPFC applications [2, 9]. The WSS for the low-Re turbulent flow was determined by the same method described above (velocity gradient method) as well as the relationship between the Reynolds shear stress and the WSS (at all three locations D, E and F) and both methods were in agreement within ±5%.

Phase-averaged velocity data were analyzed for both pulsatile flow cases and the maximum flow in each pulse was found to be around 0.7 $U_{b\text{-}max}$, whereas this value was about 1.55 U_b for the steady laminar case.

The four well-quantified flow cases (LSL, MSL, NZMSL and LCRD) were applied on PAECS to investigate the effects of flow on morphological modulation, F-actin bundle arrangement and PECAM-1 distribution. The current study is the only work among the other related studies in this area that has applied four various WSS profiles (including a physiological LCRD case) on ECs using the same facility for comparison between the EC responses to the flow.

The S.I. and the cell angle of orientation with the flow direction were found to be more suitable morphological parameters for studying the effects of flow over ECs compared to the area and perimeter.

The S.I. significantly decreased for all of the flow exposed samples compared to the static control. It was also confirmed that the S.I. changes are correlated with the reversing/uni-directional nature of the flow as well as with the mean and amplitude of the pulse for the pulsatile flow conditions which confirms the previous works [7, 10]. From the symmetry seen in the histogram illustration of the EC angle of orientation, it was concluded that the flow was merely streamwise in the PPFC, for all the cases. Also the histogram illustration was found to be a more detailed tool for studying the cell angle of orientation. In all of the four flow cases, the EC started to become oriented with the flow direction, although the cell frequency in each band was flow-sensitive. For the first time in this study, the existing 2D FFT-based analysis method [11-12] of F-actin alignment was applied as a discriminative tool on a range of flow cases for comparison. It was shown for the first time that F-actin bundles rearranged themselves to gain a certain polarity within a single cell. An A.I. was defined based on the findings from the FFT-analysis and was shown to offer a better comparative tool than another definition reported in the literature [12]. A linear relationship was proposed for the first time in this study to quantify the relationship between the cell vs. F-actin alignment.

Another significant contribution of the current work was the comparison between the PECAM-1 morphology (localization) among the four flow cases which showed that the peripheral PECAM-1 band seen in static control was conserved in the MSL and LCRD cases whereas both LSL and NZMSL cases resulted in partial/full peripheral PECAM-1 band loss. A P.R.D. was defined (for the first time in this study) to account for the peripheral PECAM-1 band area and was shown to be a very suitable discriminating parameter between all the cases. These findings might shed light to the mechanisms involved in the role of PECAM-1 [13-14] as a part of a mechanosensory complex in ECs.

5.3 Recommendations

It is recommended that the current physiological pump be replaced with a miniature, autoclavable model to (1) reduce the required biological fluid for each experiment, (2) ease the sterilization process and shorten the time required (≈ 4 hours with the present set-up) and maintain an sterilized facility for a longer experiment period and (3) allow locating the entire flow loop inside an incubator to ensure the sterility and ease of temperature and CO_2 adjustments.

Application of other flow measurement techniques such as micro-PIV might be also beneficial to compare with the current results and also to capture more detailed information about the flow structure (particularly for a stenosed case). In the case where the parameter of interest is merely the WSS, MEMS-based techniques might be beneficial as well.

It is also recommended that the experiments in the vicinity of the obstacle with (1) varying height (stenosis %) and (2) different occlusion shapes (e.g., cosine-shaped) be carried out to mimic disturbed flow conditions with accurately quantified separation points, recirculation regions and reattachment points under physiologically relevant flow conditions. Although the LSL and NZMSL cases studied in the present work are known to be athero-prone flow types, more realistic flow conditions would shed light into further understanding of the pathobiological factors involved in the effects of hemodynamics on EC dysfunction. As shown and discussed in this dissertation, EC are highly sensitive to the applied mechanical stimuli and hence approaching the experimental conditions *in vivo* would further unveil the complex response of the EC via mechanotransduction.

Investigation of up-/down- regulation of the PECAM-1 and adhesion molecules such as VCAM-1 would also be beneficial to correlate the current findings, with regards to the significant peripheral PECAM-1 band loss in the LSL and NZMSL flows compared to the MSL and LCRD cases, with EC dysfunction, since these analyses would further shed light on the contribution of the PECAM-1 as part of a mechanosensory complex and atherogenesis, consequently.

5.4 References

[1] R. M. Nerem, M. J. Levesque and J. F. Cornhill, "Vascular Endothelial Morphology as an Indicator of the Pattern of Blood Flow," *J. Biomech. Eng.,* vol. 103, pp. 172-176, 1981.

[2] B. R. Blackman, K. a Barbee and L. E. Thibault, "In Vitro Cell Shearing Device to Investigate the Dynamic Response of Cells in a Controlled Hydrodynamic Environment," *Ann. Biomed. Eng.,* vol. 28, no. 4, pp. 363-372, 2000.

[3] C. F. Dewey and S. R. Bussolari, "The Dynamic Response of Vascular Endothelial Cells to Fluid Shear Stress," *J. Biomech. Eng.,* vol. 103, pp. 177-185, 1981.

[4] F. Durst, J. Jovanovic and J. Sender, "LDA Measurements in the Near-wall Region

of a Turbulent Pipe Flow," *J. Fluid Mech.,* vol. 295, pp. 305-335, 1995.

[5] F. Durst, J. Lekakis, J. Jovanovic and Q. Ye, "Wall Shear Stress Determination from Near-Wall Mean Velocity Data in Turbulent Pipe and Channel Flows," *Exp. Fluids,* pp. 417-428, 1996.

[6] F. M. White, Fluid mechanics, seventh edition, New York: McGraw Hill, 2009.

[7] J.-J. Chiu and S. Chien, "Effects of Disturbed Flow on Vascular Endothelium; Pathophysiological Basis and Clinical Perspectives," *Physiol. Rev.,* vol. 91, pp. 327-387, 2011.

[8] G. A. Truskey, F. Yuan and D. F. Katz, Transport Phenomena in Biological Systems, NY: Pearson, 2009.

[9] S. Chien, "Mechanotransduction and Endothelial Cell Homeostasis; the Wisdom of the Cell," *Am. J. Physiol. Heart Circ. Physiol.,* vol. 292, pp. 1209-1224, 2007.

[10] G. Helmlinger, R. V. Geiger, S. Schreck and R. M. Nerem, "Effects of Pulsatile Flow on Cultured Vascular Endothelial Cell Morphology," *J. Biomech. Eng.,* vol. 113, pp. 123-131, 1991.

[11] C. E. Ayres, B. Shekharjha, H. Meredith, J. R. Bowman, G. R. Bowlin and S. C. Henderson, "Measuring Fiber alignment in Electrospun Scaffolds: A User's Guide to the 2D Fast Fourier Transfrom Approach," *J. Biomater. Sci.,* vol. 19, no. 5, pp. 603-621, 2008.

[12] A. D. van der Meel, A. A. Poot, J. Feijen and I. Vermes, "Analyzing Shear-Induced Alignmnet of Actin Filaments in Endothelial Cells with a Microfluid Assay," *Biomicrofluidics,* vol. 4, pp. 011103-1-5, 2010.

[13] D. E. Conway and M. A. Schwartz, "Mechanotransduction of Shear Stress Occurs through Changes in VE-Cadherin and PECAM-1 Tension: Implications for Cell Migration," *Cell Adh. Migr.,* p. DOI:10.4161/19336918.2014.968498, 2014.

[14] Z. Chen and E. Tzima, "PECAM-1 is Necessary for Flow-Induced Vascular

Remodeling," *Atheros. Thromb. Vasc. Biol.,* vol. 29, pp. 1067-1073, 2009.

Appendices

Appendix 1

A Brief Literature Review on Wall Offset Determination

Due to the dimensions and size of the channel, determination of measuring volume location with respect to the wall was of critical importance since the shear stress assessments (boundary layer velocity measurements) are highly dependent on the accurate determination of wall location. This section will briefly discuss some of the methods reported in the literature concerning this topic.

While numerous technical and review papers have been dedicated to the determination of the skin friction including measurement or post-processing techniques, Orlu *et al.* were the first to dedicate a detailed discussion concerning the uncertainty in wall location determination techniques [1]. Many methods (optical/non-optical, invasive/non-invasive) have been proposed depending on the feasibility of the applied method. While a simple ruler may suffice for measurements in the outer/core region of wall bounded flows, more sophisticated methods are required in the inner region (closer to the wall). Microscopes, theodolites and cathetometers are among the most frequently used devices which have been reported to have an accuracy between 1 and 25 μm [1]. For optically accessible cases, laser based measurement techniques have been used. Takagi has used a laser and photodiodes to determine the height of a hot-wire sensor from the wall and reported the accuracy be within 0.01 mm yet dependant on the optical glass fibres used for their system [2]. Osterland also measured the location of the wall in a hot-wire velocity measurement by using a high magnification microscope with an absolute error of ±5 μm [3]. Hutchins *et al.* have applied a laser triangulation positioning technique to determine the wall location using hot-wire anemometry [4] within ±2.5 μm.

Very few papers were found on the quantitative determination of wall location using an LDV system. All of the reported works have applied accurate traversing systems (i.e., computer controlled stepping motor with an accuracy of 1 to 10 μm) to move the beams in various directions [5-9]. It has been reported that there is a distinct frequency shift associated with the wall once the beam is traversed into the wall [5-8, 10]. Durst *et al.* traversed the measuring volume into the wall to detect the light scattering due to small particles attached to the wall. The location of the maximum output of the photodiode was recorded as being the wall location with the positioning repeatability better than ±40 μm [5]. Byun *et al.* also reported a strong signal when the beam was focused just on the surface, although the accuracy of the method they used was not reported [8]. Radomsky *et al.* determined the wall location by tilting the LDV probe by the half angle of the beam and using two techniques: lowering the laser power and visually observing the beam crossing just at the wall and also monitoring the output from the photomultiplier using an oscilloscope [10]. They reported that both methods produced almost identical results for determining the location of the wall with an accuracy of ±20 μm. Also, some post-processing methods for LDV measurements have been reported. Durst *et al.* determined the precise location of the measuring volume with respect to the wall (with an accuracy of ±8 μm) by identifying the point where the longitudinal velocity profile showed a distinct change in slope which was caused by partial intrusion of the measuring volume into the test section [7]. For a clean surface, only a small number of particles are collected at the wall. Once the measuring volume is partially into the wall, only that part of the fluid through which scattering particles pass, will have a major contribution to the LDV data set. The resultant mean velocity is related to the fluid in the centre of the measuring volume located in the fluid (actual centre of measurement volume); however, it is common to assign the centre of the entire measurement volume to be the centre of measurement (theoretical centre of the measurement volume). Hence, the measured values are higher than the actual values in the region very close to the wall. The location of this slope change was considered as being a distance equal to half the measuring volume diameter to the wall [7]. This method is illustrated in Figure A-1-1.

In the present study, the techniques discussed regarding the hot-wire velocity measurements were not applicable (although having higher accuracy) since the experiments were carried out in a closed channel with water-based fluid.

The discussed previous works for wall position determination using LDV, showed that the majority of the studies have applied the concept of voltage output change by traversing the measuring volume from the wall into the fluid and, hence, for the current study, the wall location was determined through this method. The advantages of this applied technique were its non-invasive nature, independency from the accuracy of the LDV measurement itself, independency from the applied post processing (e.g., determination of the slope change from time-averaged velocity), minimum reliability on human observation (e.g., visual observations), along with an acceptable accuracy (i.e., ≈±30 μm in the current work which is in the range of the reported studies using a similar technique). Tilting the probe by the half angle of the laser beam was also significantly beneficial in terms of minimizing the beam interactions with the confined geometry of the channel walls.

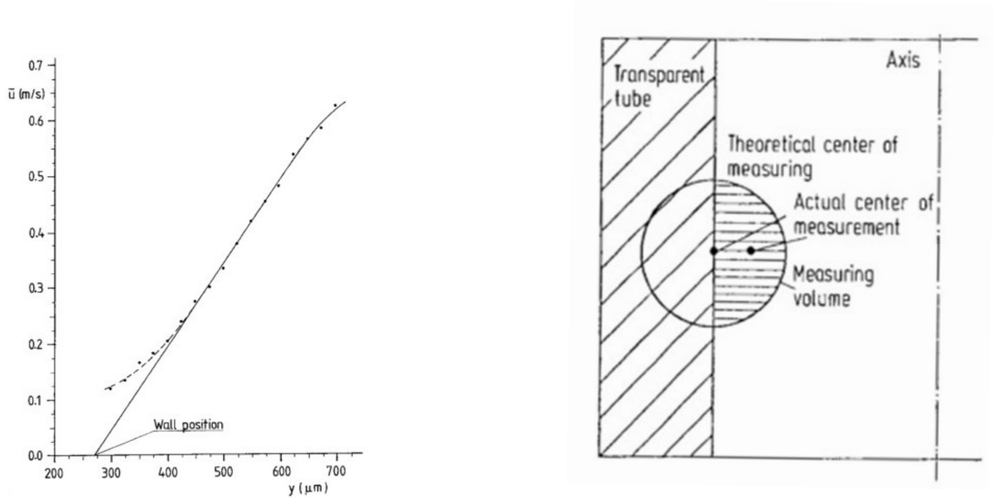

(a) **(b)**

Figure A-1-1 Near-wall velocity profile vs. position reading of traversing system (a); actual vs. theoretical measurement volume location at the wall (b) [7]

References

[1] R. Orlu, J. M. Fransson and H. Alfredsso, "On Near Wall Measurements of Wall Bounded Flows—The Necessity of an Accurate Determination of the Wall Position,"

Prog. Aerosp. Sci., vol. 46, no. 8, p. 353–387, 2010.

[2] S. Takagi, "Hot-wire Height Gauge Using a Laser and Photodiodes," *Expt. Fluids.,* vol. 3, pp. 341-342, 1985.

[3] J. M. Osterlund, "Experimental Studies of Zero Pressure-Gradient Turbulent Boundary-Layer Flow," *PhD thesis*, Royal Institute of Technology, Stockholm, 1999.

[4] N. Hutchins and K.-S. Choi, "Accurate Measurements of Local Skin Friction Coefficient Using Hot-wire Anemometry," *Prog. Aerosp. Sci.,* vol. 38, p. 421–446, 2002.

[5] F. Durst, J. Jovanovic and J. Sender, "LDA Measurements in the Near-wall Region of a Turbulent Pipe Flow," *J. Fluid Mech.,* vol. 295, pp. 305-335, 1995.

[6] F. Durst, J. Lekakis, J. Jovanovic and Q. Ye, "Wall Shear Stress Determination from Near-Wall Mean Velocity Data in Turbulent Pipe and Channel Flows," *Exp. Fluids.,* vol. 20, no. 6, pp. 417-428, 1996.

[7] F. Durst, R. Miller and J. Jovanovie, "Determination of the Measuring Position in Laser-Doppler Anemometry," *Exp. Fluids.,* vol. 6, pp. 105- 110, 1988.

[8] G. Byun, S. M. Olcemen and S. L. Roger , "A miniature laser-Doppler velocimeter for simultaneous three-velocity-component measurements," *Meas. Sci. Technol.,* vol. 15, no. 10, pp. 2075-2082, 2004.

[9] A. D. Schwarz-Van Manen, A. Van Geloven, J. C. Stothart, K. Krishna Parsa and F. Nieuwstadt, "Friction Velocity and Virtual Origin Estimates for Mean Velocity Profiles above Smooth and Triangular Riblet Surfaces," *Appl. Sci. Res.,* vol. 50, pp. 233-254, 1993.

[10] R. W. Radomsky and T. A. Thole, "Detailed Boundary Layer Measurements on a Turbine Stator Vane at Elevated Freestream Turbulence Levels," *J. Turbomach.,* vol. 124, pp. 104-118, 2002.

[11] D. N. Ku, D. P. Giddens, C. K. Zarins and S. Glagov, "Pulsatile Flow and Atherosclerosis in the Human Carotid Bifurcation," *Arterioscler. Thromb. Vasc. Biol.,* vol. 5, pp. 293-302, 1985.

Appendix 2

Spatial Correction Due to Refractive Index Mismatch

Due to the refractive mismatch of various media for an incident beam, it is a basic rule of optics that when a ray of light strikes an interface with different refractive index, the light will refract according to Snell's law [1]

$$n_1\sin(\theta_1)= n_2\sin(\theta_2) \tag{A-2-1}$$

where n and θ represent the refractive index of each medium and the angle that the incident light makes with the perpendicular projection (see Figure A-2-1).

The distance between the fringes (at the two LDV crossing beams) d_f is given by

$$d_f=\lambda/(2\sin\theta) \tag{A-2-2}$$

where λ is the wavelength of the laser light.

Considering $n_1=1$ for air since the laser beam is transmitted in the air after being emitted from the probe

$$\sin(\theta_2) = \sin(\theta_1)/ n_2 \tag{A-2-3}$$

The dependence of the wavelength on the medium is given by

$$\lambda_2= n_1 \lambda_1/ n_2 \tag{A-2-4}$$

Hence for the $n_1=1$,

$\lambda_2 = \lambda_1 / n_2$ (A-2-5)

To determine $(d_f)_2$

$(d_f)_2 = \lambda_2/(2\sin\theta_2) = (\lambda_1/n_2)/(2\sin(\theta_1)/n_2) = (d_f)_1$ (A-2-6)

Hence, the fringe spacing will be the same in medium 1 so that the size of the measuring volume remains unchanged.

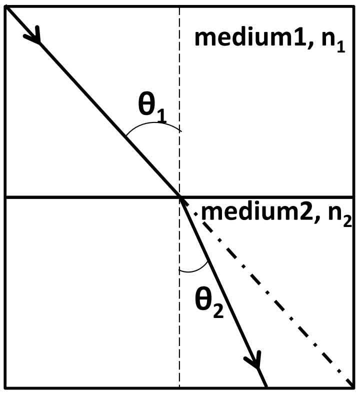

Figure A-2-1 A simple schematic of Snell's Law

Hence, spatial corrections are required for the location of the measuring volume since the two refracted incident beams cross at a point that is different from the original point where the beams are only traveling in one medium. A ray optics analysis of a beam after striking the flat optical window and entering the fluid is illustrated in Figure A-2-2.The following equation was applied for spatial correction in the horizontal direction (parameters are defined in Figure A-2-2)

$$F_a\cos\varphi = F_g\cos\varphi(\tan\theta_a/\tan\theta_f) + t[1-(\tan\theta_w/\tan\theta_f)] + d\cos\varphi[1-(\tan\theta_w/\tan\theta_f)] \qquad \text{(A-2-7)}$$

The refractive index for air, for the precision glass window and the biological fluid were considered to be 1.000 [1], 1.520 (manufacturer's data, Angstrom Precision Optics Inc., USA) and 1.345 [1, 2]. According to Equation A-2-1, the actual focal length is different from the given value and, in a given experiment, if the beam strike angle is constant; it depends only on the distance from the lens to the window.

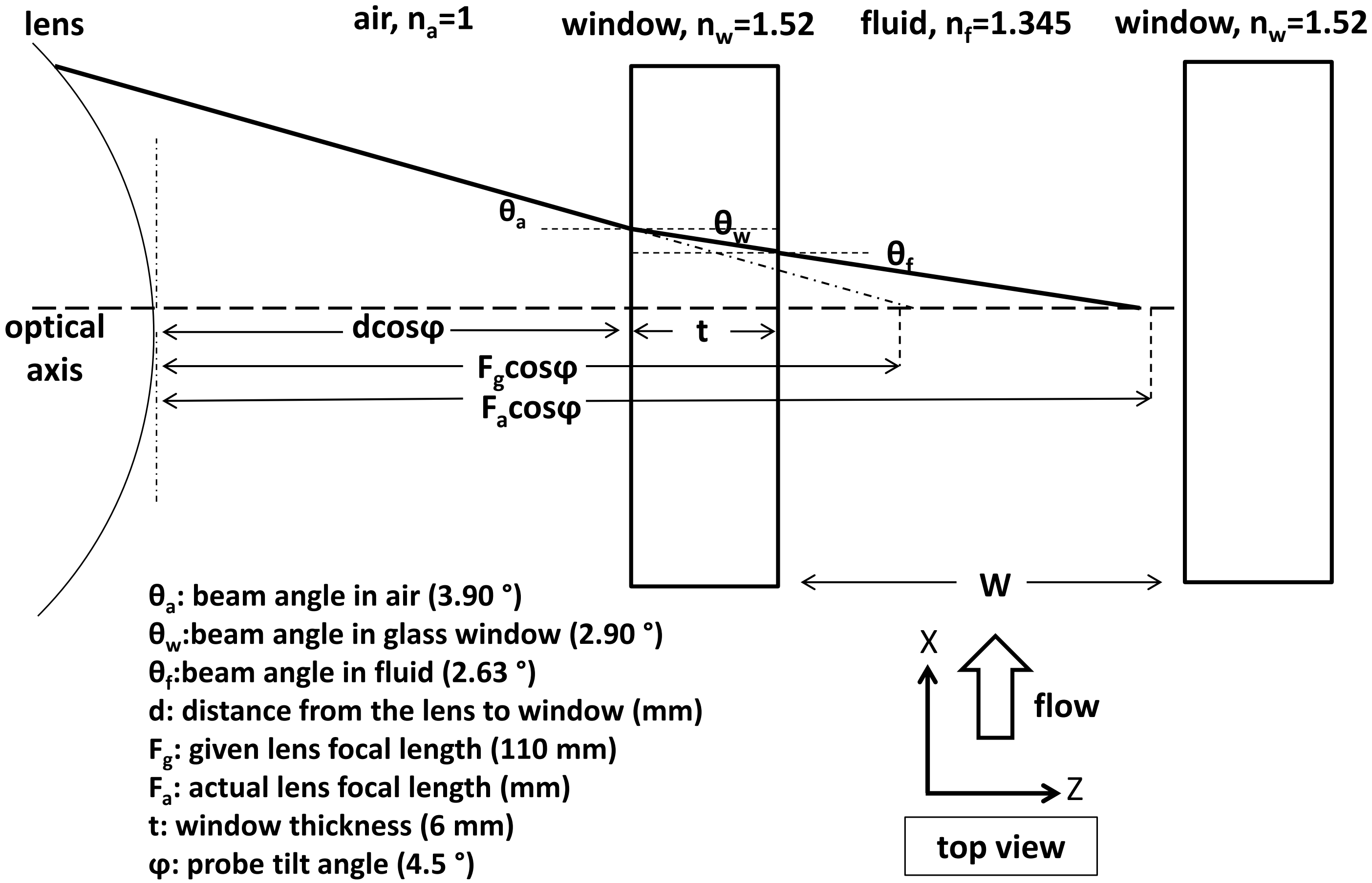

θ_a: beam angle in air (3.90 °)
θ_w:beam angle in glass window (2.90 °)
θ_f:beam angle in fluid (2.63 °)
d: distance from the lens to window (mm)
F_g: given lens focal length (110 mm)
F_a: actual lens focal length (mm)
t: window thickness (6 mm)
φ: probe tilt angle (4.5 °)
W: channel width (17.5 mm)

Figure A-2-2 Refraction of beam in the glass working section (X-Z plane, top view)

As an example, if the probe distance is adjusted to be at the centre of the channel, the focal length will be 115.54 mm, which requires the manual adjustment of the measurement location at each spatial position. These adjustments were applied for the conducted experiments. For lateral direction measurements, the consistency of the height of the measured points was checked by traversing the probe into the lower wall of the PPFC in order to accurately locate the wall as the datum and traversing upward until the desired height.

It is recommended that the probe optical axis be perpendicular to the window. However, in this study, the probe was tilted slightly larger than the half angle of the probe (this method is also reported in the literature [3]). Tilting angles under 10° for a wall thickness of less than 35 mm are considered acceptable [4] and, hence, the tilting angle of $\varphi=4.5^{o}$ in the current study (to allow for the precise wall location determination, as well as allowing v-component velocity measurement) with the existing window thickness (t=6 mm) was valid. A larger tilting angle (>10º) and deeper penetration of the beam [4] into the fluid can cause significantly less scattered light to be collected by receiver.

References

[1] J. J. Gu, Y. F. Yu, S. H. Ng, P. H. Yap, X. Q. Zhu, T. H. Cheng and A. Q. Liu, "Real-Time Measurement of Cellular Refractive Index and Thickness Using Cell Culture Chip," in *12th International Conference in Miniaturized Systems for Chemistry and Life Sciences*, San Diego, USA, 2008.

[2] D. Borja , F. Manns, A. Ho , Z. M. Ziebarth , A. C. Acosta and E. Arrieta-Quintera , "Refractive Power and Biometric Properties of the Nonhuman Primate Isolated Crystalline Lens," *Invest. Ophthalmol. Vis. Sci.,* vol. 51, p. 2118–2125, 2010.

[3] R. W. Radomsky and L. A. Thole, "Detailed Boundary Layer Measurement on a Turbine Stator Vane at Elevated Freestream Turbulence Levels," *J. Turbomach.,* vol. 124, pp. 107-118, 2002.

[4] TSI Incorporated , "Model TR360 5 beam fiberoptic Probe," Shoreview, MN, 2007.

Appendix 3

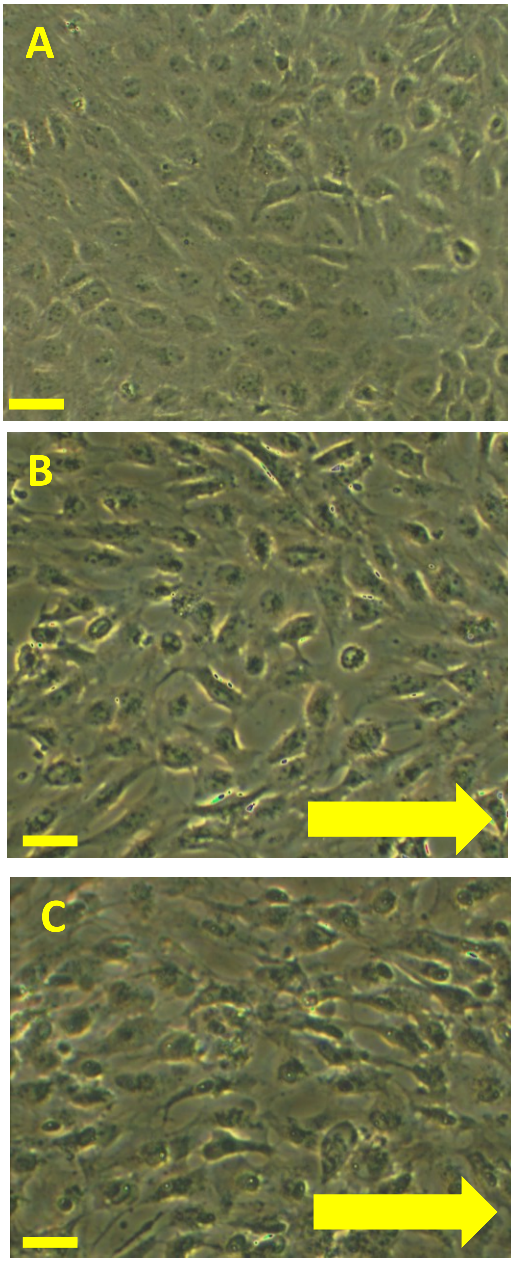

Figure A-3-1 Light microscopy image of the PAECs (A) in static condition; (B) exposed to laminar WSS=11.48±0.98 dyne/cm^2 for t=3 hours; (C) exposed to laminar WSS=11.48±0.98 dyne/cm^2 t=6 hours (yellow arrows in (B) and (C) are representing the flow direction). Scale bar=50 µm

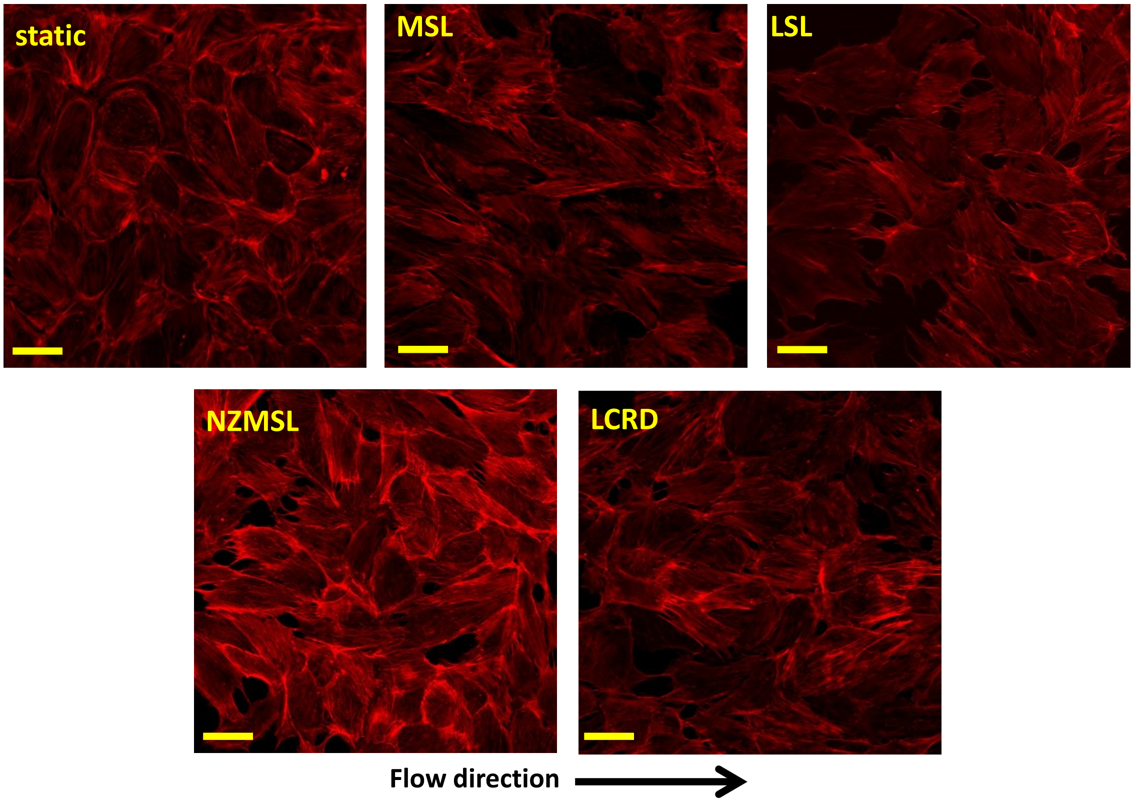

Figure A-3-2 The WSS remodels PAEC F-actin bundles under all four flow conditions. Immunofluorescence staining of F-actin bundles with Phalloidin (red). Scale bar=40 µm

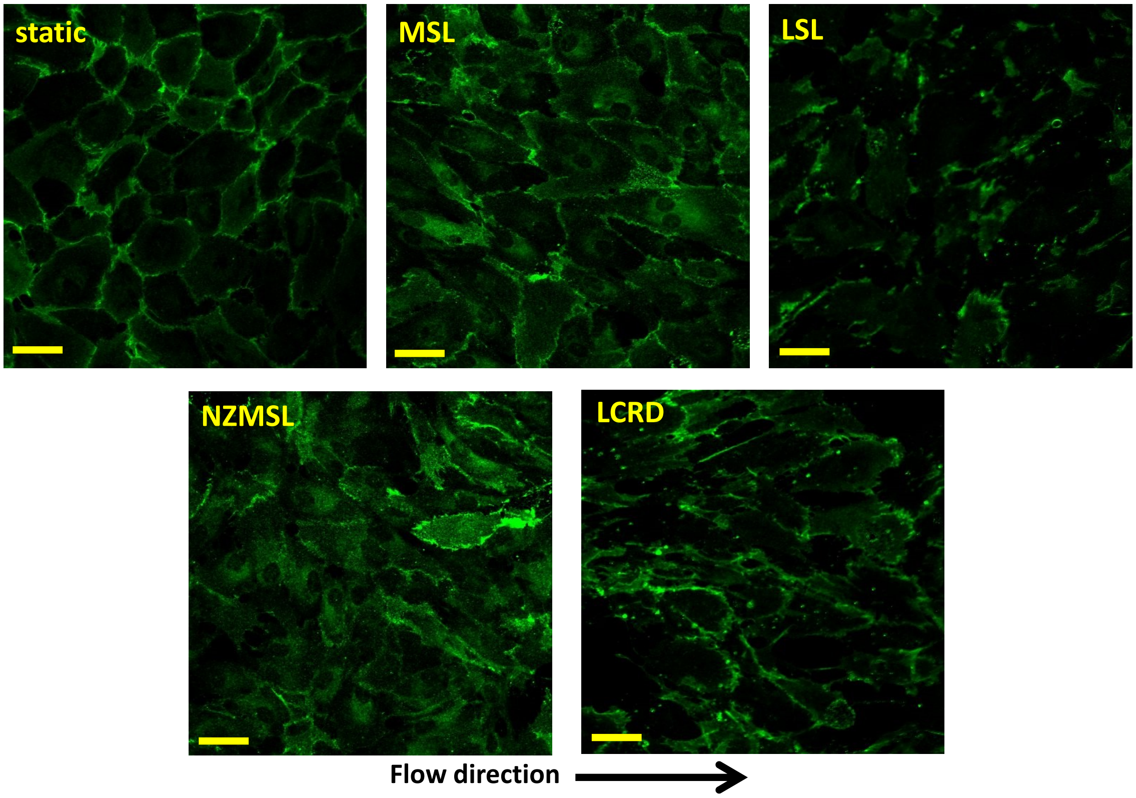

Figure A-3-2 The WSS remodels PAEC PECAM-1 under all four flow conditions. Immunofluorescence staining of PECAM-1 with CD31 (green). Scale bar=40 μm

Curriculum Vitae

Name:	Hamed Avari
Post-secondary Education and Degrees:	**Mechanical Engineering** Iran University of Science and Technology Tehran, Iran 2002-2006 B.Sc. **Mechanical Engineering (Biomechanics)** Sahand University of Technology Tabriz, Iran 2006-2009 M.Sc. **Mechanical Engineering** University of Western Ontario London, Ontario, Canada 2010-present, Ph.D.
Honours and Awards:	Awarded **Top Research Student** of 2008 in the Department of Mechanical Engineering at *Sahand University of Technology, Tabriz, Iran* Recipient of **CIHR fellowship Fund** in Strategic Training Program in Vascular Research (24K, 2010-2012), *Robarts Research Institute*, *University of Western Ontario, London, Canada*
Related Work Experience	Teaching and Research Assistant The University of Western Ontario 2010-2015

Publications and Conferences:

H. avari, E. Savory, “Laser Doppler Velocimetry Measurements under Steady and Pulsatile Flow Conditions in a Parallel Plate Flow Chamber,” Accepted in the 25th Canadian Congress of Applied Mechanics (CANCAM), London, Canada, June 2015.

H. avari, E. Savory, K. A. Rogers, “A Novel Hemodynamic Facility for Studying the Effects of Shear Stress on Endothelial Cell,” Canadian Society of Mechanical Engineering (CSME) International Congress, Toronto, Canada, May 2014.

H. Avari, M. Ahmadloui, F. Ghalichi, “A 3D Numerical Study of Oxygen Uptake in Pulmonary Capillaries to Present a Proper Relationship between Respiration Rhythm and Athletes’ Activity Levels,” The 6th International Symposium on Turbulence, Heat and Mass Transfer, Rome, Italy, September 2008.

H. Avari, M. Ahmadloui, F. Ghalichi, “A 2D Numerical Study of Gas Exchange System to Assess a Proper Relationship between Respiration Rhythm and Individual’s Activity Rate,” Iranian Journal of Biomedical Engineering. Special Issue: Biomechanics, Volume 2, Number 1, spring 2008.

H. Avari, M. Ahmadloui, F. Ghalichi, “The Study of Oxygen Diffusivity Effect on Oxygen Uptake in Pulmonary Capillaries,” The 5th Iranian Conference on Biomedical Engineering (ICBME), Mashhad , Iran, February 2008.

H. Avari, M. Ahmadloui, F. Ghalichi, “A Numerical study to assess a Proper relationship between respiration rhythm and athletes activities.” The 4th Cairo International Biomedical Conference 2008(CIBEC), Egypt, 2008.

Poster Presentation:

H. Avari, E. Savory, K. A. Rogers, “Effect of Blood Flow Shear Stress on Remodeling of Arterial Wall,” Western Sustainability and Environment Research Showcase, UWO, London, Canada, 2014.